

MEASUREMENT OF SINGLE DIFFRACTIVE DIFFERENTIAL CROSS  
SECTION  $\left(\frac{d\sigma}{dt}\right)$  AT  $\sqrt{s} = 1.96$  TeV USING THE DØ  
FORWARD PROTON DETECTORS

by  
ARNAB KUMAR PAL

Presented to the Faculty of the Graduate School of  
The University of Texas at Arlington in Partial Fulfillment  
of the Requirements  
for the Degree of

DOCTOR OF PHILOSOPHY

THE UNIVERSITY OF TEXAS AT ARLINGTON

August 2011

Copyright © by ARNAB KUMAR PAL 2011  
All Rights Reserved

To my parents, who made me who I am.

## ACKNOWLEDGEMENTS

I would like to thank my advisor Andrew Brandt for his guidance, ideas, patience, support and motivation for the work done in this thesis. It was a great learning experience to work under his supervision. I would also like to thank the UTA high energy group professors on the ATLAS and DØ experiments, Andy White, Kaushik De, Amir Farbin and Jae Yu for their constant support and motivation.

I am also grateful to the department of physics at UTA for their support. In particular I would like to thank the members of high energy physics group, Mark Sosebee, Edward, Rishiraj Pravahan, Alden Stradling and Ian Howley.

Much thanks is owed to the DØ collaboration members who have given me valuable resources because of which this work has been possible. I would like to thank the QCD group members at DØ and the conveners, Don Lincoln, Dmitry Bandurin, Sabine Lammers and Mike Strauss who have supported this analysis. I would like to thank the spokespersons of the DØ experiment Dmitri Denisov and Stefan Soldner-Rembold for their support and encouragement for the analysis efforts and George Ginther for his help in the understanding the detector and shifts. I would also like to thank Carlos Avila and Vlastislav Hynek for their useful advise and help during the analysis.

I would like to thank all my friends and colleagues whom I met at UTA, CERN and Fermilab who have helped at various stages during my stay as a graduate student.

Finally I would like to thank my parents and my wife for their everlasting love, support and guidance.

June 28, 2011

## ABSTRACT

### MEASUREMENT OF SINGLE DIFFRACTIVE DIFFERENTIAL CROSS SECTION $\left(\frac{d\sigma}{dt}\right)$ AT $\sqrt{s} = 1.96$ TeV USING THE DØ FORWARD PROTON DETECTORS

ARNAB KUMAR PAL, Ph.D.

The University of Texas at Arlington, 2011

Supervising Professor: Andrew Brandt

The analysis described in this dissertation uses the Forward Proton Detectors (FPD) installed at the DØ detector in Tevatron collider at Fermilab to measure the single diffractive differential cross section  $\left(\frac{d\sigma}{dt}\right)$  at  $\sqrt{s} = 1.96$  TeV center of mass energy. The single diffractive events were selected using the DØ central detector and the Forward proton detectors and  $|t|$  of the forward protons are measured using the FPD system. The analysis presents the measurement of the differential cross section of the single diffractive events as a function of  $|t|$  in the range  $0.2 < |t| < 1.3$  GeV<sup>2</sup>. The differential cross section measurement is within the theoretical and experimental expectations. The total single diffractive cross section ( $\sigma_{sd}$ ) in the region  $0.0 < |t| < 1.3$  GeV<sup>2</sup> is found to be  $9.682 \pm 0.048$  (stat.)  $\pm 1.219$  (syst.) mb.

## TABLE OF CONTENTS

ACKNOWLEDGEMENTS . . . . .	iv
ABSTRACT . . . . .	v
LIST OF FIGURES . . . . .	x
LIST OF TABLES . . . . .	xvii
Chapter	Page
1. INTRODUCTION . . . . .	1
1.1 The Standard Model . . . . .	1
1.2 Quantum Chromodynamics (QCD) . . . . .	4
1.3 Kinematics and Scattering . . . . .	5
1.4 Units used in high energy physics . . . . .	8
2. THEORETICAL OVERVIEW . . . . .	10
2.1 Diffraction . . . . .	10
2.1.1 Definition of Diffraction . . . . .	10
2.1.2 Soft Diffraction . . . . .	13
2.1.3 Hard Diffraction . . . . .	16
2.2 Regge Theory . . . . .	17
2.2.1 The $s$ and $t$ channel processes . . . . .	17
2.2.2 Crossing symmetry . . . . .	17
2.2.3 Optical theorem . . . . .	18
2.2.4 Scattering amplitude . . . . .	19
2.2.5 Regge trajectories . . . . .	19
2.2.6 Total scattering cross section . . . . .	20

2.3	The pomeron . . . . .	22
2.4	Single Diffraction Dissociation . . . . .	23
3.	EXPERIMENTAL APPARATUS . . . . .	25
3.1	Accelerator Complex . . . . .	25
3.1.1	Proton Source . . . . .	27
3.1.2	Linac . . . . .	27
3.1.3	Booster . . . . .	28
3.1.4	Main Injector . . . . .	28
3.1.5	Tevatron . . . . .	29
3.1.6	Anti-Proton Source and Recycler . . . . .	29
3.2	The DØ Detector . . . . .	30
3.2.1	Central Tracking System . . . . .	31
3.2.1.1	Silicon Micro-Strip Tracker . . . . .	32
3.2.1.2	Central Fiber Tracker . . . . .	34
3.2.1.3	Solenoid Magnet . . . . .	34
3.2.1.4	Preshower Detectors . . . . .	35
3.2.2	Calorimeter . . . . .	35
3.2.3	Muon System . . . . .	39
3.2.4	Luminosity Monitor . . . . .	40
3.2.5	Trigger and Data Acquisition System . . . . .	41
3.3	The DØ Forward Proton Detector . . . . .	42
3.3.1	FPD Layout . . . . .	43
3.3.2	FPD Position Detector . . . . .	45
3.3.3	FPD Timing Detector . . . . .	47
4.	ANALYSIS . . . . .	49
4.1	Data Sample . . . . .	49

4.1.1	High $\beta^*$ run . . . . .	49
4.1.2	Data sets . . . . .	50
4.1.3	Triggers used . . . . .	51
4.2	Data Reconstruction . . . . .	54
4.2.1	Alignment of detectors . . . . .	55
4.2.2	Reconstruction program . . . . .	58
4.2.2.1	Hit finding . . . . .	59
4.2.2.2	Reconstruction of tracks . . . . .	60
4.2.2.3	Timing information . . . . .	61
4.2.2.4	Low momentum tracks . . . . .	62
4.3	Validation of reconstruction . . . . .	65
4.3.1	Validation of track reconstruction . . . . .	66
4.3.2	Validation of hit finding . . . . .	69
4.4	Single diffractive event selection . . . . .	74
4.4.1	Trigger selection . . . . .	74
4.4.2	High and low mass single diffraction . . . . .	75
4.4.3	Detector correlation cuts . . . . .	76
4.4.3.1	Single diffractive Monte Carlo . . . . .	76
4.4.3.2	Single diffractive band cuts . . . . .	79
4.4.4	Halo rejection . . . . .	79
4.4.5	Detector fiducial cuts . . . . .	80
4.5	Corrections to single diffractive cross section . . . . .	82
4.5.1	Geometric acceptance . . . . .	82
4.5.2	Trigger efficiencies . . . . .	85
4.5.3	Luminosity . . . . .	100
4.5.4	High mass single diffractive fraction . . . . .	102



4.6	Background estimation and subtraction . . . . .	103
4.7	Kinematics of diffraction . . . . .	108
5.	RESULTS . . . . .	110
5.1	Single diffractive differential cross section . . . . .	110
5.1.1	Weighted average . . . . .	112
5.1.2	Systematic uncertainties . . . . .	119
5.1.2.1	Trigger Efficiency Systematic Uncertainty . . . . .	122
5.1.2.2	Ansatz function systematics . . . . .	123
5.1.2.3	Beam smearing systematics . . . . .	126
5.1.2.4	Total systematic uncertainties . . . . .	126
5.1.3	Single diffractive differential cross section . . . . .	128
5.2	Total single diffractive cross section . . . . .	128
5.3	Comparison with theory . . . . .	133
5.4	Conclusions . . . . .	134
Appendix		
A.	EXCLUSIVE $H^0$ AT ATLAS FPD . . . . .	137
B.	EXCLUSIVE $H^0 \rightarrow b\bar{b}$ AT ATLAS FPD . . . . .	142
C.	EXCLUSIVE $H^0 \rightarrow WW^*$ AT ATLAS FPD . . . . .	149
REFERENCES . . . . .		159
BIOGRAPHICAL STATEMENT . . . . .		167

## LIST OF FIGURES

Figure		Page
1.1	(a) Two-body exclusive scattering process represented by $1 + 2 \rightarrow 3 + 4$ and (b) Single-particle inclusive scattering process represented by $1 + 2 \rightarrow 3 + X$ . . . . .	5
2.1	Diffraction in nuclear and hadronic physics. Diffractive hadronic processes have behaviour similar to that of optical diffraction. The plots show the change in the cross section as a function of $\theta$ , which is proportional to $ t $ . . . . .	11
2.2	Diagram to illustrate diffractive scattering (a) Elastic scattering (b) Single diffraction (c) Double diffraction . . . . .	13
2.3	Illustration of elastic scattering in $p\bar{p}$ collision at the Tevatron and its $\eta - \phi$ topology . . . . .	14
2.4	Diagrams and $\eta - \phi$ topologies to describe single diffraction(SD), double diffraction(DD) and double pomeron exchange(DPE) processes in $p\bar{p}$ collision . . . . .	15
2.5	Description of hard diffraction in $p\bar{p}$ collision at the Tevatron and its $\eta - \phi$ topology for (a) hard single diffraction (b) hard double diffraction and (c) double pomeron exchange . . . . .	16
2.6	Crossing symmetry between (a) $s$ -channel and (b) $t$ -channel process . . . . .	18
2.7	Chew-Frautschi plot for the $t$ -channel process in $\pi^- \pi^0 \rightarrow \bar{p}n$ collisions . . . . .	20
2.8	Total cross section in $p\bar{p}$ collision shown in the upper curve and $pp$ collision shown in the curve below . . . . .	21
2.9	Single diffractive differential cross section as a function of $\sqrt{s}$ , theory and different experimental results . . . . .	23
3.1	Schematic diagram of the Fermilab accelerator complex . . . . .	26
3.2	Overview of the upgraded Run II DØ detector . . . . .	31

3.3	Overview of the Run II DØ Central Tracking System showing the SMT, CFT, Solenoid and the Preshower Detectors . . . . .	32
3.4	The Silicon Micro-Strip Tracker showing the 6 barrels, 12 F-Disks and 4 H-Disks . . . . .	33
3.5	Schematic view of the DØ Liquid argon and Uranium Calorimeter . . . . .	36
3.6	Diagram of the unit cell structure of the Calorimeter . . . . .	37
3.7	Quadrant cross sectional view of the pseudo-projective towers in the Calorimeter . . . . .	38
3.8	Layout of the Forward Proton Detector System . . . . .	43
3.9	Forward Proton Detector castle . . . . .	44
3.10	Schematic diagram of FPD position detectors and MAPMT . . . . .	46
3.11	Schematic view of the six scintillating fiber layers and the scintillating block of one detector . . . . .	47
4.1	Hitmaps showing position of the forward detectors on the proton side and the anti-proton side during the high $\beta^*$ store compared to the detector position in a normal store . . . . .	50
4.2	Comparison of the expected $ t $ acceptance during the accelerator run at $\beta^*=1.6$ m with that of standard operation . . . . .	51
4.3	Comparison of elastic event coordinates between spectrometers with detectors at the same locations . . . . .	56
4.4	The distribution of $\Delta x$ and $\Delta y$ for the detectors in the elastic events using the survey data. The distributions are normalized to unit area for comparison of their shapes . . . . .	56
4.5	The distribution of $\Delta x$ and $\Delta y$ for the detectors in the elastic events after applying the alignment . . . . .	57
4.6	Definition of cluster of (a)size one, (b)size two, (c)two clusters of size two characterizing a multi-hit event, (d)cluster of size three, (e)size four and (f)size five are shown . . . . .	60
4.7	Schematic diagram to show the timing of proton track using the timing detectors . . . . .	62
4.8	Distribution of halo bits in a run using the trigger	

scintillator timing information. The proton halo rates are much higher than the anti-proton halo rates . . . . .	63
4.9 Transverse momentum distribution, $p_T$ of the leading central tracks after lowering the threshold from 500 MeV to 150 MeV . . . . .	64
4.10 Track multiplicity distribution for three different kinds of halo events . . . . .	65
4.11 Difference in the values of $ t $ reconstruction for the elastic and FPD reconstruction. The plot on the left show the $\Delta t $ for AU spectrometer and the plot on right shows $\Delta t $ for PD spectrometer for the same elastic events . . . . .	67
4.12 $\Delta t _{p-\bar{p}}$ in the forward track $ t $ between the proton and the anti-proton for the elastic events. The shaded region shows the difference for the elastic reconstruction, the red points shows the FPD reconstruction . . . . .	68
4.13 Profile showing the difference between the elastic and FPD reconstruction as a function of $ t $ for the AU and PD spectrometers . . . . .	68
4.14 Profile plot showing the difference between the $p$ side $ t $ and $\bar{p}$ side $ t $ for the same elastic events obtained from the elastic and FPD reconstruction . . . . .	69
4.15 AUPD elastic band cuts evaluated using the elastic data points . . . . .	70
4.16 ADPU band cuts evaluated using the elastic data points . . . . .	70
4.17 Difference between the hit coordinates (x) for AU and PD detectors . . . . .	72
4.18 Difference between the hit coordinates (y) for AU and PD detectors . . . . .	72
4.19 Difference between the hit coordinates (x) for AD and PU detectors . . . . .	73
4.20 Difference between the hit coordinates (y) for AD and PU detectors . . . . .	73
4.21 (a) High mass single diffractive event in which the luminosity monitor on the opposite side is hit. (b) Low mass	

single diffractive event in which the diffractive products are carried along the beam pipe and there are no hits in the luminosity monitor . . . . .	75
4.22 Z-vertex distribution during the high $\beta^*$ run . . . . .	77
4.23 Figure showing the use of single diffractive Monte Carlo used to determine the single diffractive detector correlation cuts for AU and AD detectors . . . . .	78
4.24 Figure showing the use of single diffractive Monte Carlo used to determine the single diffractive detector correlation cuts for PU and PD detectors . . . . .	78
4.25 Fraction of events accepted in the P1U and P1D detectors due to the finite size of the detector (relative acceptance) [1] . . . . .	81
4.26 Fraction of events accepted in the P1U and P1D detectors due to the finite size of the detector . . . . .	83
4.27 The change in the acceptance function of four spectrometers due to choice of anzatz function . . . . .	84
4.28 The change in the acceptance function of four spectrometers due beam smearing . . . . .	85
4.29 Hit maps for the elastic events (red) compared to the single diffractive events (black) for the detector A1U . . . . .	87
4.30 Hit maps for the elastic events (red) compared to the single diffractive events (black) for the detector A2U . . . . .	88
4.31 Hit maps for the elastic events (red) compared to the single diffractive events (black) for the detector A1D . . . . .	89
4.32 Hit maps for the elastic events (red) compared to the single diffractive events (black) for the detector A2D . . . . .	90
4.33 Hit maps for the elastic events (red) compared to the single diffractive events (black) for the detector P1U . . . . .	91
4.34 Hit maps for the elastic events (red) compared to the single diffractive events (black) for the detector P2U . . . . .	92
4.35 Hit maps for the elastic events (red) compared to the single diffractive events (black) for the detector P1D . . . . .	93
4.36 Hit maps for the elastic events (red) compared to the	

single diffractive events (black) for the detector P2D . . . . .	94
4.37 Distribution of 3 detector hit events and 4 detector hit events for the calculation of trigger efficiencies of the first detectors . . . . .	96
4.38 Distribution of 3 detector hit events and 4 detector hit events for the calculation of trigger efficiencies of the second detectors . . . . .	97
4.39 Efficiencies for the first detectors of the A-side and P-side spectrometers given as a function of $ t $ . . . . .	97
4.40 Efficiencies for the second detectors of the A-side and P-side spectrometers given as a function of $ t $ . . . . .	98
4.41 Elastic differential cross section distribution calculated using the Fpd reconstruction and data point from the elastic analysis . . . . .	100
4.42 Efficiencies of the trigger scintillators for the A1U and A1D detectors . . . . .	104
4.43 Efficiencies of the trigger scintillators for the A2U and A2D detectors . . . . .	104
4.44 Efficiencies of the trigger scintillators for the P1U and P1D detectors . . . . .	105
4.45 Efficiencies of the trigger scintillators for the P2U and P2D detectors . . . . .	105
4.46 Tagged halo track cross section in the four spectrometers . . . . .	107
4.47 $\xi$ -distribution of the single diffractive events in each spectrometers . . . . .	108
4.48 $\eta$ -distribution of the central tracks for $p$ and $\bar{p}$ single diffractive events . . . . .	109
5.1 Single diffractive differential cross section $\frac{d\sigma_{sd}}{d t }$ per GeV calculated using all four vertical spectrometers. The black dashed line shows the average of the cross section for each bin in $ t $ . . . . .	110
5.2 Deviation of the cross section in each bin of $ t $ from the average cross section for all the four spectrometers . . . . .	111

5.3	Difference between the cross section measurement for the four spectrometers from the average value . . . . .	112
5.4	The weighted average of the single diffractive cross section calculated by weighting the four spectrometers according to the number of events. The black dashed line shows the simple average . . . . .	117
5.5	Difference between the simple average and the weighted average for the single diffractive cross section . . . . .	118
5.6	Deviation from the from the simple average and the weighted average for the single diffractive cross section . . . . .	119
5.7	The weighted average of the single diffractive cross section calculated by weighing the four spectrometers according to the number of events .The black dashed line shows the simple average . . . . .	120
5.8	Deviation from the from the simple average and the acceptance weighted average for the single diffractive cross section . . . . .	120
5.9	The single diffractive differential cross section including the statistical error and statistical errors from the trigger efficiency calculations which are a part of the systematic uncertainty . . . . .	121
5.10	The single diffractive differential cross section calculated using bin-by-bin efficiencies, the dashed line show the mean cross section measurement . . . . .	122
5.11	Difference between the differential cross section calculated using bin-by-bin efficiencies from the mean cross section . . . . .	123
5.12	Deviation of the differential cross section calculated using bin-by-bin efficiencies from the mean cross section . . . . .	124
5.13	The single diffractive differential cross section obtained using different ansatz functions . . . . .	125
5.14	Difference between the single diffractive differential cross section obtained using different ansatz functions from the mean . . . .	125
5.15	Deviation of the single diffractive differential cross section obtained using different ansatz functions from the mean . . . . .	126
5.16	The single diffractive differential cross section using un-smeared z-vertex acceptance . . . . .	127

5.17	Difference between the single diffractive differential cross section using an un-smeared z-vertex acceptance and the mean . . . .	127
5.18	Single diffractive differential cross section $\frac{d\sigma_{sd}}{dt}$ including the statistical and systematic errors . . . . .	129
5.19	Single diffractive differential cross section $\frac{d\sigma_{sd}}{dt}$ fitted to a function $A \cdot e^{(B \cdot  t  + C \cdot  t ^2)}$ . . . . .	130
5.20	Single diffractive differential cross section $\frac{d\sigma_{sd}}{dt}$ fitted to a simple exponential function $A \cdot e^{(B \cdot  t )}$ . . . . .	131
5.21	$A \cdot e^{(B \cdot  t  + C \cdot  t ^2)}$ fit to the single diffractive differential cross section $\frac{d\sigma_{sd}}{dt}$ showing the UA4 data points at low $ t $ . . . . .	132
5.22	Variation of $\chi^2/NDF$ as a function of variation of normalization for the $D\bar{O}$ data points to include the UA4 data in the fit. The fit function used here is $A \cdot e^{(B \cdot  t  + C \cdot  t ^2)}$ . . . . .	133
5.23	Fit for the single diffractive differential cross section $\frac{d\sigma_{sd}}{dt}$ from $D\bar{O}$ including the UA4 low $ t $ data, the fit line corresponds to the minimum $\chi^2/NDF$ of the fit . . . . .	134
5.24	Single diffractive cross section as a function of $\sqrt{s}$ , theory and different experimental results . . . . .	135
5.25	Single diffractive differential cross section $\frac{d\sigma_{sd}}{dt}$ compared with the UA4 and UA8 results . . . . .	136



## LIST OF TABLES

Table		Page
1.1	List of leptons and quarks with their anti-particles, their quantum numbers and masses . . . . .	2
1.2	Leptons and quarks classified into three generations . . . . .	2
1.3	List of the force carriers in the standard model along with their anti-particles and quantum numbers . . . . .	3
4.1	Total number of events triggered during the high $\beta^*$ run broken down into run numbers . . . . .	52
4.2	Detector positions for data set 1 and data set 2 . . . . .	53
4.3	Single diffractive trigger configurations for the store 4647 . . . . .	54
4.4	Positions of the detectors for data set 1 . . . . .	58
4.5	Positions of the detectors for data set 2 . . . . .	59
4.6	The fraction of zero track events and the mean number of tracks for different types of halo events . . . . .	65
4.7	Number of different types of events which are subset of empty events to determine the noise levels . . . . .	66
4.8	Elastic band cut equations . . . . .	71
4.9	Single diffractive band cut equations . . . . .	79
4.10	Efficiencies for the FPD detectors using the TT-XT and Track-XT samples . . . . .	96
4.11	Combined efficiencies for the FPD detectors using Track-XT samples which includes trigger efficiency, hit finding efficiency and selection efficiency . . . . .	99
4.12	Integrated luminosity for different run ranges in store 4647 calculated using the ratio of inclusive jet triggers . . . . .	101
4.13	Trigger scintillator efficiencies . . . . .	106

4.14	Halo tagging efficiencies ( $\mathcal{E}_{Halo}$ ) for the vertical FPD spectrometers . . . . .	107
5.1	AU Spectrometer, number of events . . . . .	113
5.2	AD Spectrometer, number of events . . . . .	114
5.3	PU Spectrometer, number of events . . . . .	115
5.4	PD Spectrometer, number of events . . . . .	116
5.5	Number of single diffractive events in each FPD spectrometer . . . . .	117
5.6	Systematic uncertainties from the constant factors . . . . .	121
5.7	Total systematic uncertainties for the single diffractive cross section measurement . . . . .	128
5.8	Table of single diffractive differential cross section values after performing a weighted average . . . . .	130
5.9	Total single diffractive cross section ( $\sigma_{sd}$ ) calculated using different methods . . . . .	135
5.10	Total single diffractive cross section ( $\sigma_{sd}$ ) measured in different experiments . . . . .	135

# CHAPTER 1

## INTRODUCTION

### 1.1 The Standard Model

The Standard model [2] represents the current best understanding of the fundamental forces of nature. This framework includes the theory of electromagnetic, weak and strong interactions. It describes how the world is made up of fundamental particles and how they interact with each other by the exchange of force carriers. The fundamental particles are called fermions and the force carriers by which the fermions interact with each other are called bosons. Fermions are particles with half integer spin and bosons are particles with integer spin.

There are six leptons [3] and six quarks [4] along with their antiparticles that make up the known matter in the world. There are also four force mediators. The six leptons can be paired together into three groups known as ‘generations’. Three of them: the electron ( $e$ ), muon ( $\mu$ ) and tau ( $\tau$ ) have mass and electric charge, while the other three: the electron neutrino ( $\nu_e$ ), muon neutrino ( $\nu_\mu$ ) and tau neutrino ( $\nu_\tau$ ), are chargeless and have very low mass [5].

There are six quarks which are grouped into three generations, up (**u**)/down (**d**), charm (**c**)/strange (**s**), top (**t**)/bottom (**b**). Each generation of quark is heavier than the previous one. They can interact via electroweak, strong and gravitational forces. The first generation of the quarks are stable, while the heavier generations quickly decay into first generation quarks.

Table 1.1 [6] shows the list of fermions (leptons and quarks), their anti-particles and the corresponding quantum numbers. It can be seen that all the fermions have a

spin of  $1/2$ . The leptons have an electric charge of 0 or  $e$  ( $e=1.6 \times 10^{-19}$  C) whereas the quarks have a electric charge of  $+(2/3)e$  or  $-(1/3)e$ . In this table B is the baryon number and L is the lepton number. It has been found that there are three separate lepton numbers, one for each generation ( $e$ ,  $\mu$  and  $\tau$ ), which are independently conserved. The anti-particles have quantum numbers with sign opposite to their parent particle except for the total isospin T.

Table 1.1. List of leptons and quarks with their anti-particles, their quantum numbers and masses

Part.	spin ( $\hbar$ )	B	L	q ( $e$ )	$m_0$ (MeV)	antipart
$e^-$	$1/2$	0	1	$-1$	0.511	$e^+$
$\mu^-$	$1/2$	0	1	$-1$	105.658	$\mu^+$
$\tau^-$	$1/2$	0	1	$-1$	1777.1	$\tau^+$
$\nu_e$	$1/2$	0	1	0	0(?)	$\bar{\nu}_e$
$\nu_\mu$	$1/2$	0	1	0	0(?)	$\bar{\nu}_\mu$
$\nu_\tau$	$1/2$	0	1	0	0(?)	$\bar{\nu}_\tau$
u	$1/2$	$1/3$	0	$+2/3$	5	$\bar{u}$
d	$1/2$	$1/3$	0	$-1/3$	9	$\bar{d}$
s	$1/2$	$1/3$	0	$-1/3$	175	$\bar{s}$
c	$1/2$	$1/3$	0	$+2/3$	1350	$\bar{c}$
b	$1/2$	$1/3$	0	$-1/3$	4500	$\bar{b}$
t	$1/2$	$1/3$	0	$+2/3$	173000	$\bar{t}$

Table 1.2. Leptons and quarks classified into three generations

Generation	leptons	quarks	anti-leptons	anti-quarks
1st generation	$e^-$ $\nu_e$	d u	$e^+$ $\bar{\nu}_e$	$\bar{d}$ $\bar{u}$
2nd generation	$\mu^-$ $\nu_\mu$	s c	$\mu^+$ $\bar{\nu}_\mu$	$\bar{s}$ $\bar{c}$
3rd generation	$\tau^-$ $\nu_\tau$	b t	$\tau^+$ $\bar{\nu}_\tau$	$\bar{b}$ $\bar{t}$

There are four fundamental forces: electromagnetic, weak nuclear, strong nuclear, and gravity. The Standard Model describes the first three forces, but does not currently include gravity, due to difficulties in reconciling quantum theory and special relativity. Particles interact in the Standard Model by the exchange of mediators called bosons: the photon ( $\gamma$ ) for the electromagnetic force, the intermediate vector bosons ( $W^+$ ,  $W^-$  **and**  $Z$ ) for the weak force, and the gluon ( $g$ ) for the strong force. The electromagnetic and the weak forces have been unified into the electroweak force during 1960's by Sheldon Glashow, Abdus Salam, and Steven Weinberg[6].

Table 1.3. List of the force carriers in the standard model along with their anti-particles and quantum numbers

Particle	spin ( $\hbar$ )	B	L	charge ( $e$ )	$m_0$ (MeV)	antipart.
$\gamma$	1	0	0	0	0	$\gamma$
gluon	1	0	0	0	0	$\bar{g}$
$W^+$	1	0	0	+1	80220	$W^-$
$Z$	1	0	0	0	91187	$Z$

Table 1.3 provides a summary of the Standard Model force carriers. Note they all have the integer spin characteristic of bosons. The photon  $\gamma$  and the  $Z$  are their own anti-particles, while the  $\bar{g}$  is the anti-particle of the gluon, and  $W^+$  is the anti-particle of the  $W^-$ . The quantum number are subject to conservation laws. These conservation laws are invariant under *Lorentz Transformations* and *CPT* (charge/parity/time) operations, and are summarized here:

1. Mass/energy because the laws of nature are invariant for translations in time.
2. Momentum because the laws of nature are invariant for translations in space.
3. Angular momentum because the laws of nature are invariant for rotations.

4. Electrical charge because the Maxwell equations are invariant under gauge transformations.
5. Color charge is conserved.
6. Baryon number and lepton number are conserved.
7. Quark type is only conserved under the color interaction.
8. Parity is conserved except for weak interactions.

## 1.2 Quantum Chromodynamics (QCD)

Quantum chromodynamics (QCD) is the study of the interaction between particles via the strong force, and introduces an additional charge known as color, which can have three different values (*red*, *green* and *blue*). The strong force affects only particles with color (quarks and gluons). The interaction between quarks (mediated by *gluon* exchange) is similar to the electromagnetic interaction between charged particles and the photon ( $\gamma$ ). One notable difference between *Quantum Electrodynamics* (QED) and QCD, is that the gluon (unlike the photon) carries color and thus can interact with other gluons, leading to a coupling constant,  $\alpha_s$ , that varies as a function of energy (the so-called running coupling constant) instead of being a real constant as in QED, where  $\alpha \sim 1/137$ . While the other forces decrease with distance, QCD does not. As the color charges are separated, the potential energy becomes high enough to create a quark-antiquark pair out of the vacuum, resulting in two hadrons in the final state. This property of QCD, confinement, implies that there are no free quarks, and all stable particles are color neutral.

### 1.3 Kinematics and Scattering

This thesis deals with the phenomenon of diffraction. Mainly we are concerned with two types of scattering processes:

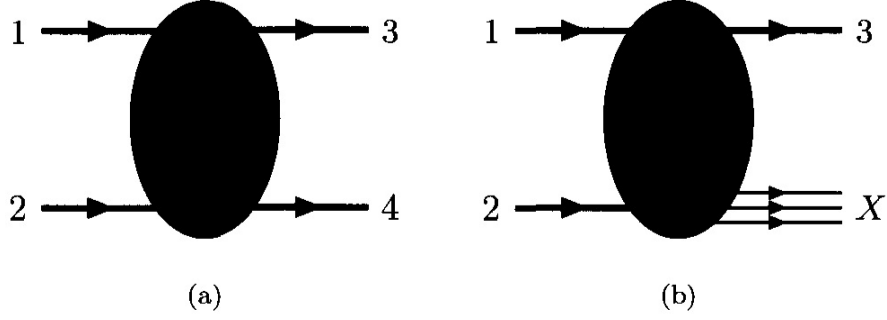


Figure 1.1. (a) Two-body exclusive scattering process represented by  $1 + 2 \rightarrow 3 + 4$  and (b) Single-particle inclusive scattering process represented by  $1 + 2 \rightarrow 3 + X$ .

- *Two-body exclusive* scattering as shown in Fig. 1.1 (a) [7].
- *Semi-inclusive*(single particle inclusive) scattering as shown in Fig. 1.1 (b) [7].

The two-body exclusive scattering processes are represented by the following equation:

$$1 + 2 \rightarrow 3 + 4$$

This process can be described by two independent variables. Elastic scattering is special case of *two-body exclusive* scattering, where the final state particles are the same but in different kinematic configuration. Elastic scattering can be written as follows

$$1 + 2 \rightarrow 1' + 2'$$

The variables to describe the *two-body exclusive* process are chosen from the three Mandelstam invariants, defined as follows:

$$s = (p_1 + p_2)^2 = (p_3 + p_4)^2 \quad (1.1)$$

$$t = (p_1 - p_3)^2 = (p_2 - p_4)^2 \quad (1.2)$$

$$u = (p_1 - p_4)^2 = (p_2 - p_3)^2 \quad (1.3)$$

Where  $p_1, p_2, p_3$  and  $p_4$  are the four momentum of the particles 1, 2, 3 and 4. The Mandelstam variables obey the following identity

$$s + t + u = \sum_{i=1}^4 m_i^2 \quad (1.4)$$

and the conservation of momentum  $p_1 + p_2 = p_3 + p_4$ . Because of this only two of the Mandelstam variables [8] are independent. Generally  $s$  and  $t$  are taken to be the independent variables. From the equations above  $s$  is the square of total center of mass of the system and  $t$  is the square of the momentum transfer. The  $s$ -channel corresponds to the particles 1,2 colliding and forming an intermediate particle that eventually decays into 3,4 whereas the  $t$  channel represents the process in which the particle 1 emits a boson and becomes the final particle 3, while the particle 2 absorbs it and becomes 4. In the relativistic high energy limit the rest masses of the particles can be neglected, which means that  $p_1^2 = m_1^2$  and  $p_2^2 = m_2^2$ . So  $s$  and  $t$  can be written as

$$s \approx 2.p_1.p_2 \approx 2.p_3.p_4 \quad (1.5)$$

$$t \approx -2.p_1.p_3 \approx -2.p_2.p_4 \quad (1.6)$$

$$u \approx -2p_1.p_4 \approx -2.p_2.p_3 \quad (1.7)$$



The semi-inclusive scattering is represented by the following equation

$$1 + 2 \rightarrow 3 + X$$

this process requires three independent variables for the system description because the system  $X$  is not on mass. Generally  $s, t$  and the invariant mass  $M^2 = (p_1 + p_2 - p_3)^2$  of the system  $X$ . The invariant mass of this system is also called the missing mass of the system. The Mandelstam variables are defined with the  $p_4$  replaced with  $p_X$ . Since  $X$  is not a real particle,  $M^2$  is not a fixed number.

Another commonly used kinematic variable is Feynman's  $x_F$ :

$$x_F = \frac{|p'_z|}{p_z}$$

where  $|p'_z|$  is the momentum in the  $z$  direction of the final particle. In the high energy limit when the average transverse momentum ( $p_T$ ) of the particle is low compared to  $M$  then the Feynman  $x_F$  can be written as

$$x_F \approx 1 - \frac{M^2}{s} \quad (1.8)$$

Then the variable  $t$  can be written as a function of  $x_F$

$$t \approx \frac{p_T^2}{x_F} \quad (1.9)$$

Single-inclusive processes, can be described by either of the following sets of variables:

$$[s, x_F, p_T^2] \text{ or } [s, t, M^2].$$

Another important variable which is used to in the description of single-inclusive processes is *rapidity*. For a particle with energy  $E$  and momentum  $p_z$  the rapidity  $y$  is defined as

$$y = \frac{1}{2} \ln \frac{E + p_z}{E - p_z}$$

Rapidity transforms additively under Lorentz boost along the  $z$  axis, because of this rapidity difference is invariant under longitudinal boosts and remains same in all collinear frames of reference. For a particle of zero mass the rapidity and the pseudo-rapidity coincide. This is also the case in the high energy approximation. For the case of single-inclusive process the rapidity difference between the final state particle and the disassociated system  $X$  is given by

$$\Delta y \approx \ln \left( \frac{s}{M^2} \right)$$

#### 1.4 Units used in high energy physics

In high energy particle physics, the energy, momentum and mass are expressed in electron volts (eV). By definition the electron volt is a unit of energy and is equal to the energy gained by a electron when it passes a potential difference of 1 volt. In S.I. units this is equal to  $1.602 \times 10^{-19}$  J. In normal circumstances the energy would be expressed in terms of eV, momentum as  $\text{eV}/c$  and mass as  $\text{eV}/c^2$ . But here all these quantities are expressed in terms of eV, this is called natural units, or Heaviside-Lorentz units [9] This means that Planck's constant ( $\hbar$ ), the velocity of light ( $c$ ), and the Boltzmann constant  $k_B$  are such that

$$\hbar = c = k_B = 1 \tag{1.10}$$

this also implies that

$$\epsilon_0 = \mu_0 = 1 \tag{1.11}$$

## CHAPTER 2

### THEORETICAL OVERVIEW

#### 2.1 Diffraction

Hadronic processes are typically classified into two main categories

1. Hard Processes.
2. Soft Processes.

Soft processes are mainly characterized by the energy scale of the order of hadron size  $R$ , where  $R \sim 1$  fm. The momentum transferred squared of this process is such that  $|t| \sim 1/R^2$ . The cross sections of the soft process depend exponentially on  $|t|$  such that  $d\sigma/dt \sim e^{R^2|t|}$  and large- $|t|$  events are highly suppressed. Theoretically perturbative QCD is inadequate to describe the soft processes because of the large length scales. On the other hand the hard processes [10, 11, 12, 13] are characterized by two or more energy scales, one is still the hadron size and the other is the so called “hard” energy scale. The value of the momentum transfer in these processes is greater than 1.0 GeV. The higher value of the momentum transfer of these processes allows the use of perturbative QCD, but a part of these processes is still non-perturbative. The “factorization theorems” allows the separation of the perturbative processes from the non-perturbative ones. Loosely speaking diffraction is generally a soft process.

##### 2.1.1 Definition of Diffraction

The term diffraction was first used in high energy physics during the 1950s by the Landau school. The term “diffraction” is used in analogy with the optical

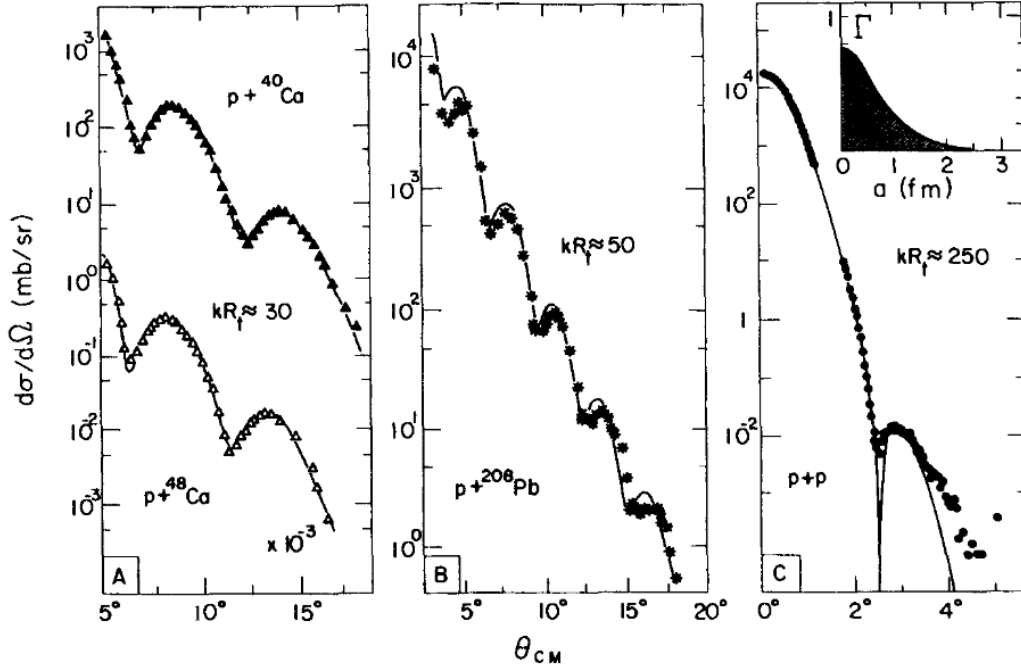


Figure 2.1. Diffraction in nuclear and hadronic physics. Diffractive hadronic processes have behaviour similar to that of optical diffraction. The plots show the change in the cross section as a function of  $\theta$ , which is proportional to  $|t|$ .

phenomenon of diffraction. From optics the diffracted intensity of light at small angles and large wave numbers  $k$  is given by

$$I(\theta) \approx I_0 (1 - Bk^2\theta^2) \quad (2.1)$$

where  $B \propto R^2$  and  $k\theta$  is the momentum transfer. The diffractive hadronic process have a similar kind of behavior. Their cross sections are shown in Fig. 2.1, and vary according to the following equations

$$\frac{d\sigma}{dt} = \frac{d\sigma}{dt} \bigg|_{t=0} e^{-B|t|} \approx \frac{d\sigma}{dt} \bigg|_{t=0} (1 - B|t|) \quad (2.2)$$

for small  $|t|$  and at high energies  $|t| \propto \theta^2$ . The slope parameter  $B$  is proportional to the square of the radius of the target hadron.

Diffraction is generally described as “a high energy reaction in which no quantum numbers are exchanged between the colliding particles.” In the definition above the condition that there should be no exchange of quantum number between the colliding particles is a necessary condition but is not a sufficient one for diffraction to happen. The requirement that no quantum numbers can be exchanged between the particles other than that of the vacuum does not eliminate all possible backgrounds to the diffractive processes. The backgrounds, however, are asymptotically smaller and smaller, thus the inclusion of “high energy” in the above definition. Examples of diffractive processes are

1. **Elastic Scattering**, when the same incident particles come out after the collision.

$$1 + 2 \rightarrow 1' + 2'$$

2. **Single Diffraction**, while one of the particles comes out unscathed after collision, while the other gives rise to a bunch of other final state particles or resonances with the same same quantum numbers.

$$1 + 2 \rightarrow 1' + X_2$$

3. **Double Diffraction**, when both the colliding particles gives rise to bunch of final state particles or resonances with the quantum numbers of the initial particles.

$$1 + 2 \rightarrow X_1 + X_2 \tag{2.3}$$

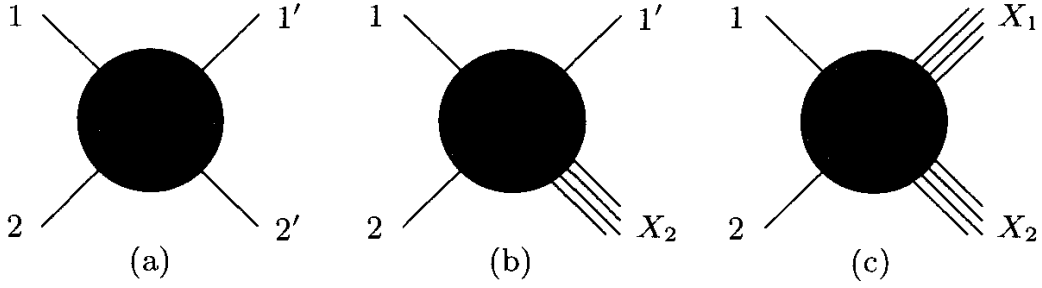


Figure 2.2. Diagram to illustrate diffractive scattering (a) Elastic scattering (b) Single diffraction (c) Double diffraction.

From the point of view of experimental observation the diffractive reactions are defined by Bjorken [14], “a diffractive reaction is characterized by a large, non exponentially suppressed, rapidity gap in the final state.” This definition implies that in the case of diffractive events there is expected to be a large rapidity gap between the final state particles  $X_1$  and  $X_2$ , while rapidity gaps from background are exponentially suppressed. If the rapidity gap between the final state particles is given as  $\Delta\eta$ , the distribution of the diffractive events are given as

$$\frac{dN}{d\Delta\eta} \sim \text{constant}$$

whereas the distribution for the non-diffractive background is given by

$$\frac{dN}{d\Delta\eta} \sim e^{-\Delta\eta}.$$

### 2.1.2 Soft Diffraction

The largest component of diffractive scattering is Soft Diffraction. In this class of events large momentum transfer does not occur and no short distance physics is involved. The momentum is carried from one beam to another through a mediator

that carries the quantum numbers of vacuum, this particle is called the Pomeron( $P$ ). Elastic scattering is one example of soft diffraction. Elastic scattering accounts for the largest component of soft diffraction. Such a process can be written as

$$p + \bar{p} \rightarrow p + \bar{p}, \quad (2.4)$$

In this reaction both the initial particles survive in the final state, and no other

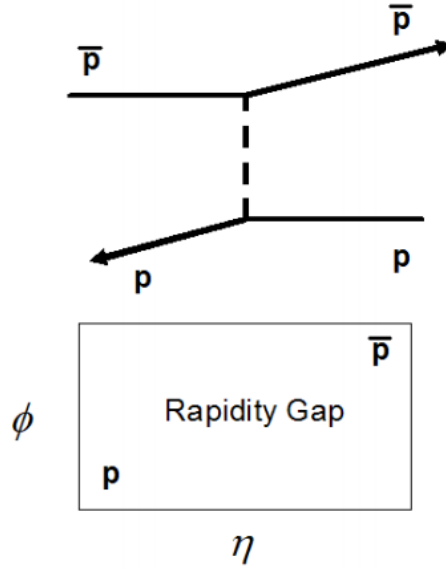


Figure 2.3. Illustration of elastic scattering in  $p\bar{p}$  collision at the Tevatron and its  $\eta - \phi$  topology.

particles are produced in the reaction. There is a large region between the scattered proton and anti-proton which is devoid of any particles. This region is called rapidity gap. Figure 2.3 shows the elastic scattering process and its experimental signature. In addition to the elastic scattering there are a few other soft diffractive process,



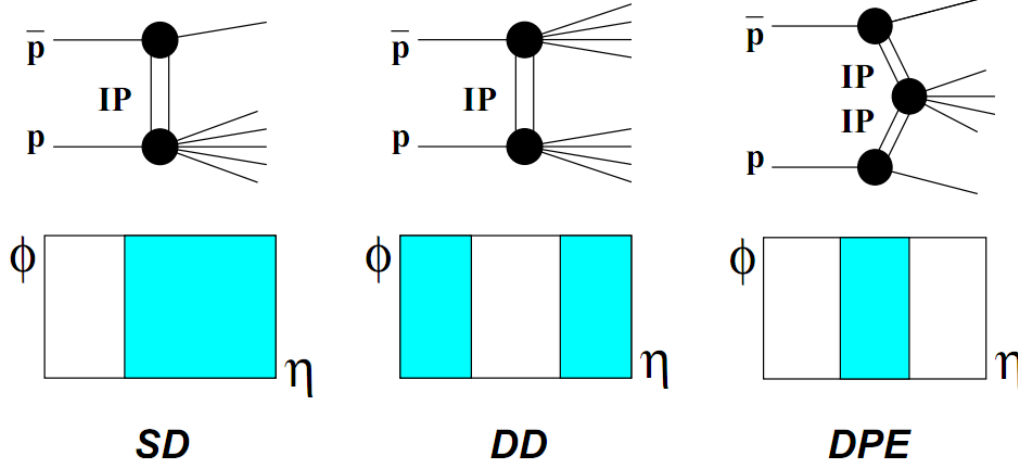


Figure 2.4. Diagrams and  $\eta - \phi$  topologies to describe single diffraction(SD), double diffraction(DD) and double pomeron exchange(DPE) processes in  $p\bar{p}$  collision.

Fig. 2.4 (SD) illustrates the important ones. In the case of single diffraction [15] the collision process can be written using the following equation

$$p + \bar{p} \rightarrow (p \text{ or } \bar{p}) + X, \quad (2.5)$$

where either the initial proton or anti-proton remain intact in the final state while the other  $p$  or  $\bar{p}$  hadronizes to produce a system  $X$ . Figure 2.4 (DD) shows the double diffractive process [16]

$$p + \bar{p} \rightarrow X_1 + X_2, \quad (2.6)$$

this occurs when an object with the quantum numbers of the vacuum (pomeron,  $\mathbb{P}$ ) is exchanged between the colliding  $p$  and  $\bar{p}$ , causing the incident particles to break up and produce two mass clusters  $X_1$  and  $X_2$  separated by a rapidity gap. The last

example in Fig. 2.4 (DPE) is the so-called double pomeron exchange process [17], which can be written as

$$p + \bar{p} \rightarrow p + X + \bar{p}. \quad (2.7)$$

These events are characterized by leading proton and anti-proton in the final state and large rapidity gaps in the forward regions on both sides. In the central region there is a mass resonance or a diffractive system.

### 2.1.3 Hard Diffraction

In addition to the above mentioned soft diffraction there is hard diffraction, in which there is a hard partonic scattering in addition to large rapidity gaps. Such kind of events might have forward, central, or multiple rapidity gaps. Figure 2.5 shows examples of hard diffraction observed at the Tevatron, namely dijet production.

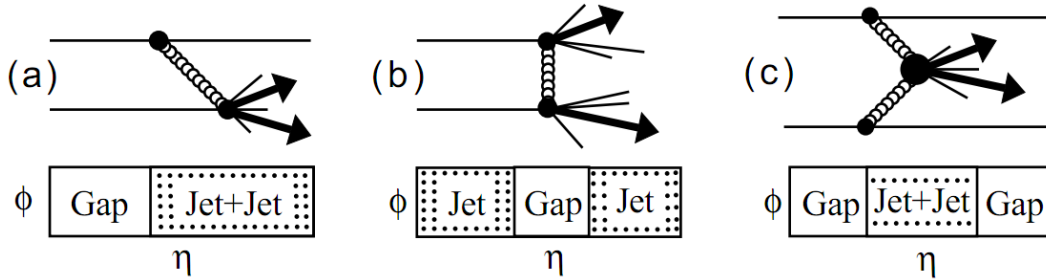


Figure 2.5. Description of hard diffraction in  $p\bar{p}$  collision at the Tevatron and its  $\eta - \phi$  topology for (a) hard single diffraction (b) hard double diffraction and (c) double pomeron exchange.

In addition to dijets hard single diffraction may produce other heavy particles such as a  $W$ ,  $Z$ , or heavy quark.

## 2.2 Regge Theory

The soft diffraction phenomenon described in Section 2.1.2 is described phenomenologically by Regge Theory [18], which considered the initial and final states of the scattering process and proposed a relation for hadron-hadron scattering cross section as a function of center of mass energy. This was done without any knowledge of the interaction mechanism in hadron-hadron scattering, as it pre-dated the advent of quark theory in 1964 [19]. A detailed derivation of Regge theory is given in [20]; the main points of the theory are described in the following sections.

### 2.2.1 The $s$ and $t$ channel processes

In the case of  $2 \rightarrow 2$  collision process,  $a + b \rightarrow c + d$ , the two Mandelstam variables defined in terms of the four momenta of the particles are

$$s = (p_a + p_b)^2 \text{ and } t = (p_a - p_c)^2, \quad (2.8)$$

where  $\sqrt{s}$  is the center of mass energy of collision and  $t$  is the square of the four momentum transfer between particle  $a$  and  $c$ . This gives rise to two different interaction topologies, the  $s$ -channel processes and the  $t$ -channel processes. In the  $s$ -channel process the particles  $a$  and  $b$  annihilate to produce a real particle or a resonance. In the case of the  $t$ -channel processes there is a exchange of virtual particle between the particles  $a$  and  $b$ . The square of the four momentum transfer between the particle is negative in this case.

### 2.2.2 Crossing symmetry

The  $s$ -channel and  $t$ -channel processes are shown in Fig. 2.6. The amplitudes for these two processes are related to each other by crossing symmetry, which states

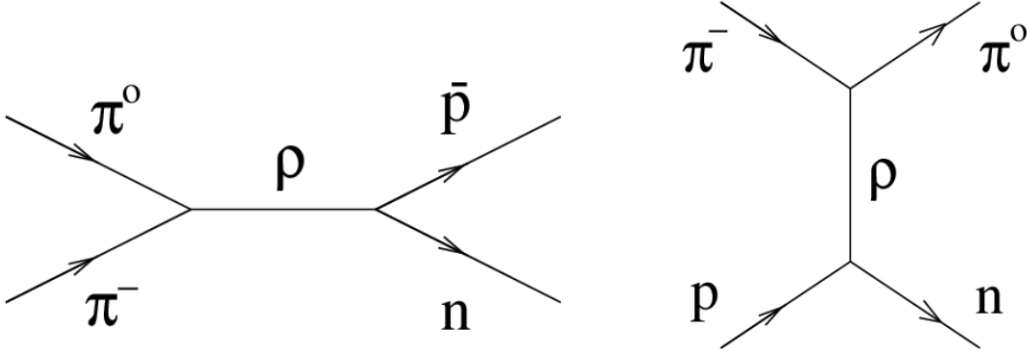


Figure 2.6. Crossing symmetry between (a)  $s$ -channel and (b)  $t$ -channel process.

that the scattering amplitudes of the  $s$ -channel process  $a+b \rightarrow c+d$  and the  $t$ -channel in the crossed process  $a+\bar{c} \rightarrow \bar{b}+d$ , with  $s$  and  $t$  interchanged, are equal [21]. This implies that the scattering amplitudes  $\mathcal{A}(s, t)$  for the  $s$ -channel and crossed  $t$ -channel processes are equal even if they are different physical processes.

### 2.2.3 Optical theorem

The optical theorem gives the relationship between the total cross section  $\sigma_{tot}$  and the imaginary part of the forward scattering amplitude  $\mathcal{A}(s, 0)$

$$\sigma_{tot} \approx \frac{\mathcal{A}(s, 0)}{s}, \quad (2.9)$$

in this case the amplitude is called forward because the momentum transfer is zero. The momentum transfer is given by

$$\cos(\theta) = 1 + \frac{2t}{s}, \quad (2.10)$$

where  $\theta$  is the scattering angle in the center of mass frame, in this case  $t = 0$  is zero scattering.

### 2.2.4 Scattering amplitude

Regge Theory describes the scattering process in the asymptotic limit. In the “Regge Limit,”  $s \rightarrow \infty$  with  $s/t$  fixed. The scattering amplitude for the  $t$ -channel process is the sum of all the partial wave amplitudes that correspond to all the possible exchanges with different angular momenta. The  $s$ -channel process is then the crossed process. Its scattering amplitude is obtained through crossing symmetry by interchanging  $s$  and  $t$ . The scattering amplitudes are then generalized using complex angular momentum [22, 23], which states that particles can have only integer angular momenta( $l$ ), but in the complex  $l$ -plane the scattering amplitudes may have poles. These poles are called “Regge poles,”  $\alpha_n(t)$ . In the Regge limit only the right most pole in the complex  $l$ -plane, the one with the largest real part contributes to the scattering amplitude. The scattering amplitude is then given as a function of center of mass energy,  $\sqrt{s}$

$$\mathcal{A}(s, t) \sim s^{\alpha(t)}, \quad s \gg |t| \quad (2.11)$$

Equation 2.11 holds for all the scattering processes.

### 2.2.5 Regge trajectories

In order to explain hadron scattering Chew and Frautschi plotted the total angular momentum ( $J$ ) for particular sets of hadrons versus the square of their masses( $M^2$ ). Figure 2.7 shows the Chew-Frautschi plot [20] for meson resonances in  $\pi^- \pi^0 \rightarrow \bar{p} n$  collisions. It can be seen that the data is in a straight line which means that for hadrons with same quantum number, the total angular momentum  $J$  is proportional to  $M^2$ . This linear dependence between  $J$  and  $M^2$  is called “Regge trajectory.” In this given case the trajectory is called  $\rho$ -trajectory and is denoted by  $\alpha_R(t) = \alpha_R(0) + \alpha'_R t$ .

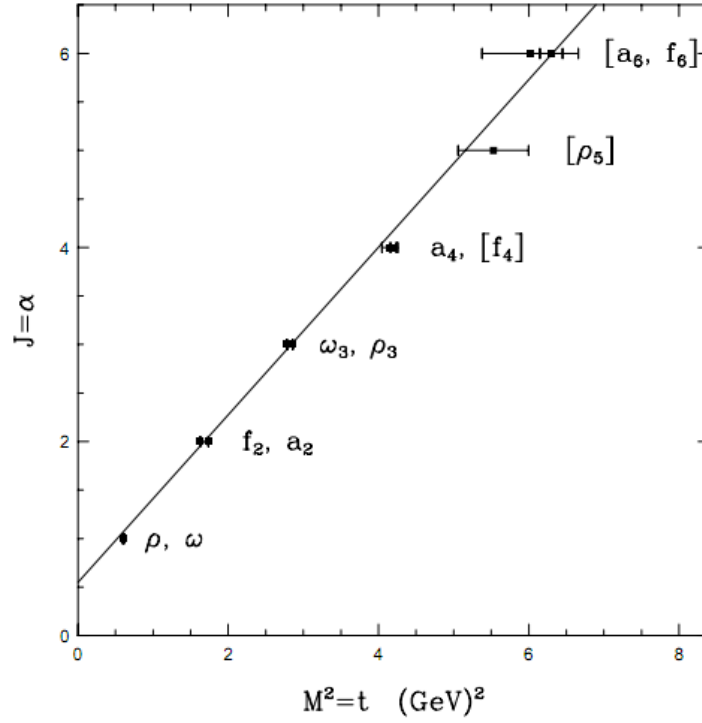


Figure 2.7. Chew-Frautschi plot for the  $t$ -channel process in  $\pi^-\pi^0 \rightarrow \bar{p}n$  collisions.

Using the Regge approach the scattering amplitude of the  $s$ -channel process is related to the  $t$ -channel process by crossing symmetry. In this case the  $t$ -channel process is given by  $\pi^-p \rightarrow \pi^0n$ . The amplitudes are equal in magnitude in this case, but since the energy dependence of the amplitude is driven by Regge trajectory, the two processes are also connected Chew-Frautschi plane. The  $s$ -channel data lies in the  $t > 0$  region whereas the  $t$ -channel data lies in the  $t < 0$  region. This property that the amplitude can be extrapolated across the  $t = 0$  boundary is called analyticity.

### 2.2.6 Total scattering cross section

The total cross section for hadron-hadron scattering behaves in the following way

$$\sigma_{tot} \sim S^{\alpha(0)-1}, \quad (2.12)$$

in this case  $\alpha(0)$  is the intercept of the Regge's trajectory. This intercept is less than unity for the  $\rho$ -trajectory so the total cross section decreases with increasing  $s$  for this type of scattering, as noted by Pomeronchuk and Okun [24]. The prediction that the total cross section decreases with increasing  $s$  was validated at low energies, but the scattering data for  $pp$  and  $p\bar{p}$  (Fig. 2.8 [25]) shows that the total cross section begins to increase above  $\sim 20$  GeV. This was also predicted by Pomeranchuk [26].

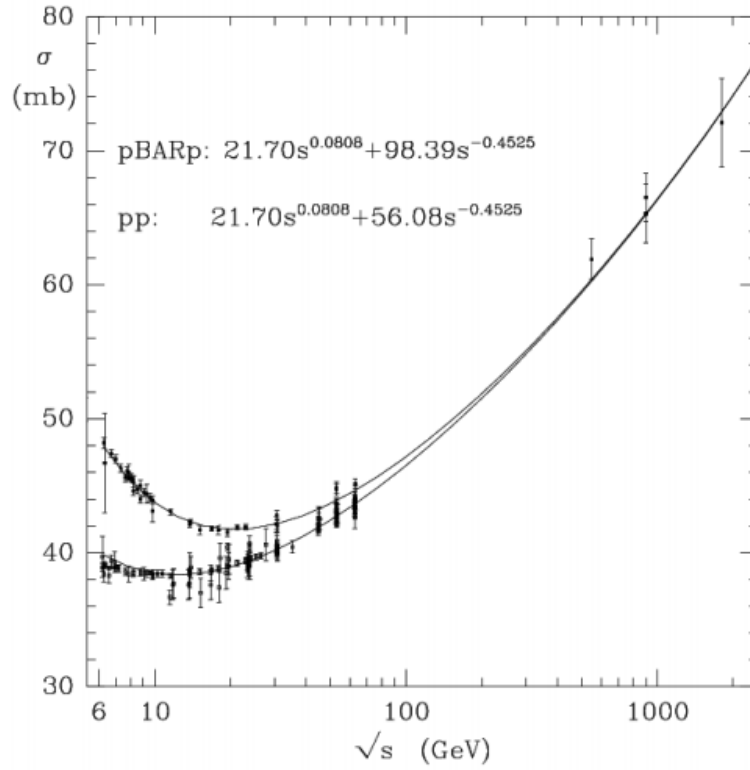


Figure 2.8. Total cross section in  $p\bar{p}$  collision shown in the upper curve and  $pp$  collision shown in the curve below.

### 2.3 The pomeron

Pomeranchuk theoretically showed that the the total cross-sections for particle and anti-particle collisions are equal to each other at high energies [24]. This is known as Pomeranchuk's theorem. Since the cross-sections are same for particles and anti-particles, the exchanged objects between the two must be able to couple equally with particle as well as its anti-particle, implying that it must have quantum numbers of the vacuum, that is, no charge, no color, zero spin, isospin and baryon number.

As these particles are responsible for the increase in the total cross sections with  $\sqrt{s}$ , they must be lying on a different Regge trajectory in such a way that their intercept is greater than unity. The particles were dubbed “pomeron.” Donnachie and Landshoff parametrized the total cross sections in  $pp$  and  $p\bar{p}$  collisions as being made up of two contributions [25]

$$\sigma_{tot} = As^{\alpha_{IP}(0)-1} + Ys^{\alpha_R(0)-1} \quad (2.13)$$

as shown in Fig. 2.8. In these fits the first term corresponds to the rise in the cross section and is same for both  $pp$  and  $p\bar{p}$  collisions. The intercept for the first term is found to be  $\alpha_{IP}(0) = 1.08$ . This is called the pomeron contribution. The second term which is responsible for the fall in the cross-sections is called the reggeon contribution. The reggeon contribution is universal and all types of scattering process have the same trajectory and  $s$  dependence.

The pomeron on the other hand has an intercept greater than unity,  $\sim 1.08$ , this means that the cross section would continue to rise with increasing  $\sqrt{s}$  and violate unitarity at very high center of mass energies. The total hadron-hadron scattering cross section is kept under control because of multiple pomeron exchanges. When more than one pomeron are exchanged, they contribute to the total cross section with



alternating signs. The pomeron intercept changes very slowly with  $\sqrt{s}$ . At  $\sqrt{s} = 1.8$  TeV,  $\alpha_{IP}(0)$  is almost constant because multiple pomeron exchange is only about 10% of the total cross section [27]. There are also two types of pomeron trajectories, the one described before with  $\alpha_{IP}(0) = 1.08$  is called the “soft pomeron.” This can describe a number of soft diffractive processes. A “hard pomeron” was proposed by Donnachie and Landshoff [28] in order to explain the results of the HERA experiment [29]. The intercept for the hard pomeron,  $\alpha_{IP}(0) \sim 1.4$ .

#### 2.4 Single Diffraction Dissociation

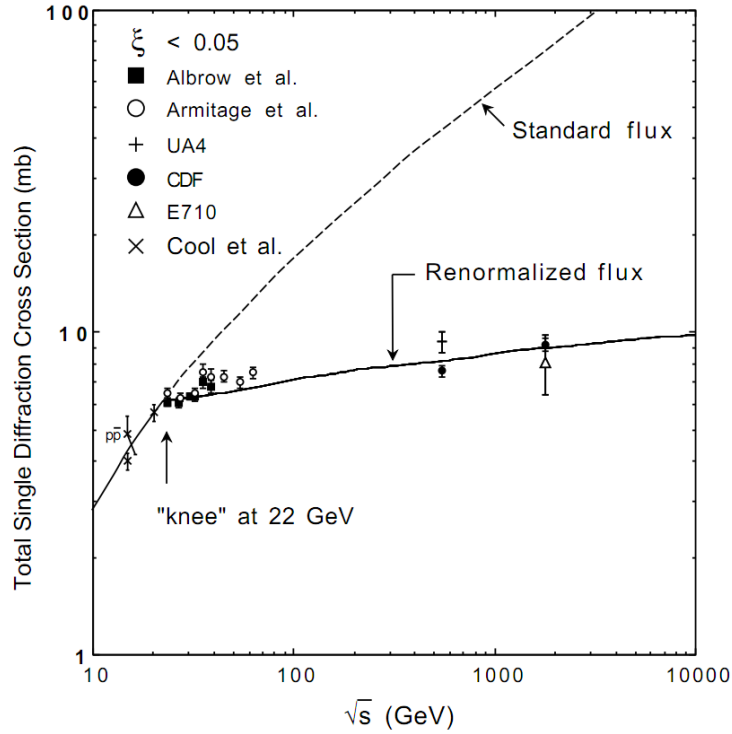


Figure 2.9. Single diffractive differential cross section as a function of  $\sqrt{s}$ , theory and different experimental results.

This dissertation focuses on the single diffraction dissociation process( $p + \bar{p} \rightarrow p(\bar{p}) + X$ ) described in the previous sections. The Regge Theory approach describes the experimental data approximately up to the energy range  $\sqrt{s} < 60$  GeV [30]. As the center of mass energy of experiment's increased, unitarity problems began to arise. In Regge Theory the pomeron trajectory has an intercept  $\alpha(0) > 1$  and the  $s$  dependence of the total cross section is  $\sigma_{tot} \sim s^{(\alpha(0)-1)}$ ; at higher energies as  $s \rightarrow \infty$  the total cross section violate the Froissart bound [31], which is given as

$$\sigma_{tot} \propto s^{(\alpha(0)-1)} > \ln^2 s \quad (2.14)$$

In 1994 the CDF experiment made the measurements of total cross section [32], the elastic cross section [33], and single diffractive cross section [34] at  $\sqrt{s} = 540$  GeV and  $\sqrt{s} = 1800$  GeV. These measurements showed that there is little  $s$  dependence of  $\frac{d\sigma_{sd}}{dM_X^2}$  between  $\sqrt{s} = 20$  GeV and 540 GeV. This was opposite to the expectation of Regge Theory. To explain the experimental data Goulianos in 1995 [35] proposed that the “pomeron flux,”  $f_{IP}$  should be renormalized to unity when the integral over the  $\xi - t$  space exceeds unity. This renormalization cancels out the  $\sigma_{tot} \sim s^{(\alpha(0)-1)}$  dependence. Figure 2.9 shows the experimental data and the renormalization of the pomeron flux and the standard pomeron flux. It can be seen that the renormalized flux shows good agreement with the experimental data.

## CHAPTER 3

### EXPERIMENTAL APPARATUS

The analysis described in the following chapters was carried out at the DØ detector in Fermi National Accelerator Laboratory (FNAL), which is located in Batavia, Illinois. FNAL was commissioned in 1967 by the US Atomic Energy Commission. Originally it was named the National Accelerator Laboratory. On May 11, 1974, the laboratory was renamed Fermi National Accelerator Laboratory in honor of 1938 Nobel Prize winner Enrico Fermi[36]. The Fermilab Tevatron was the world’s largest and highest energy superconducting accelerator for more than fifteen years before recently being surpassed by the CERN Large Hadron Collider (LHC). There are two collider experiments, CDF (Collider Detector at Fermilab) and DØ (named due to its location in the Tevatron ring) that make use of the Tevatron’s proton and anti-proton beams.

Two major discoveries to support the Standard Model were made at Fermilab. The first one was the discovery of the bottom quark in 1977 [37], while the second major discovery was that of the top quark in 1995 [38, 39]. Apart from these two, the first direct observation of CP violation was performed in 1999 [40]. The  $\tau$  neutrino which was predicted by the standard model was seen in 2001 [41].

#### 3.1 Accelerator Complex

The Tevatron started operation in 1983 with a 512 GeV proton beam. In 1984 it attained a beam energy of 800 GeV for the proton and anti-proton beams. The first  $p\bar{p}$  collisions were observed at the CDF detector with a center of mass energy  $\sqrt{s} =$

1.6 TeV in 1984. The accelerator first attained  $\sqrt{s} = 1.8$  TeV in 1986. Collider Run I began in 1992 and also included the DØ detector. During the 4 years of this run the accelerator delivered a total integrated luminosity of  $130 \text{ pb}^{-1}$  to the DØ and CDF detectors. From the end of Run I in 1996 through March, 2001 both the detectors as well as the accelerator were upgraded. The next run, Collider Run II began in 2001 with a higher  $\sqrt{s} = 1.96$  TeV and will end in September, 2011.

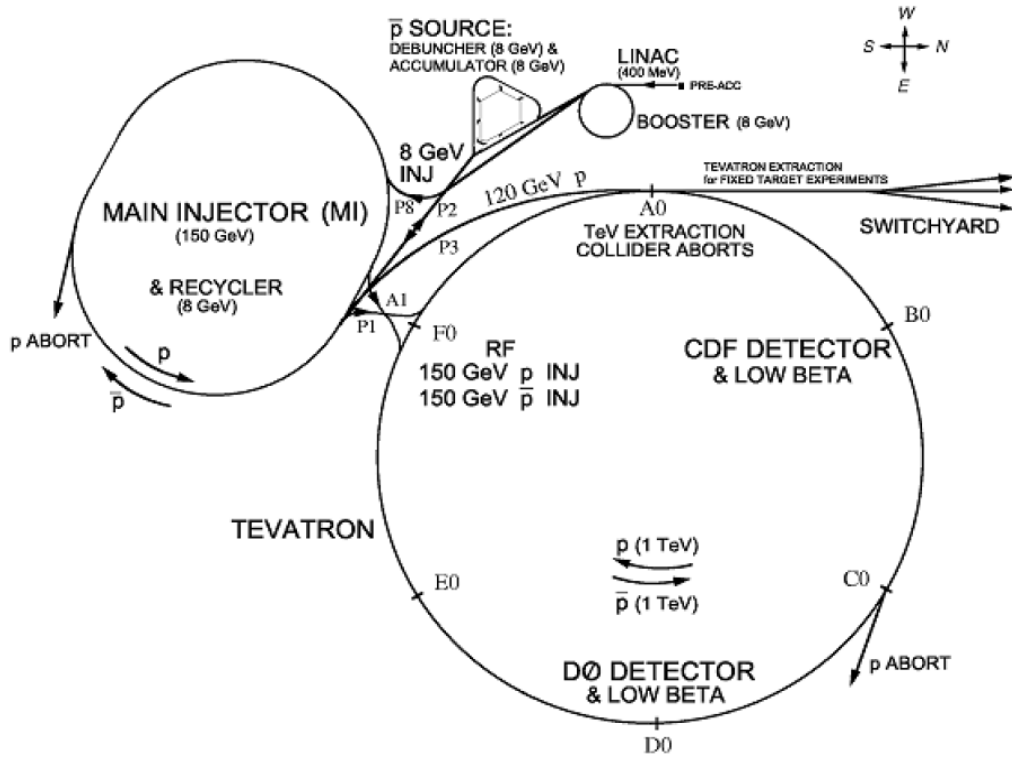


Figure 3.1. Schematic diagram of the Fermilab accelerator complex.

The accelerator complex is made up of several individual particle accelerators as shown in Fig. 3.1. These accelerators increase the energy of the particles in steps. The main components of the accelerator complex are the following:

- Proton Source (pre-accelerator, Cockcroft-Walton generator, 0-750 keV)

- Linac (750 keV- 400 MeV)
- Booster (400 MeV- 8 GeV)
- Main Injector (8 GeV- 150 GeV)
- Tevatron (150 GeV- 980 GeV)
- Recycler and Anti-Proton Source.

### 3.1.1 Proton Source

The pre-accelerator is made up of the proton source and the Cockcroft-Walton generator. In the proton source hydrogen atoms are fed into a magnetron source which produces  $H^+$  ions. The  $H^+$  are then fed into the Cockcroft-Walton generator [42]. The Cockcroft-Walton generator is a commercially available generator that uses a series of charged capacitors to accelerate the  $H^+$  ions to 750 keV energy. The  $H^+$  ions are then sent to the Linac.

### 3.1.2 Linac

The  $H^+$  ions are passed to the Linac (Linear accelerator) after they leave the pre-accelerator. The Linac is a 130 m long linear accelerator which accelerates the  $H^+$  ions from 750 keV to 400 MeV. It uses oscillating electric fields in the radio frequency range (RF) inside copper cavity drift tubes to accelerate  $H^+$ . The Linac is made up of two parts, the first one is called drift tube linac (DTL) and the second one is called side coupled Linac (SCL). The DTL is 79 meters long and is made up of five electrically resonant copper cylinders whose resonance frequencies are at 201.24 MHz. The SCL on the other hand is made up of seven resonant cavities at 805 MHz. The main difference between the DTL and SCL is that the DTL accelerates the beam in every cycle while the SCL accelerates the beam every fourth cycle to compensate for the difference in the resonance. At the end of the Linac the bunches are passed

through a carbon foil which strips all the electrons from the ions leaving the bare protons only.

### 3.1.3 Booster

The Booster is the first of the synchrotrons in the accelerator complex. It takes the 400 MeV bunches from the Linac and accelerates them to 8 GeV. The Booster has a diameter of 151 meters and is located 20 feet below ground. It is made up of 96 combined function dipole-quadrupole magnets and 17 dual gap cavity resonators. The magnets, which create the quadrupole and the dipole fields are used to focus and bend the beam so that it stays in a circular orbit along the synchrotron. The proton bunches are accelerated using the 17 RF cavities which have a period of 0.033 seconds. The RF frequency also keeps the particles in bunch centered in a RF bucket. After the bunches have been accelerated to 8 GeV, they are sent to the Main Injector.

### 3.1.4 Main Injector

The Main Injector (MI) is a circular synchrotron of circumference 3 kilometers. It was commissioned in 1999 and is made up of 18 RF cavities and separate dipole and quadrupole magnets. The Main Injector has several modes of operation, “shot setup mode,” “ $\bar{p}$  production mode,” and “protons for NuMI.” In the shot setup mode the proton bunches are accelerated for injection into the Tevatron. It takes the protons from the booster at 8 GeV and accelerates them to 150 GeV. Seven bunches of protons are taken at a time and are accelerated to 150 GeV, after this these seven bunches are combined into one bunch using a process called coalescing. This process is repeated 36 times. In the case of the anti-protons, four bunches are loaded at a time and accelerated to 150 GeV. The anti-proton bunches are not combined. This process is repeated 9 times. In the end of the shot setup we have 36 bunches of protons and 36

bunches of anti-protons. These are spaced 396 nano-seconds apart in time. In the  $\bar{p}$  production mode the main injector takes the bunches of protons from the Booster and accelerates them in 120 GeV in a process called stacking. The accelerated bunches are then sent to the  $\bar{p}$  source. The Main Injector is also used to get 120 GeV proton for NuMI which is a neutrino experiment.

### 3.1.5 Tevatron

The Tevatron, a synchrotron with a circumference of 4 miles, receives the 150 GeV proton and anti-proton bunches from the MI. In the Tevatron the particles are accelerated to 980 GeV using RF cavities. The steering and focusing of the beams is done by approximately 1000 dipole and quadrupole magnets. These magnets are superconducting magnets operating at a temperature of 4.3 K and at a field strength of 4.2 T. The particle beams collide with each other at two predetermined points D0 (DØ Detector) and B0 (CDF Detector) at a center of mass energy,  $\sqrt{s} = 1.96$  TeV.

### 3.1.6 Anti-Proton Source and Recycler

The anti-proton source produces the anti-protons for the collisions. This is made up of three main parts: the Target Station, the Debuncher, and the Accumulator. The 120 GeV protons from the Main Injector are sent to the Target Station, which is made up of a nickel target. The 120 GeV proton strikes the nickel target to produce anti-protons and many other secondary particles. From the products of this collision 8 GeV anti-protons are selected using magnets on the basis of charge and momentum. These 8 GeV anti-protons are sent to the Debuncher. The Debuncher is a triangular synchrotron of length 90 meters. Inside the Debuncher the anti-protons are maintained at 8 GeV energy and cooled (reduction of momentum spread) using a process called stochastic cooling. After this process the anti-protons are sent to

the accumulator which is a storage ring. It shares the same tunnel as that of the Debuncher. The anti-protons are kept in the accumulator until they are extracted to the Main Injector.

The anti-protons are extracted from the Tevatron after every store and are stored in the Recycler. The Recycler, which shares the same tunnel as the MI, is meant for longer term storage of the anti-protons. It is used to increase the number of the anti-protons available for collisions.

### 3.2 The DØ Detector

The DØ detector is one of two detectors on the Tevatron ring. The primary purpose of the detector is to perform fundamental research on the nature of matter. It was commissioned in 1992 during Tevatron Run I and recorded data with high efficiency through 1996 producing many notable physics results including the top quark discovery. The detector was upgraded between the end of Run I and the start of Run II in 2001 [43] to handle higher luminosities. During the upgrade a new tracking system, calorimeter and muon system[44] were installed. Figure 3.2 shows an overview of the main parts of the DØ central detector[45], which include:

- Central Tracking System.
- Calorimeter System.
- Muon System
- Luminosity Monitor

The DØ Forward Proton Detector is not shown here, since it is located more than 20 m upstream and downstream of the central detector—it is shown in Sec. 3.3. The Data Acquisition System (DAQ) takes the data from these sub detectors and uses 128 different triggers to select them. The triggered data is written to the storage.



In the following sections the different sub detector systems are described using the references [43, 46, 47].

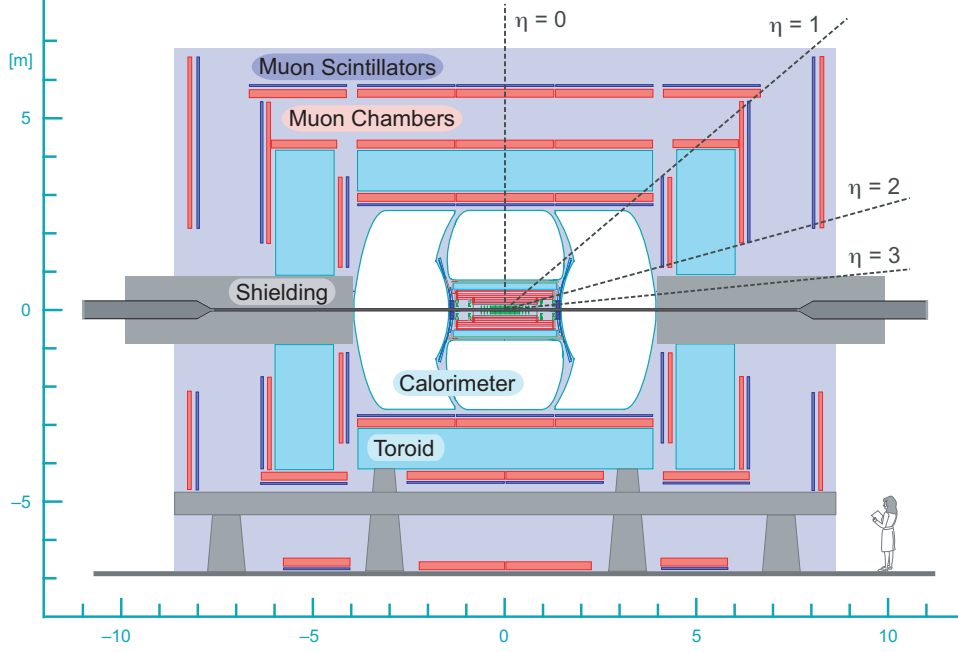


Figure 3.2. Overview of the upgraded Run II DØ detector.

### 3.2.1 Central Tracking System

The Tracking system is important for determining the position and momentum of the charged particles; the overview of the tracking system is shown in Fig. 3.3. The DØ tracking system is made up of the Silicon Micro-Strip Tracker (SMT)[48], the Central Fiber Tracker (CFT)[49], the Central Preshower Detector, the Forward Preshower Detector, and a solenoid. The SMT and the CFT were added to the DØ detector during the Run II upgrade. The SMT is the first layer of detector with which the particles interact after collision. The CFT overlaps the SMT over a range  $|\eta| < 2.0$ , with the combination providing a precise measurement of the vertex and

tracks. One of the roles of CFT is to provide fast track triggering in the range  $|\eta| < 1.6$  because it can process the track signal faster than the SMT. The superconducting solenoid magnets covering the SMT and CFT generate a magnetic field of 1.92 T. The magnetic field bends the charged particles inside the tracker, enabling the momentum measurement. The preshower detectors were also added during the Run II upgrade to enhance the photon and electron identification.

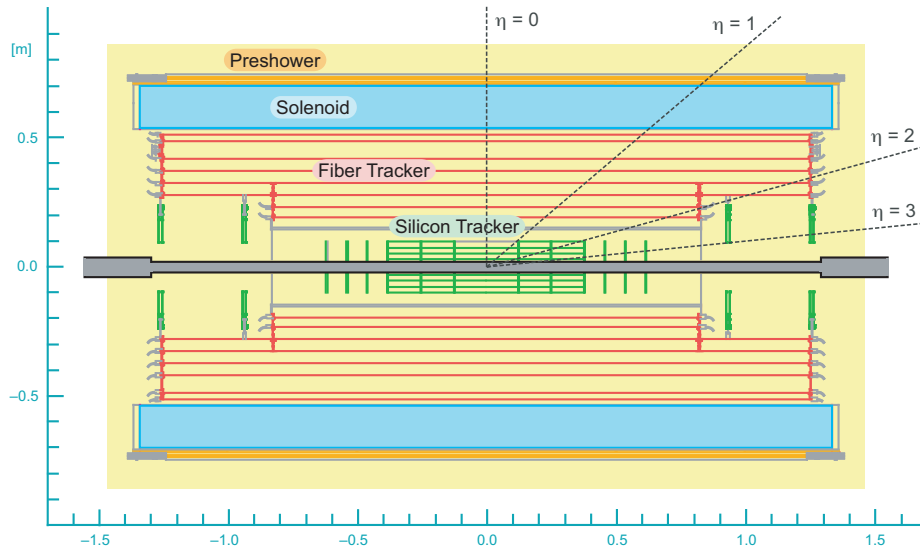


Figure 3.3. Overview of the Run II DØ Central Tracking System showing the SMT, CFT, Solenoid and the Preshower Detectors.

### 3.2.1.1 Silicon Micro-Strip Tracker

The main motivation behind the SMT is to measure the central vertex and to trigger on events with displaced vertices from events with  $b$ -quarks. It covers the full interaction region (25 cm) about the interaction point. The SMT is made up of six barrels in the central region, with the ends of each of the barrels capped by disks on each side called F-Disks (12 F-Disks) and at the most forward position on each side

there are two more disks called H-Disks (4 H-Disks). Figure 3.4 shows the structure of the SMT detector.

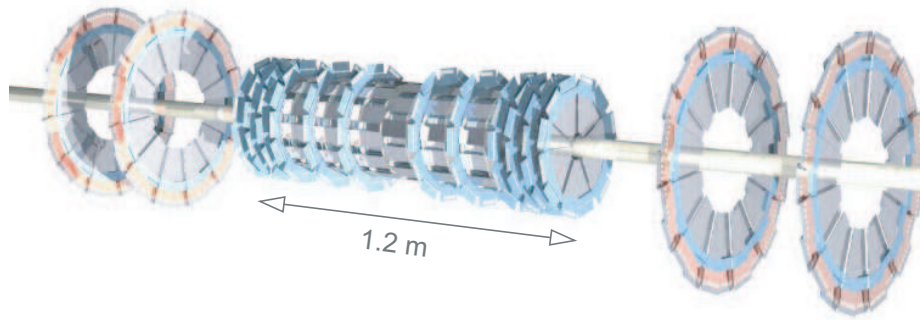


Figure 3.4. The Silicon Micro-Strip Tracker showing the 6 barrels, 12 F-Disks and 4 H-Disks.

The barrel is made of individual units of detectors called ladders whereas the disks are made up of wedges. The ladders and wedges are made up of single and double sided micro-strip detectors. The barrel initially consisted of four layers of detectors, but prior to Run IIb an extremely radiation hard inner layer called Layer 0 was added to allow the tracker to maintain its resolution as the inner layers degraded due to radiation damage. The F-disks are made up of 12 double sided wedge detectors. The H-Disk detectors are made up of 24 wedge detectors each, each wedge has 2 single sided detectors glued back to back. The Micro-Strip detectors are made up of silicon sensors. Each sensor is a one sided n-type silicon wafer  $300\ \mu\text{m}$  thick with a variable strip pitch depending on the detector location. As the charged particles pass through the detectors they produce electron hole pairs. The silicon strips are connected to the SVXIIe chips which measure the deposited charge in each strip using analog to digital converters (ADC). All the chips are read out using a hybrid readout called High Density Interconnect (HDI).

### 3.2.1.2 Central Fiber Tracker

The CFT is a scintillating fiber detector that surrounds the silicon detector and lies in the magnetic field created by the Solenoid. The main purpose of the CFT is to reconstruct the tracks and measure the momentum of the tracks. The CFT is also crucial in fast triggering because the singles are processed faster in the CFT than SMT. The CFT overlaps the SMT in the range  $|\eta| < 2.0$  and provides triggering in the range  $|\eta| < 1.6$ .

The CFT is made up of 76,800 scintillating fibers which are arranged on 8 concentric carbon fiber support cylinders. The fibers are arranged on the cylinders in 2 doublets, one is oriented along the axial direction (z) of the detector and the second is oriented along a stereo angle on  $\phi = +3^\circ$  (u) and  $\phi = -3^\circ$  (v). The fibers are placed within a spatial resolution of  $25 \mu\text{m}$  and the whole setup provides a hit resolution of  $100 \mu\text{m}$  in  $r$  and  $\phi$ . The individual fibers are made up of scintillating fibers of diameter  $835 \mu\text{m}$  which are doped with a fluorescent dye. These scintillator fibers are attached to clear fiber wave guides which carry the light to the Visible Light Photon Counters (VLPCs). The fiber are read out at only one end, while the other end is covered with sputtered aluminum having very high reflectivity  $\approx 90\%$ .

### 3.2.1.3 Solenoid Magnet

Beyond the CFT is the superconducting solenoid magnet that encloses the tracking system. This magnet produces a magnetic field of 2 T. The purpose of this magnet is to maximize the momentum resolution of the tracking systems and increase the resolution of the track recognition. This superconducting magnet is made up of two layer coils and is 2.75 m long, 0.32 m thick and it has a radius of 0.6 m. The

conductors of the magnet are made up of superconducting Rutherford-type cables of Cu:NbTi with strands of pure aluminum for stability.

#### 3.2.1.4 Preshower Detectors

The preshower detector is located outside the Solenoid Magnet and is made up of central preshower (CPS) and forward preshower (FPS). The purpose of the Preshower Detector is to improve the electron and photon identification. The Preshower detector can be either used as a calorimeter to measure energy or it can be used as a tracking detector to match the tracks with the EM shower in the calorimeter. Both the CPS and the FPS are made up of triangular scintillators with embedded wavelength shifting fibers [50]. The output of the CPS and the FPS are fed into the same VLPC and AFE readout system of the CFT.

#### 3.2.2 Calorimeter

The main purpose of the calorimeter[51] is to measure the energy of the particles that pass through it. The DØ calorimeter is a sampling calorimeter, which consists of alternating layers of sampling media and absorber plates. It measures the visible energy in discrete intervals (sampling), and uses calibration constants to correct to the total energy [43]. In addition to energy measurement the DØ calorimeter also provides some particle identification and coarse tracking.

The DØ calorimeter is made up of Liquid Argon which is the active medium and Uranium plates which acts as the absorber. The absorber material induces a electromagnetic and hadronic shower in the high energy particles and absorbs the low energy particles. The active medium on the other hand samples the ionization energy produced by the showering particles. Liquid argon which is the active medium in this case has the disadvantage that it needs to be housed in cryostat and an operating

temperature of 80 K has to be maintained. Once the calorimeter is installed it is radiation hard and easy to maintain.

The DØ Calorimeter has three main parts one central and two endcaps (EC). The individual detectors are housed in cryostat as can be seen in Fig. 3.5. In each of the cryostats the uranium plates are placed in liquid argon filled chambers. In each of the detectors there is electromagnetic (EM), fine hadronic and coarse hadronic section located radially outwards from the interaction point. The EM calorimeter is made up of the thinnest depleted uranium plates of 3 mm thickness in the central region and 4 mm in the EC regions. The fine hadronic calorimeter is made up of 6 mm thick plates of an alloy of uranium and niobium. The coarse hadronic calorimeter is made up of copper plates of thickness 46.5 mm in the central region and stainless steel plates in the forward region.

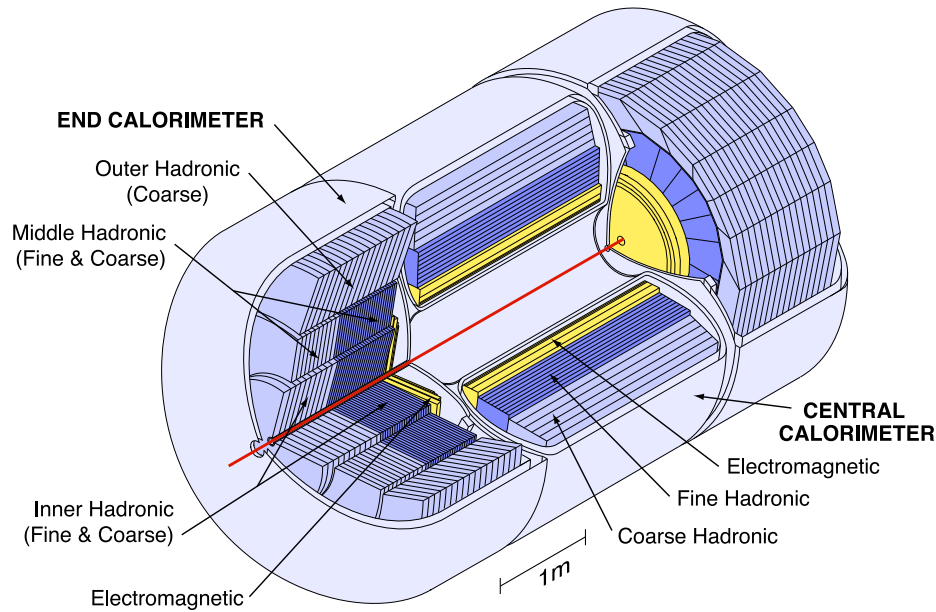


Figure 3.5. Schematic view of the DØ Liquid argon and Uranium Calorimeter.

Each layer of the calorimeter is divided into cells. The cells are offset to reduce the possibility of a particle to escape without showering. The unit cell of the calorimeter is the basic unit from which signal is collected. Figure 3.6 shows the structure of the unit cell of the calorimeter. This is made up of a absorber plate followed by a 2.3 mm gap filled with liquid argon followed by readout electronics and the a final gap. The ion pairs produced by the ionization of liquid argon are collected by the electrodes in a strong electric field. The absorber plates are the ground electrodes, while the copper plates from the anodes are placed at a potential of 2.0 to 2.5 kV.

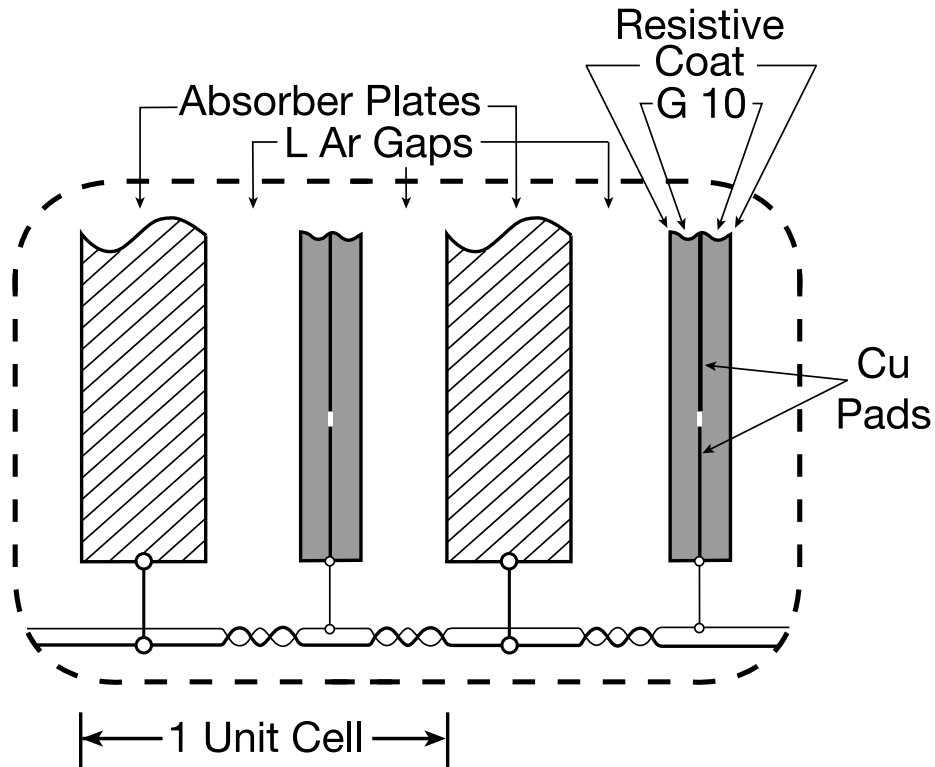


Figure 3.6. Diagram of the unit cell structure of the Calorimeter.

A readout cell in the calorimeter is a combination of several adjacent unit cell to increase to total measured charge. The size of readout cell in the calorimeter is

$\Delta\eta \times \Delta\phi = 0.1 \times 0.1$ . A set of such readout cells aligned outward from the interaction point is called a tower. The Calorimeter tower geometry is shown in Fig. 3.7, the centers of the cells in the tower all lie in a line originating from the detector center.

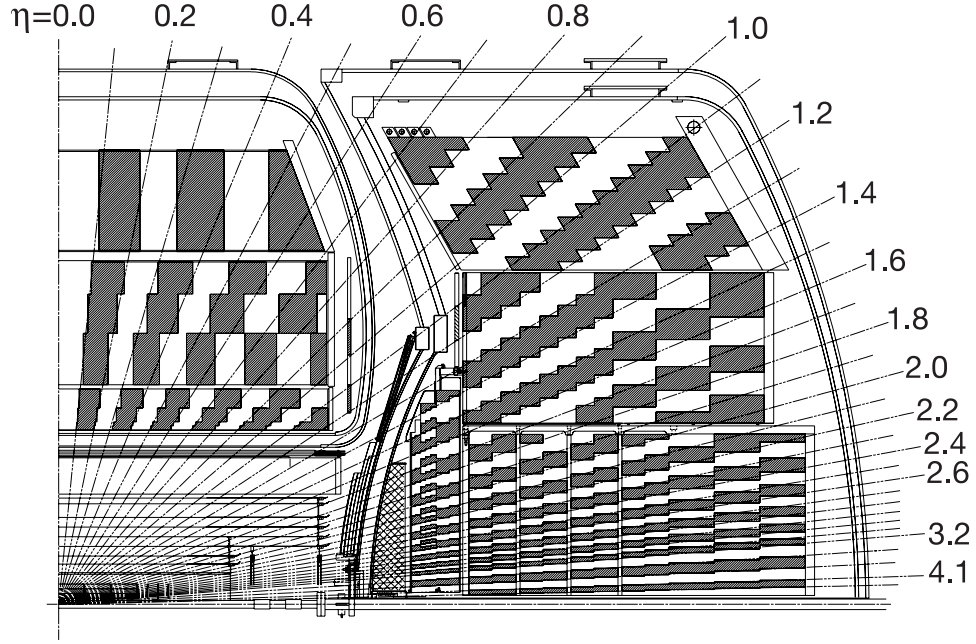


Figure 3.7. Quadrant cross sectional view of the pseudo-projective towers in the Calorimeter.

The DØ calorimeter was designed to be a compensating calorimeter, which means that the response of the calorimeter is the same for both the electromagnetic and hadronic objects. The ratio of electron and pion response,  $e/\pi \sim 1.05$  in the calorimeter



### 3.2.3 Muon System

The Muon System is the outermost detector of the DØ detector system. This detector is dedicated to the detection of muons only. Since the muons are much heavier than the electrons, a muon of the energy 3.5 - 4.0 GeV passes the inner detectors without depositing much of its energy. That is why the Muon Detector is the outermost detector set. It is shielded from the debris of the electronic and hadronic shower because of the calorimeter material. The Muon System is synchronized to the Tevatron clock for timing, so that it can reject the cosmic muons. The Muon system is composed of the following major components

- The wide angle Muon Spectrometer ( $|\eta_{det}| < 1.0$ ).
- Forward angle Muon Spectrometer ( $1.0 < |\eta_{det}| < 2.0$ ).
- Solid iron toroidal magnet.

The Wide Angle Muon Spectrometer (WAMUS) is made up two types of detectors, proportional drift tubes (PDT) and scintillator tiles. The PDTs are used for tracking and the scintillator tiles are used for timing and triggering. There are three layers of detectors in the WAMUS. The A layer is closest to the interaction point and is located inside the toroid, whereas the B and C layers are outside the toroid. The A layer has four decks of drift tubes, while the B and C layers have three decks of drift tubes each. There are scintillators in the A and C layers only. There is a small region in WAMUS which is devoid of any tracking from  $225^\circ < \phi < 310^\circ$  because this region is occupied by the Calorimeter support structure.

The Forward Muon System (FAMUS) has a similar structure as that of the WAMUS, but it uses Mini Drift Tubes (MDTs) and scintillation pixels instead of the PDTs. The FAMUS uses MDTs due to the high rates of forward particle production. The MDTs have a shorter drift time for the electrons, are more radiation hard, and

provide a better coordinate resolution. There are also three layers of wire chambers. All the layers in the FAMUS have both the MDTs and pixels.

The Toroid is essentially a magnetic box fitting around the calorimeter. The central part is made up of twenty coils each while the end part is made up of eight coils with eight turns each. There are square holes at the ends of the toroid for the beam pipe, The polarity of the toroid is regularly reversed and it runs at a magnetic field of 6% less than 2T.

### 3.2.4 Luminosity Monitor

The Luminosity Monitor, which was designed to provide a measurement of the luminosity at the DØ interaction point, is made up of hodoscopes of scintillation counters and mounted on the inside face of each end cryostat near the beam pipe. The hodoscopes are made up of 24 wedges of plastic scintillators and are located at  $|z| \approx 140$  cm. They have a pseudo-rapidity coverage of  $2.7 < |\eta_{det}| < 4.4$  and are located inside the magnetic field of the solenoid. They provide a timing resolution of 200 ps and is read out using photomultiplier tubes.

The Luminosity Monitors measure the rate of inelastic collisions by detecting the showers of particles that result from the dissociation of the scattered proton and anti-proton. The luminosity ( $\mathcal{L}$ ) is calculated using the average number of inelastic collisions per bunch crossing and is corrected for the acceptance ( $\mathcal{A}$ ) and efficiency ( $\epsilon_{lm}$ ) of the luminosity monitors as shown in the equation 3.1 where  $f$  is the beam crossing frequency.

$$\mathcal{L} = \frac{f \cdot \bar{N}_{inelastic}}{\mathcal{A} \cdot \epsilon_{lm}} \quad (3.1)$$

In addition to the luminosity measurement the timing information from the north and the south LM can be used to make a measurement of the collision vertex

(fast  $z$ ). One of the important uses of the luminosity monitor in this analysis is the use of inactivity in the luminosity monitor (LM veto) which is used for selecting diffractive events at the trigger level and in offline data analysis.

### 3.2.5 Trigger and Data Acquisition System

During the running of the experiments, only a few interesting events out of millions of collisions are selected to be recorded. This is because the total collision rate exceeds the rate at which the data can be recorded. The data recording rate is limited mainly because of the dead time of the electronics. The cost of the storage media also puts a constraint on the amount of data that can be recorded. The data to be recorded is chosen based on the different physics process, the probability of their occurrence, and the research goals of the collaboration.

The physics events are selected through the use of triggering system. The triggering system monitors the detectors subsystem for coarse information and quickly decides if the event is an interesting physics event and if it should be recorded according to some predefined criterion. The DØ trigger system is divided into three trigger levels, Level 1 (L1), Level 2 (L2) and Level 3 (L3). The trigger system reduces the few MHz input rate to L1 to typically 50 Hz out of L3 written to disk. This reduction is accomplished by various selections on different detectors, that ideally have a high efficiency and a large rejection. A less intelligent mechanism for reducing the rate is to apply a prescale factor which randomly propagates only some fraction of the events of a specific type. The prescale values can be changed during a store depending on the instantaneous luminosity.

The L1 Trigger is a hardware trigger which implements simple algorithms using Field Programmable Gate Arrays (FPGAs). At L1 each individual trigger decision is sent to “L1 AND-OR” terms. There are 256 such terms which are combined into 128

different triggers. The data acquisition rate is much faster than the trigger decision processing rate so the acquired data is stored in a buffer. It takes approximately  $3.3 \mu\text{s}$  to process the trigger after which the events are either selected to be sent to the L2 trigger or rejected based on the L1 trigger decision or the prescale. At L1 the rate is reduced from 1.7 MHz to 1.6 KHz. At L2, the information from different subdetectors can be combined to further reduce the rate to about 800 Hz. L2 uses logic cards and microprocessors in VME crates running 500 MHz alpha processors. The L2 processing times are also more than the data rate so it also uses a buffer to store the L1 data for up to  $100 \mu\text{s}$  while the trigger decision is being made. Data comes in to the L3DAQ system in parallel from 63 VME readout crates each corresponding to a part of the detector or the trigger framework. Each crate is read by a single board computer (SBC), which is powered by a single 933 MHz Pentium-III processor with 128 MB of RAM each. The data is moved out of the SBCs over an ethernet network over a 1 Gb/s optical fiber to the L3 farm. The L3 farm partially reconstructs each event and based on the physics selection criterion they are selected. The selected events are sent to the collector machine over the network where they are written to the disks.

### 3.3 The DØ Forward Proton Detector

The Forward Proton Detector (FPD) subsystem [52] was added to the DØ detector system during Run II. The main objective of this detector is to detect the scattered protons and anti-proton at small angles, of the order of 1 mrad with respect to the central beam. The motivation behind this detector is the study of diffractive events because the detection of the forward protons and anti-protons gives full access to the kinematics of diffractive and elastic events. Without the FPD these scattered protons would escape undetected down the beam pipe.

### 3.3.1 FPD Layout

The FPD is made up of nine momentum spectrometers along the beam pipe. The spectrometers use the beam magnets along with scintillating fiber position detectors to measure the momentum of the outgoing forward protons. They are located at distance of 20 - 60 m from the DØ central detector. Figure 3.8 shows the location of the 8 FPD quadrupole spectrometers (each with two detectors), which use the low beta quadrupole magnets to measure the momentum and angle of the scattered protons. The dipole spectrometer is located further down stream on the anti-proton side, and is not used in this analysis.

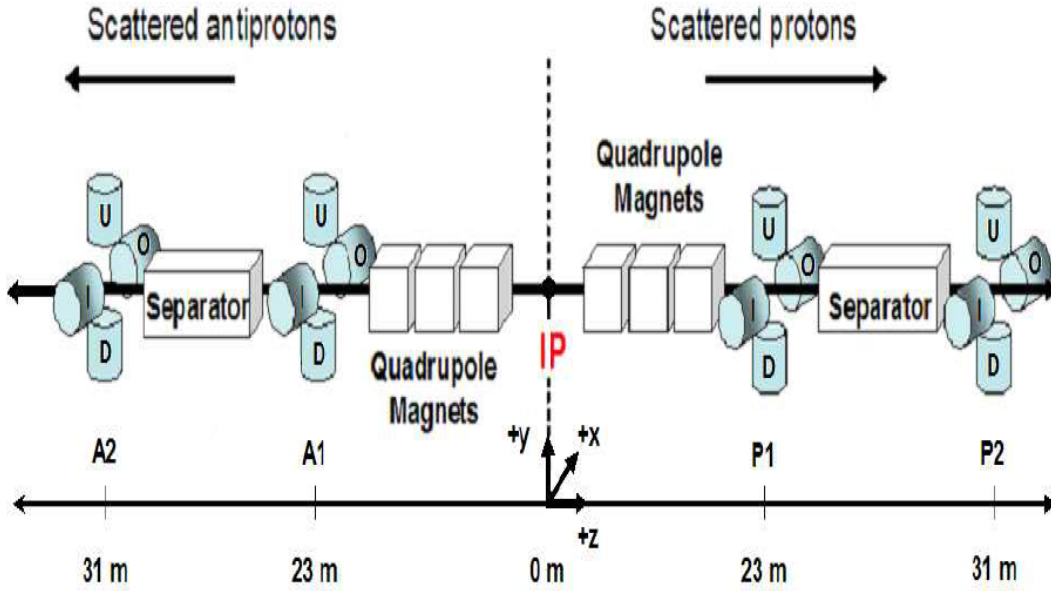


Figure 3.8. Layout of the Forward Proton Detector System.

The position detectors are housed within stainless steel containers called Roman Pots (RP). This allows them to operate very close to the beam but outside the beam pipe's ultra high vacuum (UHV). The  $p$  and  $\bar{p}$  transverse a 200  $\mu\text{m}$  thick window to

enter the position detectors. The pots are retracted during the injection of the beam into the accelerator, and can be controlled remotely to place the detectors within a few mm of the beam during periods of stable beam.

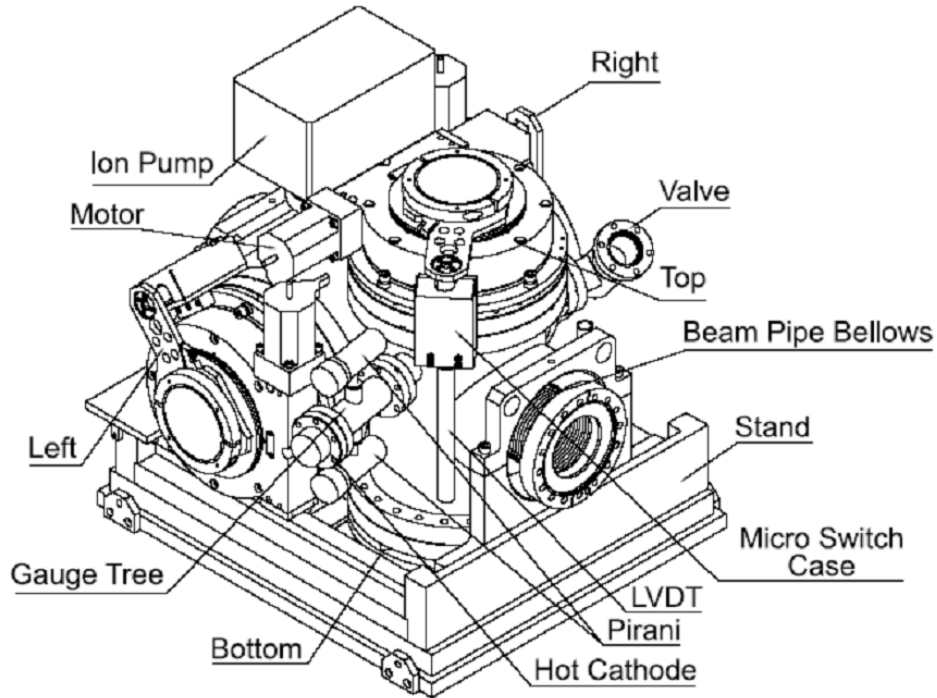


Figure 3.9. Forward Proton Detector castle.

The Romans pots are housed in stainless steel structures called castles as shown in Fig. 3.9. The castles are located at different distances relative to DØ interaction point. There are two types of castles, one houses four RPs and is called a quadrupole castle and the other types houses only one Roman Pot and is called a dipole castle. There are two quadrupole castles on the outgoing proton side called P1 and P2, on the anti-proton side there are four castles A1, A2 which are after the quadrupole castles and D1, D2 which are dipole castles.

Each castle is mounted on a stand whose position can be adjusted within  $\pm 15$  mm with an accuracy of 0.1 mm. The pots inside the castle are connected to a driving mechanism by which the pots are moved towards or away from the beam remotely. The motion control system uses a step motor and threaded worm gear to move the pots about  $8\text{ }\mu\text{m}$  for each half turn of the motor. A system of cylindrical and conical bearings are used to adjust the pot alignment. A linear variable differential transformer (LVDT) is used to monitor the position of the pot. Steel bellows are used to interface the castles to the beam pipe and also to allow the movement of the pots inside the vacuum.

### 3.3.2 FPD Position Detector

The Position Detectors consists of channels of 0.8 mm thick, double clad square scintillating fibers bundled in stacks of four parallel fibers forming a structure measuring  $0.8 \times 3.2\text{ mm}^2$  in area. A schematic diagram of the position detectors are shown in Fig. 3.10. When a particle passes through the active region of the detector it results in 10 scintillation photons in the blue region of the visible spectrum with a peak at about 475 nm. The fibers are glued in a plastic frame which maintain both the position of the fibers and the relative alignment between them. The different channels are separated from each other by a  $250\text{ }\mu\text{m}$  plastic fins which reduce optical cross talk between the channels. One end of the active detector element is coated with a aluminum layer of thickness of  $3\text{ }\mu\text{m}$  to increase the light output. The other end of the active element is spliced to a clear waveguide fiber of the same dimension.

The detectors are made up of six layers of fibers  $(u, u', v, v', x, x')$  and are arranged in three planes  $(u, v, x)$ . The planes are made up of “primed” and “unprimed” fiber layers, the primed fiber layers are offset from the unprimed fiber layers by two-thirds of a fiber width. The layers  $u$  and  $v$  are oriented at  $\pm 45^\circ$  with respect to the

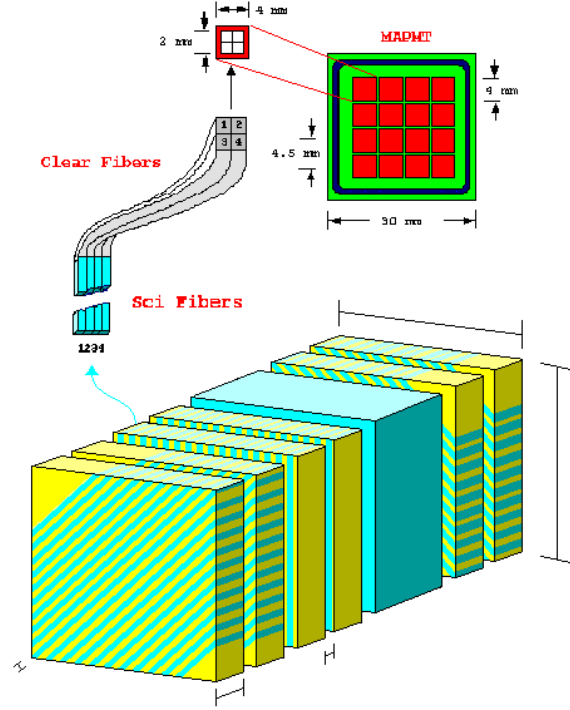


Figure 3.10. Schematic diagram of FPD position detectors and MAPMT.

detector bottom whereas the  $x$  plane is oriented at  $90^\circ$ . There are 20 channels for the  $u$ ,  $v$  planes and 16 channels for the  $x$  plane, giving a total of 112 channels for each detector and a total of 2016 channel for the whole the system.

The clear waveguide fibers takes the light from one detector channel to one pixel of a 16 channel multi-anode photomultiplier tube (MAPMT). There are seven MAPMTs for each detector. Optical cross talk and light attenuation is small in these optical waveguide fibers. The clear fibers are held position by a diamond polished plastic support called a cookie. The cookie maintains the position of the clear fibers with respect to the MAPMT pixels. The entire detector including the seven MAPMTs and the cookies are mounted in Roman Pots.

The MAPMT signals are sent to the Amplifier/Shaper (A/S) boards located nearby. The amplified signals are sent to the central DØ platform using 16 channel



ribbon cables. These signals are then processed by the transition patch panels (TPP) made up of transformers and resistors so that the charge of the signal can be reduced to a level which can be processed by the CFT electronics. A trigger manager of the type used by the muon system is also used here, it uses the FPD hit information to make a trigger decision. The trigger signal is sent directly to the Luminosity Monitor electronics without any amplification.

### 3.3.3 FPD Timing Detector

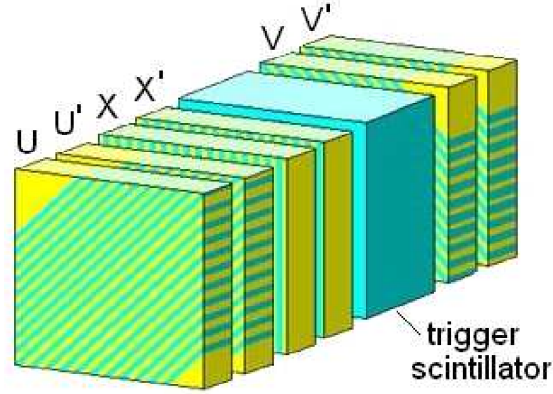


Figure 3.11. Schematic view of the six scintillating fiber layers and the scintillating block of one detector.

In addition to the fiber-based position detectors, each Roman Pot also contains a trigger scintillator as shown in Fig. 3.11. The purpose of this detector is to measure the proton time of flight for background and halo rejection. The particles outside the main beam core that travel with the beam are halo particles. The scintillator hit times are read out by the TDC system based on the Luminosity Monitor electronics. The TDC system sets an in-time bit if a particle passed through the detector at the

expected time and sets a halo-bit if it the particle passes through the detector at a early time.

## CHAPTER 4

### ANALYSIS

#### 4.1 Data Sample

The data used in this analysis is taken from store 4647 of the Tevatron. This run was in February 17<sup>th</sup> and 18<sup>th</sup> in 2006. This was optimized for alignment and physics of the Forward Proton Detectors at DØ and was called the high  $\beta^*$  run. During this run the beam was tuned so that the FPD detectors could be brought much close to the beam axis than during the standard high luminosity operations. The initial instantaneous luminosity for this store was about  $0.5 \times 10^{30} \text{ cm}^{-2} \text{ s}^{-1}$ . The beam emittance was  $20\pi \text{ mm/mrad}$  for the proton beam and  $17\pi \text{ mm/mrad}$  for the anti-proton beam. The total integrated luminosity for the store was  $30 \text{ nb}^{-1}$ . A total of about 20 million events were recorded during the store using a special trigger list optimized for elastic and diffractive physics.

##### 4.1.1 High $\beta^*$ run

The main goal of the high  $\beta^*$  run was the study of elastic and diffractive physics. The Tevatron injection tune was used with  $\beta^* = 1.6 \text{ m}$  at the DØ interaction point. The low  $\beta$  squeeze to the standard  $\beta^* = 0.35 \text{ m}$  lattice was omitted. Since only one proton and one anti-proton bunch were injected, the separators were not needed, so they were not turned on resulting in more parallel beams. Combined with the additional scraping to lower the halo, the net result was that the detectors could be brought much closer to the beam during this run. Figure 4.1 shows the position on the detectors during the normal store and the high  $\beta^*$  stores. Since the detectors are much

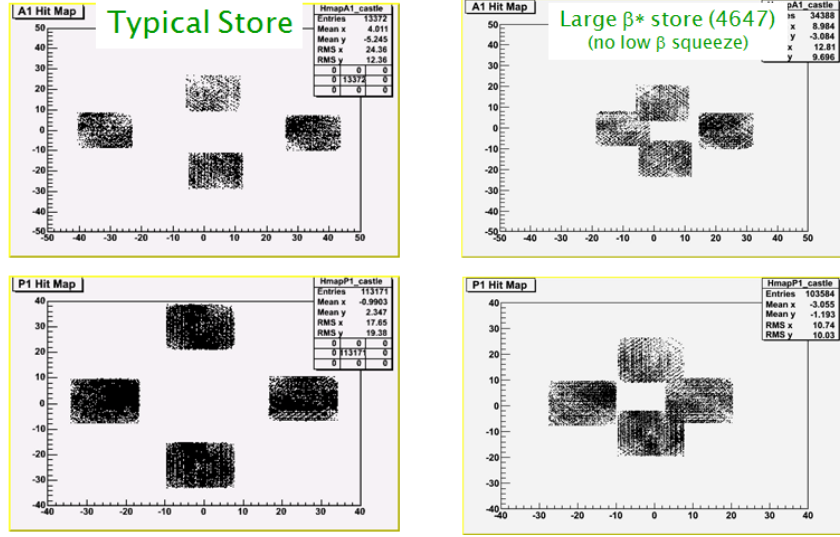


Figure 4.1. Hitmaps showing position of the forward detectors on the proton side and the anti-proton side during the high  $\beta^*$  store compared to the detector position during a normal store.

closer to the beam during this store the transverse momentum ( $|t|$ ) acceptance extends to much lower values of  $|t|$ . Figure 4.2 shows the anticipated  $|t|$  range accessible during the high  $\beta^*$  run, extracted from a proposal with the minimum  $|t|$  determined by the pot position and the maximum by the integrated luminosity.

#### 4.1.2 Data sets

During the high  $\beta^*$  run a total of 20 million events were recorded using a special trigger list for elastic and diffractive physics. Table 4.1 shows the run numbers and the number of events corresponding to each run. The data is comprised of two different sets of detector positions with respect to the beam. Table 4.2 shows the detector positions for data set 1 which corresponds to run numbers 215417 to run number 215430 and data set 2 from run numbers 215433 to run number 215449 with respect to the beam. The values of the detector position correspond to the measured position

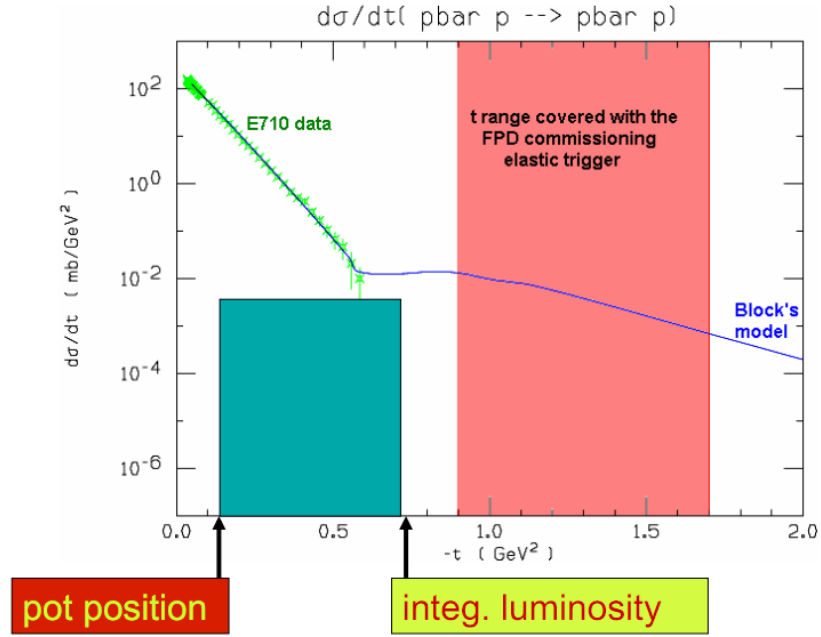


Figure 4.2. Comparison of the expected  $|t|$  acceptance during the accelerator run at  $\beta^*=1.6$  m with that of standard operation.

during data taking. These values were later corrected after the alignment of the detector.

#### 4.1.3 Triggers used

The triggers used to record the events were based on patterns of scintillating fibers. A fiber was “ON” if its ADC value was above the Analog Front End board (SIFT) threshold. Simple fiber segments were defined using the primed and un-primed planes of the fibers. A “fine fiber segment” is defined as  $1/3$  of a scintillating fiber width and a “wide fiber segment” is defined as  $4/3$  of a scintillating fiber width. The triggers used the wide fiber segments.

The single diffraction data is recorded using two different types of triggers, one for the proton side and the other for the anti-proton side. The proton side

Table 4.1. Total number of events triggered during the high  $\beta^*$  run broken down into run numbers

Run Numbers	Events
215417	740705
215418	508464
215421	827303
215424	1600633
215425	1220636
215429	4147836
215430	435472
215433	140072
215434	787005
215436	1359433
215440	1012787
215443	1114845
215445	789949
215447	1769842
216448	1591610
215449	1530883
TOTAL	19891750

trigger “SD\_PRO” includes a PU, PD, PO or PI hits while the anti-proton side trigger “SD\_PBAR” includes A-side hits. The “SD\_PRO” trigger is defined as

$$\{(P1U \cdot P2U) \vee (P1D \cdot P2D) \vee (P1I \cdot P2I) \vee (P1O \cdot P2O)\}_{Hit} \cdot \{ALMNorth[v]\} \quad (4.1)$$

where “ALMNorth[v]” is a veto on hits in the north luminosity monitor. Similarly, the “SD\_PBAR” trigger can be written as

$$\{(A1U \cdot A2U) \vee (A1D \cdot A2D) \vee (A1I \cdot A2I) \vee (A1O \cdot A2O)\}_{Hit} \cdot \{ALMSouth[v]\} \quad (4.2)$$

Table 4.2. Detector positions for data set 1 which corresponds to run numbers 215417 to run number 215430 and data set 2 from run numbers 215433 to run number 215449 with respect to the beam

Detector	Position(mm) Set 1	Position(mm) Set 2	$\Delta_{Position}$ (mm)
A1U	5.75	5.41	0.34
A1D	5.44	4.08	1.36
A1I	3.83	3.83	0.00
A1O	14.74	12.21	2.53
A2U	4.53	4.24	0.29
A2D	5.04	5.04	0.00
A2I	4.02	4.37	-0.35
A2O	12.52	10.27	2.25
P1U	9.17	7.96	1.21
P1D	5.7	3.88	1.82
P1I	11.00	9.22	1.78
P1O	8.11	3.83	4.28
P2U	8.17	7.11	1.06
P2D	4.84	4.35	0.49
P2I	11.72	10.2	1.52
P2O	4.39	4.39	0.00

At each detector level a “TIGHT” hit is required. The “TIGHT” hit condition (T) requires that there is exactly one validated wide segment hit in U and V plane of the detector. The validated condition requires that the X segment intersecting the U and V segments was also “ON”. There are two possible hit conditions that are allowed “MEDIUM” and “LOOSE”. The MEDIUM (M) condition allows up to three validated hits and the LOOSE (L) condition requires only 2 out of 3 planes to be ON. The MEDIUM and LOOSE hit conditions are not used in the single diffraction triggers, but they are used in the elastic and double-pomeron triggers. Table 4.3 shows the detailed description of the configuration of the single diffractive triggers corresponding to each runs and their prescale factors.

Table 4.3. Single diffractive trigger configurations per run of the store 4647. Here T=TIGHT and X=no condition. The order of trigger conditions in the detectors are P1, P2, A1 and A2. The number by which each condition is divided by corresponds to the prescale for that trigger. Here SD\_PRO = XXTT and SD\_PBAR = TTXX

Run	Events $\times 10^6$	SD_PRO Trigger	SD_PBAR Trigger
215417-8	1.2	TTXX/15	XXTT/15
215421	0.8	TTXX/20	XXTT/15
215424-30	7.4	TTXX/20	XXTT/15
215433-36	2.2	TTXX/50	XXTT/30
215440	1.0	TTXX/50	XXTT/30
215443	1.1	TTXX/50	XXTT/30
215445-47	3.7	TTXX/70	XXTT/40
215448-49	3.1	TTXX/70	XXTT/40

## 4.2 Data Reconstruction

The data from the runs 215417 to 215449 were unpacked from the “raw” format to DØ thumbnails using the “d0\_reco” version p17.09.07. This version of the d0\_reco unpacks the forward detector data (ADC data) and the timing information (TDC data) of the FPD system. The main goals of the reconstruction process were the following

- Extract the FPD fiber (ADC) information.
- Extract the FPD timing (TDC) information.
- Apply the new detector positions to the reconstruction obtained during the alignment process [1]
- Add new branches to the “caftrees” like the “Fpd branch” for the fiber information and “Tdc branch” for the timing information.
- Reconstruct the forward tracks using the program called “Fpd Reco” [53, 54, 55]
- Use the SIFT fibers for track reconstruction, these are the fibers which are above the SIFT threshold and fire the trigger



- Extract the values of the kinematic variables.
- Lower the momentum cut for the central tracks in  $D\bar{O}$  reco so that low momentum tracks with  $p_T > 150$  MeV are available.

#### 4.2.1 Alignment of detectors

The alignment converts the hit position measured in the detector coordinates to the coordinate systems with respect to the beam. The alignment was done for the elastic analysis using the elastic events [1]. The method used to calculate the detector position with respect to the beam relies on the fact that one can select the elastic events without knowing the exact position of the detectors. Since the selected events are elastic and the forward detectors on both sides of the interaction point are at the same longitudinal (z) distances from the intersection point (IP), the hits in the proton and anti-proton detectors are expected to be collinear. Figure 4.3 from the elastic note [1] shows the hits from the opposite side using the survey data in Table 4.2. It is clear from the plots that the hits in the detectors are not consistent with the elastic requirement as the hits do not lie in a straight line. Figure 4.4 shows the distribution of difference in hit coordinates ( $\Delta x$  and  $\Delta y$ ) of the first and the second detectors. This is a more quantitative approach to show the misalignment of the detectors. In these plots  $\Delta x = x_2 - R \times x_1$  and  $\Delta y = y_2 - R \times y_1$ , these distributions should be Gaussian with mean about zero for elastic events.

To fix the alignment problem of the detectors a data driven alignment method was developed. This method relies on the fact that during this store the detectors were much closer to one another. The horizontal and the vertical detectors overlap at the edges as shown in Fig. 4.1. There is a sample of tracks which pass through both the detectors at the same time. This sample can be used to obtain the relative position of the detectors with respect to each other. By choosing a set of elastic

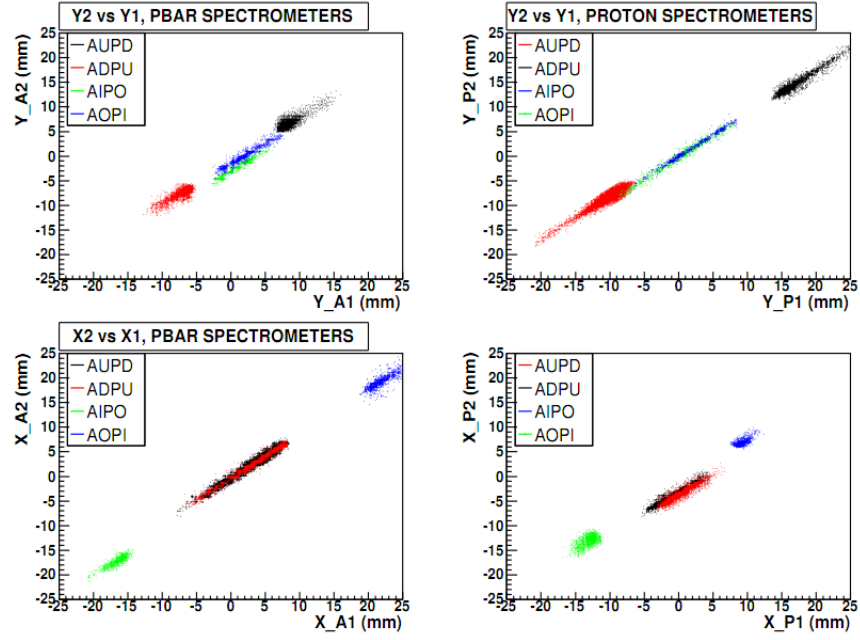


Figure 4.3. Comparison of elastic event coordinates between spectrometers with detectors at the same locations in the Tevatron.

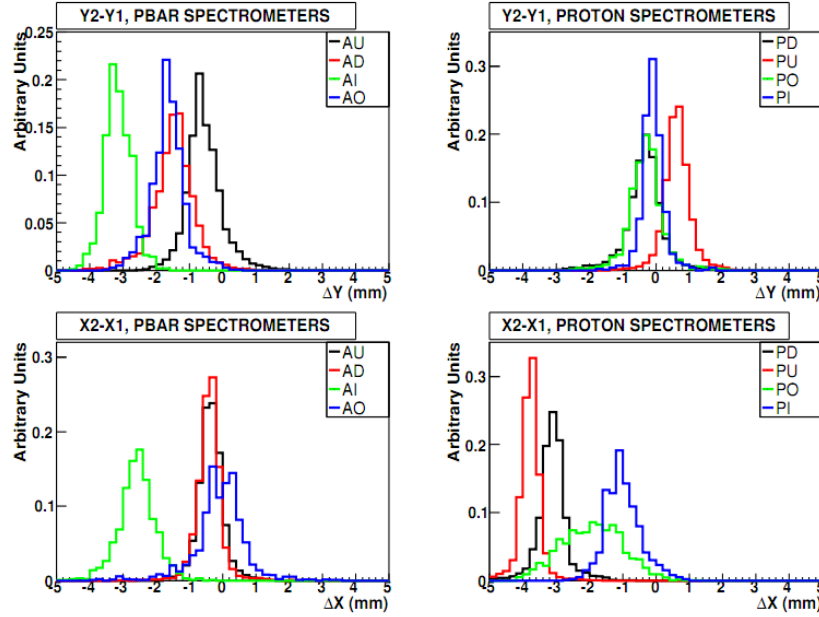


Figure 4.4. The distribution of  $\Delta x$  and  $\Delta y$  for the detectors in the elastic events using the survey data. The distributions are normalized to unit area for comparison of their shapes.

events it is possible to find out the position of all the detectors with respect to each other as well as with respect to the beam. A detailed description of the alignment procedure is given in elastic analysis note [1].

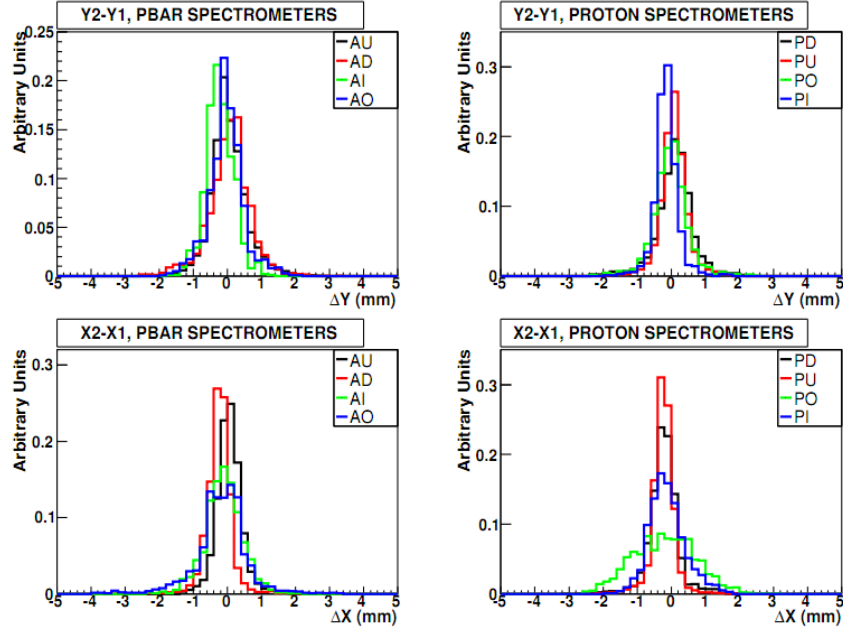


Figure 4.5. The distribution of  $\Delta x$  and  $\Delta y$  for the detectors in the elastic events after applying the alignment.

Figure 4.5 shows the distribution of  $\Delta x$  and  $\Delta y$  after the alignment is applied. The distribution shows that the relative position of the detectors has been determined correctly. By using the fact that the events are elastic the position of the detectors with respect to the beams is obtained. Tables 4.4 and 4.5 shows the alignment parameters of the detectors in data set 1 and data set 2 with respect to the beam. In these tables  $y_c$  and  $x_c$  gives the values of the detector corners with respect to the castle centers. The columns  $y_o$  and  $x_o$  give the offset of the beam from the castle center, columns  $y_b$  and  $x_b$  gives the  $x$  and  $y$  position of the beam with respect to the detector corner.

Table 4.4. Positions of the detectors for data set 1 (Runs 215417-215430), columns 2 and 3 are the positions before the alignment, columns 4 and 5 are the offsets of the castle center with the beam and columns 6 and 7 are the pot positions with respect to the beam after alignment.

Detector	$y_c$ (mm)	$x_c$ (mm)	$y_o$ (mm)	$x_o$ (mm)	$y_b$ (mm)	$x_b$ (mm)
A1U	4.65	8.635	0.97	4.46	3.68	13.10
A1D	5.39	8.695	0.97	4.46	6.36	4.24
A1I	3.05	8.695	0.97	4.46	7.51	9.67
A1O	14.53	8.250	0.97	4.46	10.07	7.28
A2U	1.29	8.395	-2.16	3.66	3.45	12.06
A2D	6.39	8.695	-2.16	3.66	4.23	5.04
A2I	1.03	8.695	-2.16	3.66	4.69	6.54
A2O	12.05	7.000	-2.16	3.66	8.39	9.16
P1U	8.47	9.720	2.10	-0.76	6.37	10.48
P1D	4.78	8.695	2.10	-0.76	6.88	7.94
P1I	8.50	8.995	2.10	-0.76	7.74	6.90
P1O	9.51	8.695	2.10	-0.76	10.27	10.8
P2U	8.06	8.900	1.90	-4.39	6.16	13.29
P2D	4.04	8.695	1.90	-4.39	5.94	4.31
P2I	11.42	9.300	1.90	-4.39	7.03	7.40
P2O	2.91	8.695	1.90	-4.39	7.30	10.60

#### 4.2.2 Reconstruction program

To reconstruct the forward proton tracks, the generalized DØ forward proton reconstruction program is used. This program is called “d0fpd\_track” [56]. The code is based on transport equations [55] of tevatron lattice for high beta low luminosity field strength. There is a database interface of the reconstruction program called “fpd\_db\_client” [57] which is used to retrieve all the field strengths and the detector geometries. The detector positions with respect to the beam are a input from the user. The detector position values obtained from the alignment procedure described in the previous section are used. There is also a propagation code in the reconstruction

Table 4.5. Positions of the detectors for data set 2 (Runs 215433-215449) , columns 2 and 3 are the positions before the alignment, columns 4 and 5 are the offsets of the castle center with the beam and columns 6 and 7 are the pot positions with respect to the beam after alignment.

Detector	$y_c$ (mm)	$x_c$ (mm)	$y_o$ (mm)	$x_o$ (mm)	$y_b$ (mm)	$x_b$ (mm)
A1U	4.31	8.635	0.97	4.46	3.34	13.16
A1D	4.03	8.695	0.97	4.46	5.00	4.24
A1I	3.05	8.695	0.97	4.46	7.51	9.67
A1O	12.00	8.25	0.97	4.46	7.54	7.28
A2U	1.00	8.395	-2.16	3.66	3.16	12.06
A2D	6.39	8.695	-2.16	3.66	4.23	5.04
A2I	1.38	8.695	-2.16	3.66	5.04	6.54
A2O	9.80	7.000	-2.16	3.66	6.14	9.16
P1U	7.26	9.720	2.10	-0.76	5.16	10.48
P1D	2.96	8.695	2.10	-0.76	5.06	7.94
P1I	6.72	8.995	2.10	-0.76	5.96	6.90
P1O	5.23	8.695	2.10	-0.76	5.99	10.8
P2U	7.00	8.900	1.90	-4.39	5.10	13.29
P2D	3.55	8.695	1.90	-4.39	5.45	4.31
P2I	9.90	9.300	1.90	-4.39	5.51	7.40
P2O	2.91	8.695	1.90	-4.39	7.30	10.60

program. This code is used to check if a particle is in the active area of the detector. This is useful for FPD detector simulation. The single diffractive Monte Carlo along with the detector simulation is used to study detector acceptances.

#### 4.2.2.1 Hit finding

The hit reconstruction program used in this analysis is designed to analyze multi-hit events. In the first step the program reads how many channels (fibers) are tuned on (the ADC counts of the fibers are above the SIFT threshold). In the next step the program defines segments for each plane from the ON fibers. This process

is called clustering. The fibers are grouped into clusters defined as clusters of size 1 through 5 as shown in Fig. 4.6. The size of the cluster depends on how many neighboring fibers are hit. A cluster size of one is the simplest cluster. The clustering function also finds the clusters in such a way that the number of fibers in each segment is minimum.

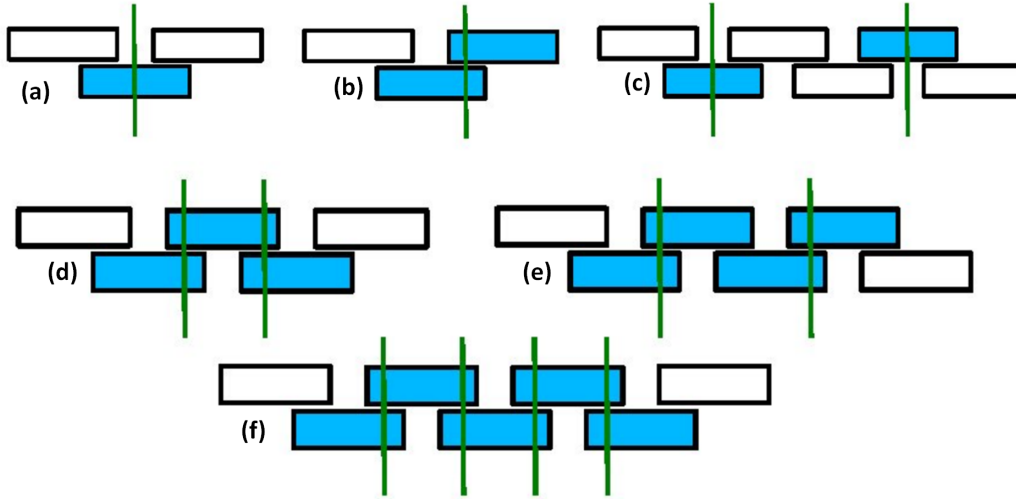


Figure 4.6. Definition of cluster of (a)size one, (b)size two, (c)two clusters of size two characterizing a multi-hit event, (d)cluster of size three, (e)size four and (f)size five are shown.

#### 4.2.2.2 Reconstruction of tracks

After all the clusters are determined in a detector, these clusters are combined in two plane combinations to find the possible hit positions. At this point only the planes which have fiber multiplicity less than 5 ( $N_{fiber} < 5$ ) are considered for track reconstruction. This fiber multiplicity cut gets rid of multi-hit and spray type of events as shown in the elastic analysis.

The reconstruction program is based on an iterative method. The basic idea of the iteration method is to start the process with an initial pair of values of  $\xi = 0$  and  $\xi_{step}$ , where  $\xi_{step}$  is a parameter denoting the step size. Using the linear approximation between the  $x$  and  $y$  coordinates it calculates a correction to  $\xi$  in the first step. In the second step there is another correction to the value of  $\xi$  obtained by calculating new values of the interaction point. The method stops after two steps. For this analysis a  $\xi_{step} = 0.0001$  have been used. There is also a minimum value of interaction point position change in step 2, called  $\Delta IP_{cut}$ . The value of  $\Delta IP_{cut} = 0.001$  mm, if the position of the interaction points are too close to one another, the reconstructed  $\xi$  is not reliable [53]. The reconstruction step can fail in two cases: 1) step 2 can fail the minimum  $\Delta IP_{cut}$  cut 2) the particle may not propagate to the IP and hit the beam pipe. If any of the steps fails then the whole process is started again with new initial values of  $\xi$  such that  $\xi_{new} = \xi + \xi_{step}$ . The convergence of the iteration method is defined as

$$\left| 1 - \frac{\xi_{reco}}{\xi_{real}} \right| \quad (4.3)$$

where the convergence of the reconstruction is only a function of  $\xi_{step}$

#### 4.2.2.3 Timing information

Each detector in the FPD system contains a trigger scintillator. This is used to observe the time at which the particle pass through the detector. To get the trigger scintillator timing information into the data files, the “raw” files were unpacked along with the timing information. A new branch in the “**caftree**” called “TDC” was added. The “TDC” branch contains all the timing information for all the eight trigger scintillators. Figure 4.7 shows the timing of the FPD system for a proton halo

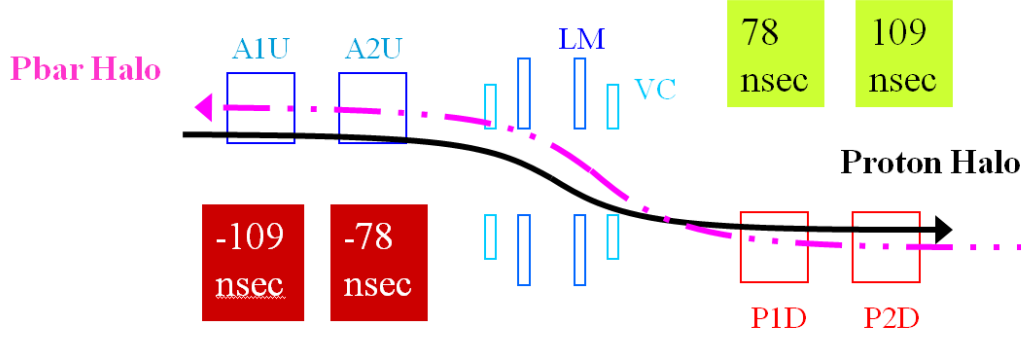


Figure 4.7. Schematic diagram to show the timing of proton track using the timing detectors.

track. The two important variables in the “TDC” branch are the “hit bit” and “halo bit”.

- The hit bit is set to **TRUE** if a hit is detected in the in-time window. The in-time bit is defined using a window of 5 ns around 78 ns for det1 and 109 ns for det2.
- The halo bit is set to **TRUE** if a hit is detected in the early-time window.

Figure 4.8 shows the distribution of halo bits in a run. It can be seen that the hit bits corresponding to the proton halo have about 10 times higher statistics than those halo bits corresponding to the anti-proton halo. Since we also know that the corresponding detectors on the proton and anti-proton sides have similar acceptances this distribution is expected as the proton intensity is  $\sim 10$  times higher than the anti-proton intensity. We also expect more halo in horizontal plane due to momentum dispersion

#### 4.2.2.4 Low momentum tracks

One of the objectives of the reconstruction is to study the double pomeron exchange [58] process and associated central resonances [59]. To study the mass resonances, I implemented a new reconstruction cut to lower the  $p_T$  threshold from



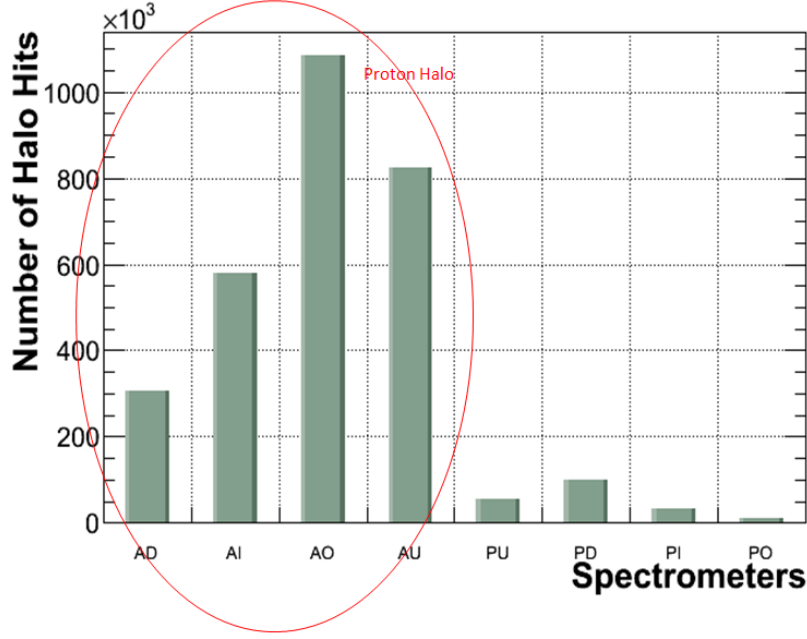


Figure 4.8. Distribution of halo bits in a run using the trigger scintillator timing information. The proton halo rates are much higher than the anti-proton halo rates.

the  $D\bar{O}$  standard value of 500 MeV to 150 MeV. Figure 4.9 shows the  $p_T$  distribution of the leading tracks showing that tracks below  $p_T$  of 500 MeV are now reconstructed.

For the purpose of cross check, the central track multiplicity distribution of three different types of halo events are compared. In principle halo events should not have any central tracks except for the events that consist of an overlapped minimum bias event with a track event. Based on this fact three different types of halo events were chosen, events with a proton track tagged as halo, events with a anti-proton tracks tagged as halo, and events with both proton and anti-proton tracks tagged as halo events. A detailed description of selection of different types of halo events is given below:

- **p side halo:** Choose events with `SD_PRO` trigger and demand that there is only one halo track on the  $p$ -side spectrometer (track is a halo track when the halo bits on the diagonally opposite A-side spectrometers are ON).

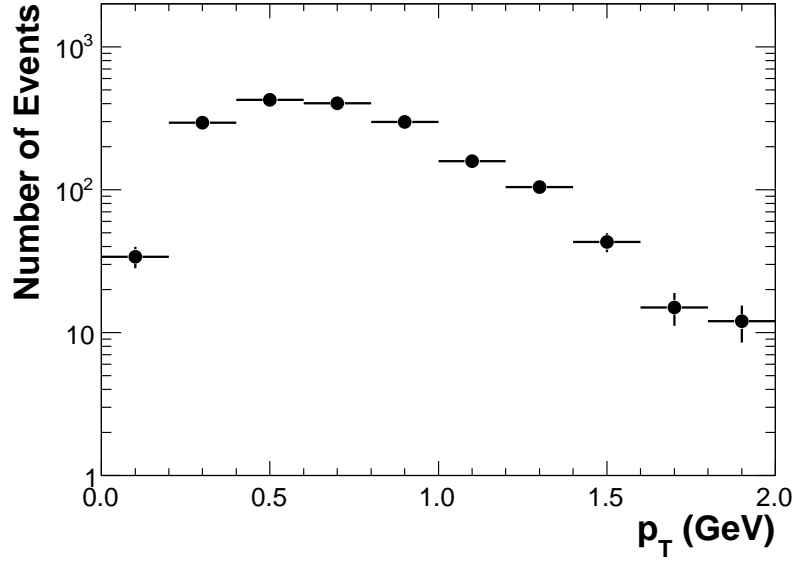


Figure 4.9. Transverse momentum distribution,  $p_T$  of the leading central tracks after lowering the threshold from 500 MeV to 150 MeV.

- **$\bar{p}$  side halo:** Choose events with SD\_PBAR trigger and demand that there is only one halo track on the  $\bar{p}$ -side spectrometer (track is a halo track when the halo bits on the diagonally opposite P-side spectrometers are ON).
- **$p$  and  $\bar{p}$  halo:** Choose events with DPOM trigger and demand that there is only one halo track on the  $\bar{p}$ -side spectrometer and  $p$ -side spectrometer each.

Figure 4.10 shows the track multiplicity distribution of the three different kind of halo events. It can be seen that the distribution are in agreement with each other. Table 4.6 shows the fraction of zero track events. Since the events are halo events the fraction of zero track events from 97% to 99% is consistent. The small number of events in which there are central tracks could be due to fake tracks or overlap with minimum bias events.

To estimate the fake track rate, empty events were chosen. This was done by selecting events with `zero_bias_NCU` trigger and tick number not equal to 7 (the  $p$

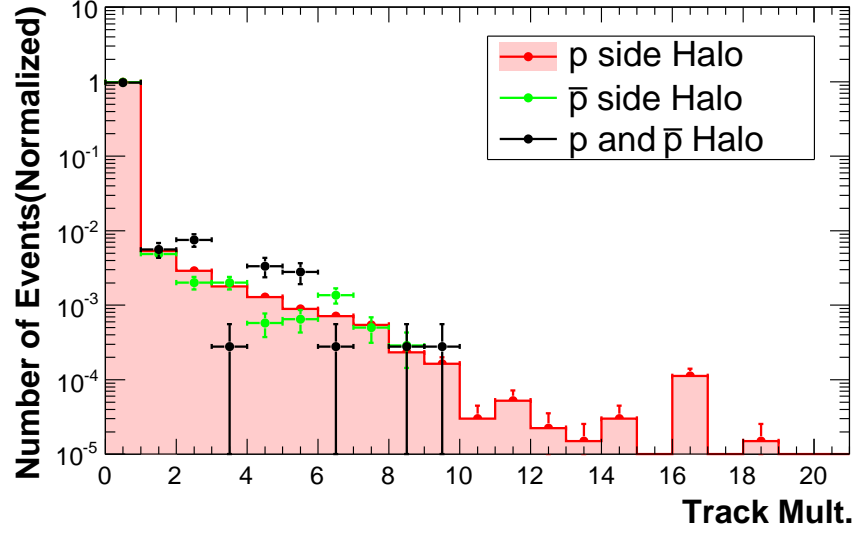


Figure 4.10. Track multiplicity distribution for three different kinds of halo events.

Table 4.6. The fraction of zero track events and the mean number of tracks for different types of halo events

Halo type	No. of Events	Frac. zero track	Mean no. Tracks
Double halo	3581	0.979	0.058
$p$ Halo	133698	0.985	0.042
$\bar{p}$ Halo	13922	0.987	0.039

and  $\bar{p}$  bunch only collide in tick number 7). The central tracks in these empty events are expected to be fake tracks. Table 4.7 shows that the fake track rate for the low momentum track cut is very low. It also shows that the probability of accidentally firing the Luminosity monitors (LM noise) is also very low.

### 4.3 Validation of reconstruction

The validation of the FPD reconstruction was done by direct comparison with elastic events from the elastic analysis [1] The two steps in the validating the re-

Table 4.7. Number of different types of events which are subset of empty events (zero bias with wrong tick) to determine the noise levels

Total events <code>zero_bias_NCU</code> trigger	429635
Events with no central tracks	428680
Fraction of zero track events	0.998
<code>LMSouth</code> hits	18
<code>LMNorth</code> hits	29
<code>LMSouth AND LMNorth</code> hits	4

construction program by using the hits from the elastic reconstruction and the FPD reconstruction: 1) validation of track 2) validation of hit finding for both the programs.

#### 4.3.1 Validation of track reconstruction

In order to check the reconstruction program, elastic events were chosen from the elastic analysis. The hits from the elastic analysis were provided as inputs to the FPD reconstruction program. It is important to understand the difference between the elastic reconstruction and FPD reconstruction, since in the case of elastic reconstruction  $\xi$  is set to zero. In the case of FPD reconstruction the values  $\xi$  and  $|t|$  are calculated iteratively from the hit coordinates. In this section the events from elastic configuration in AU-PD spectrometers have been considered.

Figure 4.11 shows the difference in the reconstructed  $|t|$  value in GeV for the AU and PD spectrometers for the elastic and FPD reconstruction programs. It can be seen that the reconstruction programs are in agreement.

Figure 4.12 shows the difference in the the reconstructed  $|t|$  for the proton and the anti-proton. In the elastic events it is expected that they have same  $|t|$  values. The shaded region in the plot shows the distribution of  $\Delta|t|(p - \bar{p})$  for the elastic reconstruction and the red points shows the the difference for the FPD reconstruc-

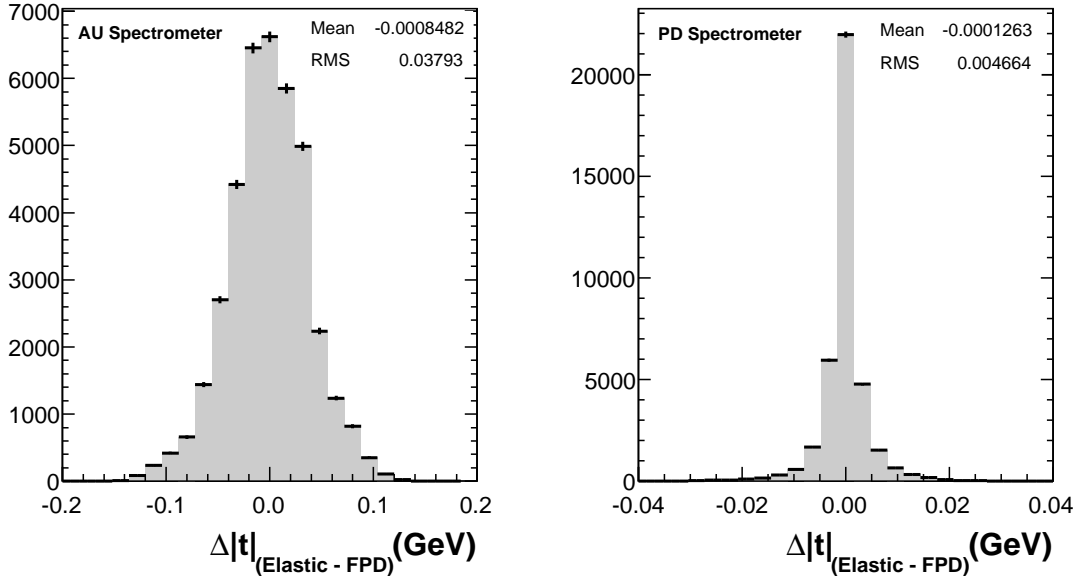


Figure 4.11. Difference in the values of  $|t|$  reconstruction for the elastic and FPD reconstruction. The plot on the left show the  $\Delta|t|$  for AU spectrometer and the plot on right shows  $\Delta|t|$  for PD spectrometer for the same elastic events.

tion, it can be seen that both reconstructions are in agreement with each other. The resolution of the elastic reconstruction is slightly smaller than that of the FPD reconstruction since  $\xi$  is constrained to zero in elastic reconstruction.

Figure 4.13 is a profile plot showing the difference in the elastic and FPD reconstruction as a function of  $|t|$ . It can be seen that there is no bias in the reconstruction. It can be seen that the resolution of the PD spectrometer is higher than that of the AU spectrometer. This feature is also seen in Fig. 4.11.

Figure 4.14 shows the difference between the proton and the anti-proton  $|t|$ . In this figure it can be seen that the FPD reconstruction has full agreement with the elastic reconstruction as well. Since this is a profile plot it can be seen that the resolution of the  $|t|$  reconstruction becomes worst with the increase in  $|t|$  value, this

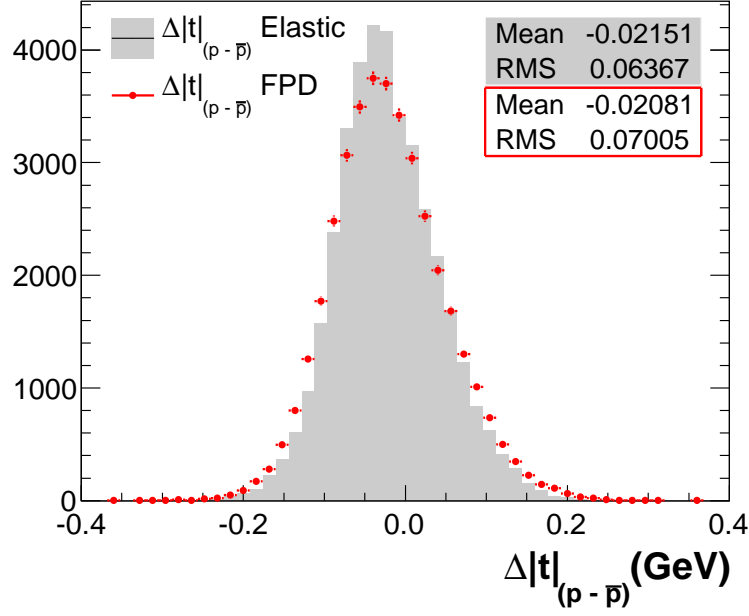


Figure 4.12.  $\Delta|t|_{p-\bar{p}}$  in the forward track  $|t|$  between the proton and the anti-proton for the elastic events. The shaded region shows the difference for the elastic reconstruction, the red points shows the FPD reconstruction.

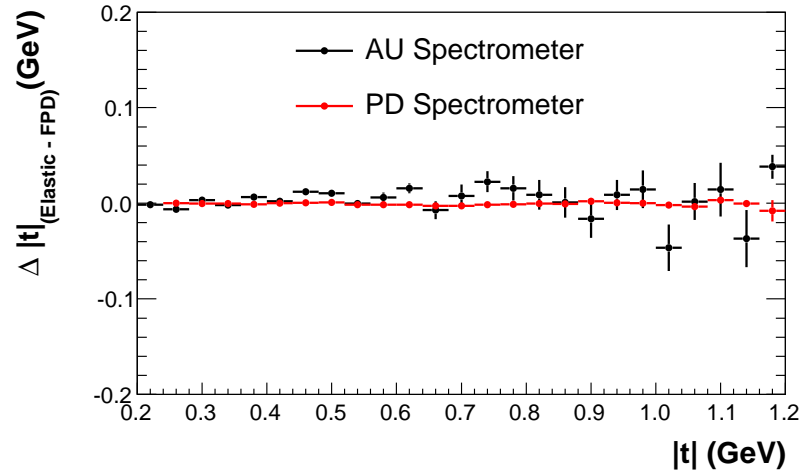


Figure 4.13. Profile showing the difference between the elastic and FPD reconstruction as a function of  $|t|$  for the AU and PD spectrometers.

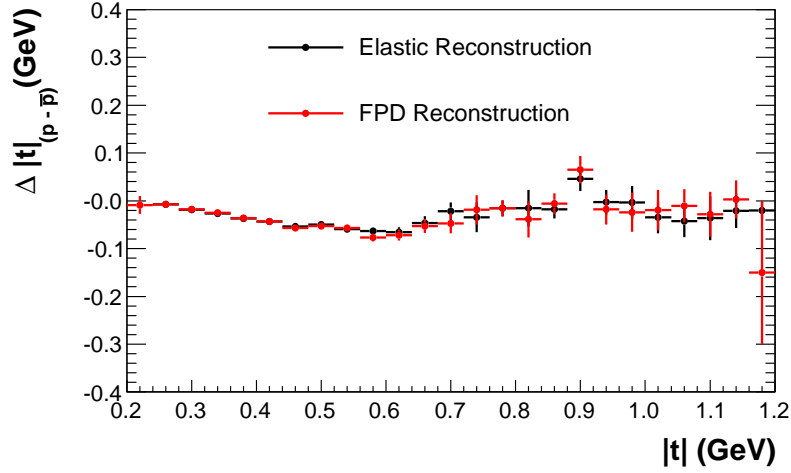


Figure 4.14. Profile plot showing the difference between the  $p$  side  $|t|$  and  $\bar{p}$  side  $|t|$  for the same elastic events obtained from the elastic and FPD reconstruction.

is a expected feature. Although there is some structure to the figure, the absolute deviation from  $\Delta|t| = 0$  is small.

#### 4.3.2 Validation of hit finding

The next step in the validation process is to evaluate the differences in the hit finding algorithms between the elastic and FPD reconstruction programs. For this purpose the events were reconstructed with both algorithms. In order to have agreement with the elastic analysis event selection, correlation cuts for the 1<sup>st</sup> and 2<sup>nd</sup> detector are implemented by using the events from the elastic analysis for all four different spectrometers. Figure 4.15 shows the elastic band cuts for the AU and PD spectrometer configuration. Figure 4.16 shows the elastic band cuts for the AD and PU configurations. Table 4.8 shows the equations of the upper and lower line cuts for each spectrometer.

After applying the band cuts obtained from elastic events, the FPD reconstruction program is run on the same events. The hit coordinates from the FPD

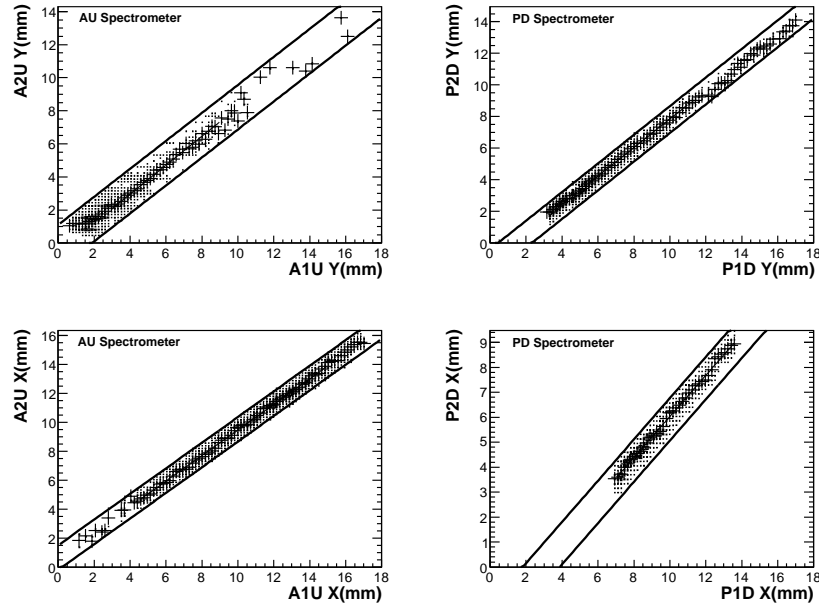


Figure 4.15. AUPD elastic band cuts evaluated using the elastic data points.

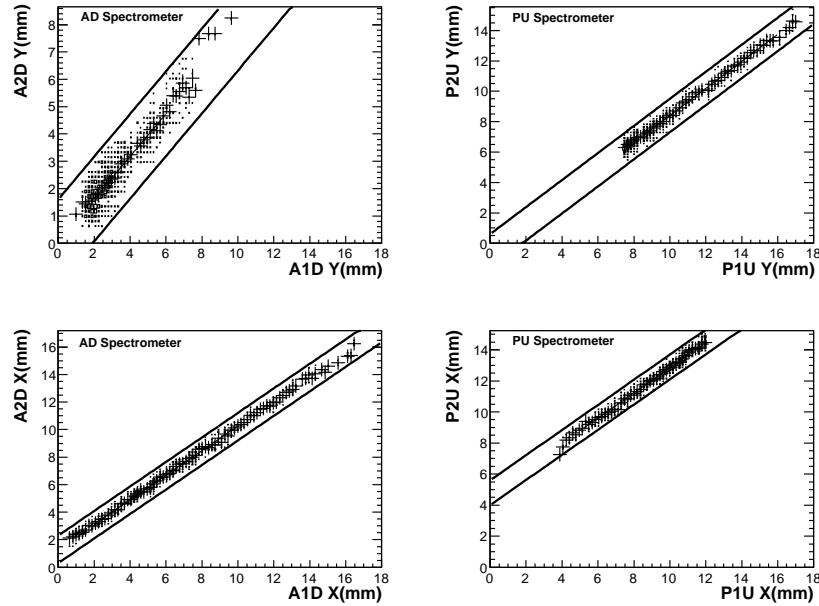


Figure 4.16. ADPU band cuts evaluated using the elastic data points.



Table 4.8. Elastic band cut equations

Spec.	x Lower cut	x Upper cut	y Lower cut	y Upper cut
AU	$-0.2 + 0.887.x$	$1.5 + 0.887.x$	$-1.6 + 0.847.x$	$1.1 + 0.847.x$
AD	$0.3 + 0.891.x$	$2.3 + 0.891.x$	$-1.5 + 0.782.x$	$1.6 + 0.782.x$
PU	$4.0 + 0.809.x$	$5.6 + 0.809.x$	$-1.6 + 0.890.x$	$0.6 + 0.890.x$
PD	$-3.2 + 0.826.x$	$-1.5 + 0.826.x$	$-2.1 + 0.905.x$	$-0.4 + 0.905.x$

reconstruction are compared with the hit coordinates from the elastic analysis. Figure 4.17 shows the distribution of the difference between the  $x$  coordinates of the hits from the elastic and FPD reconstruction programs for the AU and PD spectrometers. Figure 4.19 shows the difference in the  $x$  coordinate of the hits for the AD and PU spectrometers. It can be seen in the figures that there are some peaks other than the central distribution, this is because of the difference in the hit finding algorithms used in the elastic and FPD reconstruction program. Figure 4.6 illustrates the FPD hit finding algorithm, it uses five different types of clusters whereas the elastic reconstruction uses only three types of cluster, from type 1 to type 3. So in the elastic reconstruction program a type 5 hit would appear to be two hits and the reconstruction would pick the hit with higher ADC count, while in the FPD reconstruction this would be only one hit. Each fine segment is approximately  $270 \mu m$  wide and there is a difference of up to two wide segment between the two programs so the shift in the hit position would be approximately  $2/\sqrt{(2)} \approx 400 \mu m$ . Figures 4.18 and 4.20 shows the comparison of the  $y$  coordinates, which are in agreement with each other.

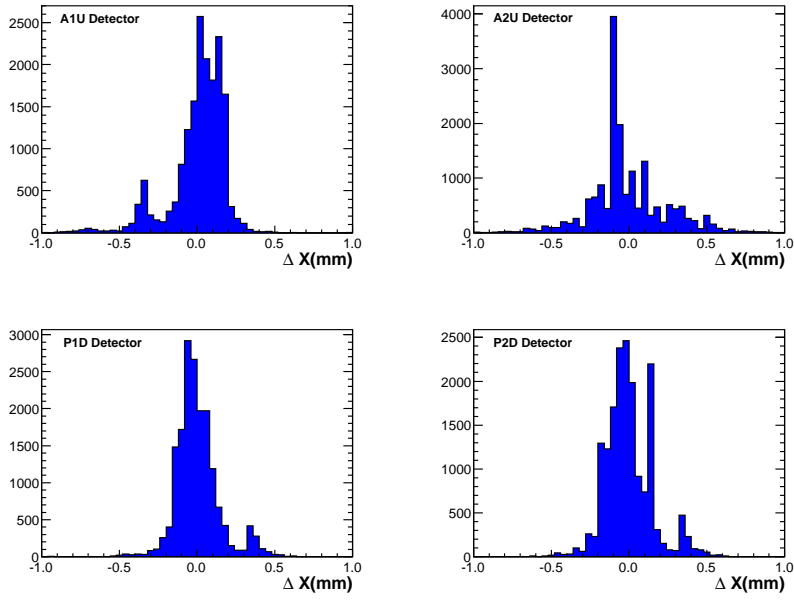


Figure 4.17. Difference between the hit coordinates ( $x$ ) for AU and PD detectors.

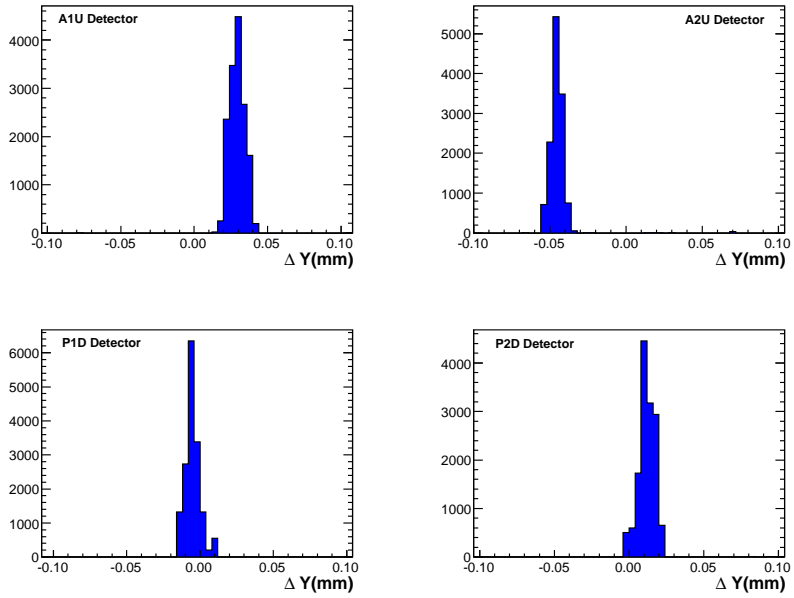


Figure 4.18. Difference between the hit coordinates ( $y$ ) for AU and PD detectors.

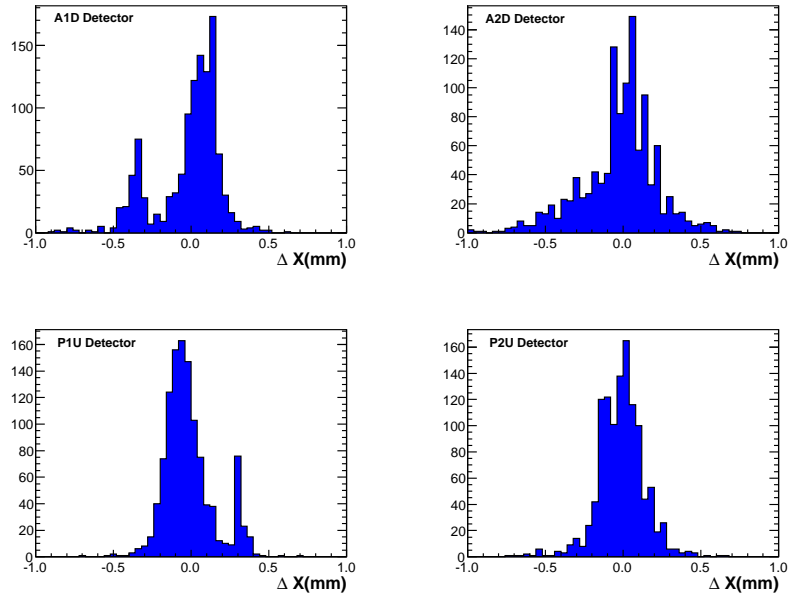


Figure 4.19. Difference between the hit coordinates ( $x$ ) for AD and PU detectors.

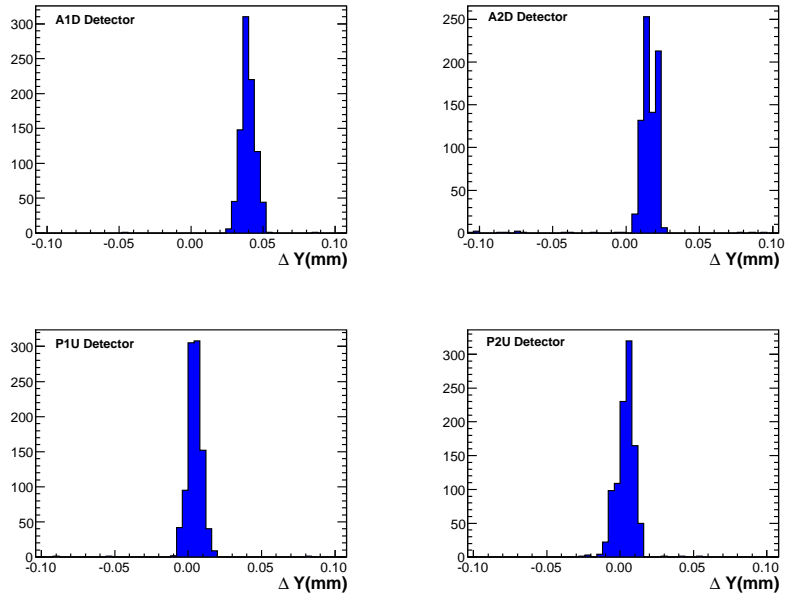


Figure 4.20. Difference between the hit coordinates ( $y$ ) for AD and PU detectors.

#### 4.4 Single diffractive event selection

The different steps for selection of single diffractive events is listed below and the details of these cuts are given in the following sections

- Select event with `SD_PRO` or `SD_PBAR` triggers.
- Demand that there is a valid forward track in the FPD detector.
- Select high mass single diffractive events demanding hits in the Luminosity monitors.
- Choose events which have tracks inside the good fiducial region of the forward detectors.
- Reject halo tracks.

##### 4.4.1 Trigger selection

The single diffractive data was recorded with two special triggers, `SD_PRO` which is the single diffractive trigger on the proton side and `SD_PBAR` which is the single diffractive trigger on the anti-proton side. As mentioned earlier `SD_PRO` trigger is defined as the OR of triggers coming from the four spectrometers on the proton side (PU, PD, PI and PO) also require not hits in the luminosity monitor on the south side, while `SD_PBAR` trigger is similar but requires anti-protons. At the spectrometer level there is a requirement for a “TIGHT” condition on both of the detectors. The TIGHT condition (T) is a requirement made at the hit level in the detectors. It demands that there is exactly one validated wide segment hit in the U and V planes. Validated hit means that the X plane which has fiber intersecting the U and V planes are also hit.

#### 4.4.2 High and low mass single diffraction

The single diffractive events are classified into two different types of single diffractive processes; 1) High mass single diffractive events 2) Low mass single diffractive events.

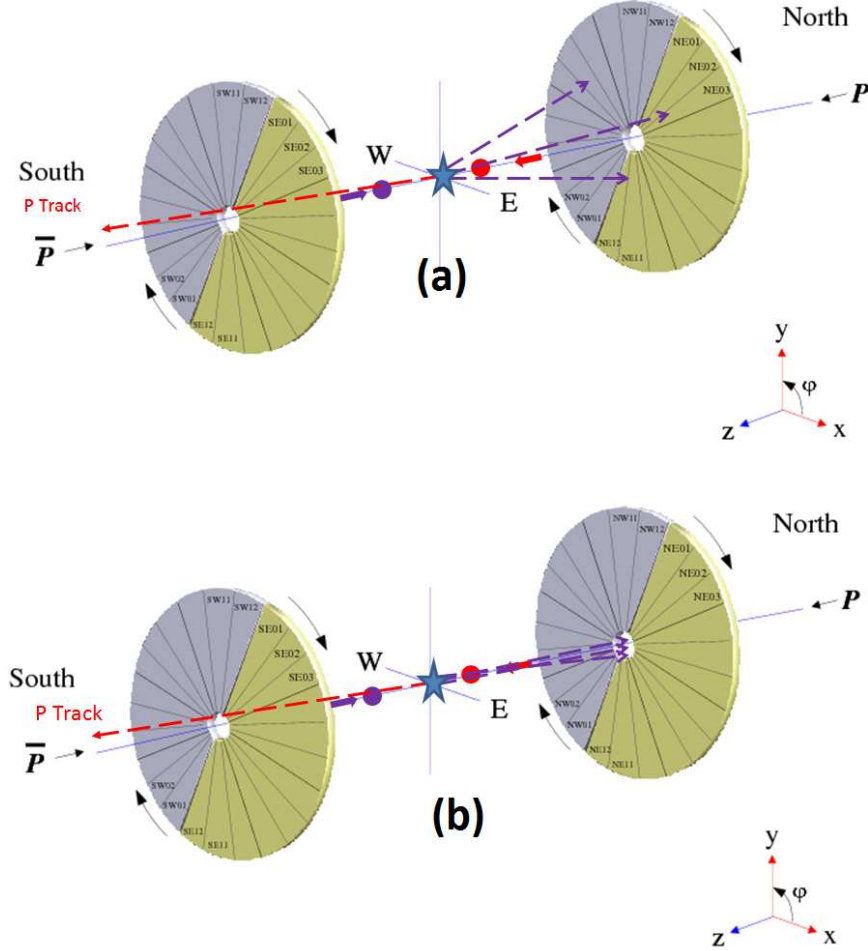


Figure 4.21. (a) High mass single diffractive event in which the luminosity monitor on the opposite side is hit. (b) Low mass single diffractive event in which the diffractive products are carried along the beam pipe and there are no hits in the luminosity monitor.

Figure 4.21(b) shows a proton side low mass single diffractive event: there is a forward track on the proton side. The diffractive system on the anti-proton side is

low mass and the particles remain in the beam pipe without hitting the luminosity monitor on the other side. These kinds of events have large halo contamination. Figure 4.21(a) shows a proton side high mass single diffractive events: there is one forward proton track in the proton side. The diffractive system on the anti-proton side hits the luminosity monitor. We can select these kinds of events by demanding hits in the opposite side luminosity monitor on the other side. High mass single diffractive events have lower halo contamination than the low mass single diffractive events. Still there is some contamination from halo and zero arm single diffractive events. Since there is a hit requirement on the luminosity monitor on the other side it imposes an effective mass cut of  $M_X > 11.6$  GeV on the high mass single diffractive events. In this analysis we are going to use the high mass single diffractive events.

#### 4.4.3 Detector correlation cuts

The detector correlation cuts are evaluated using a standalone Monte Carlo program. This program uses the Tevatron lattice to simulate the propagation of the final state protons and anti-protons to the forward detectors. The Monte Carlo includes 16 quadrupole detectors and takes into account the smearing effects from beam divergence and detector resolution. This is useful in evaluating the single diffractive detector correlation cuts and the geometrical acceptance of the detectors.

##### 4.4.3.1 Single diffractive Monte Carlo

To generate the events for the simulation POMWIG parametrization function has been used in such a way that for these events  $M_X > 11.6$  GeV. The lattice parameters and the detector position are used as inputs for the program. The detector position determine the minimum values of  $|t|$  that are accepted by the different spectrometers while the beam pipe aperture limits the maximum  $|t|$

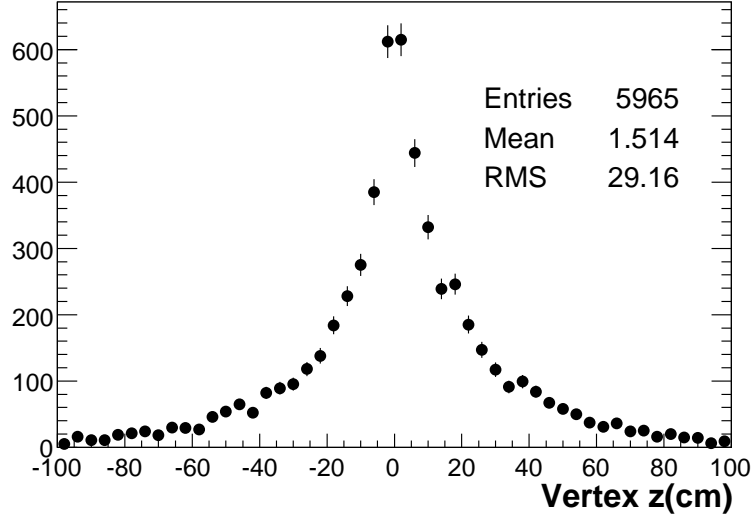


Figure 4.22. Z-vertex distribution during the high  $\beta^*$  run.

First random numbers are generated for the  $|t|$  and  $\xi$  values from the distribution function. The azimuthal angle  $\phi$  is generated from a uniform random distribution between 0 and  $2\pi$ . To account for the beam spot size a Gaussian smearing of mean 0 and standard deviation 50 cm. Figure 4.22 shows the z-vertex distribution during the high  $\beta^*$  run. The beam divergence is modeled by Gaussian smearing of standard deviation of  $50\mu\text{Rad}$  applied to  $\Theta_x$  and  $\Theta_y$ . The particles that are produced at the interaction point are propagated using the beam transport matrices to the forward detectors. If the particle hits the forward detectors then the detector resolution effects are applied to the hit coordinates. After the hit coordinates are obtained from the simulation, these are fed to the standard FPD reconstruction program like the real data.

Figure 4.23 and 4.24 shows the hit coordinates of single diffractive events obtained from the monte carlo program. The hits are compared to the hits from the elastic events (data) and elastic band cuts. Figure 4.23 shows the events for the

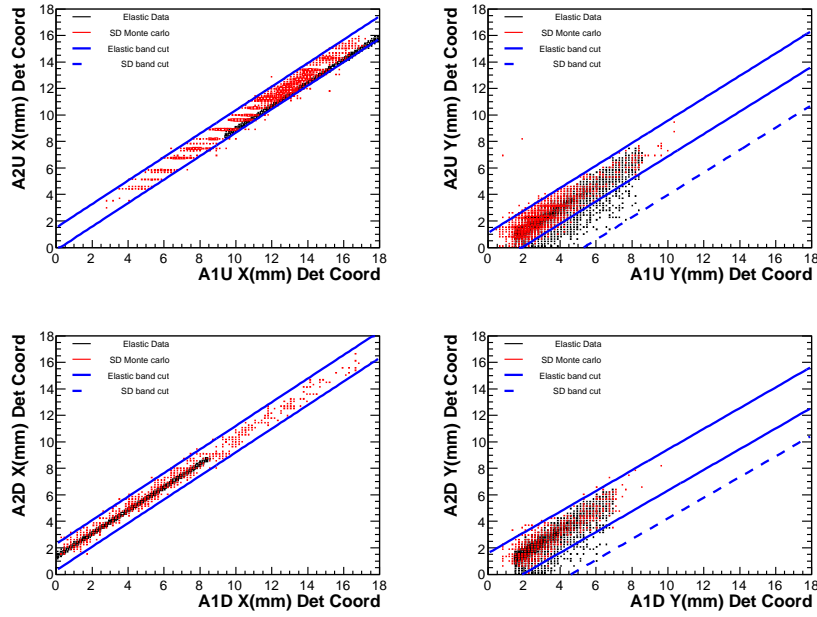


Figure 4.23. Figure showing the use of single diffractive Monte Carlo used to determine the single diffractive detector correlation cuts for AU and AD detectors.

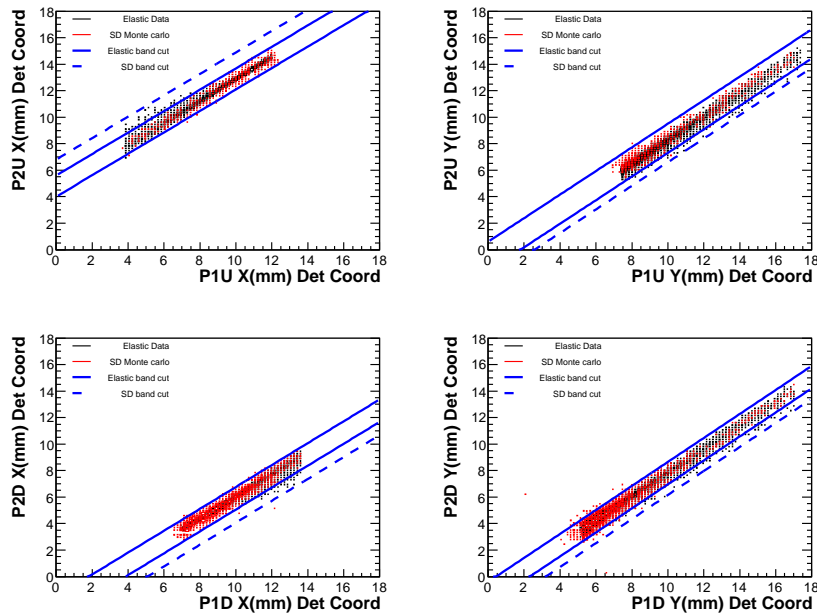


Figure 4.24. Figure showing the use of single diffractive Monte Carlo used to determine the single diffractive detector correlation cuts for PU and PD detectors.



A-side spectrometers (both X and Y coordinates) and Fig. 4.24 shows the P-side spectrometers. It can be seen that the single diffractive events hit different regions of the detectors compared to the elastic events. This is because of the fact that the elastic events have  $\xi = 0$  whereas single diffractive events can have  $\xi > 0$ , which alters their trajectory. Also there is difference between the P-side hits and A-side hits. This because of the fact that the rotation of the beam ellipse is different on A-side and P-side.

Table 4.9. Single diffractive band cut equations

Spec.	X Lower cut	X Upper cut	Y Lower cut	Y Upper cut
AU	$-0.2 + 0.887.x$	$1.5 + 0.887.x$	$-4.5 + 0.847.x$	$1.1 + 0.847.x$
AD	$0.3 + 0.891.x$	$2.3 + 0.891.x$	$-3.6 + 0.782.x$	$1.6 + 0.782.x$
PU	$4.0 + 0.809.x$	$6.8 + 0.809.x$	$-2.3 + 0.890.x$	$0.6 + 0.890.x$
PD	$-4.2 + 0.826.x$	$-1.5 + 0.826.x$	$-2.9 + 0.905.x$	$-0.4 + 0.905.x$

#### 4.4.3.2 Single diffractive band cuts

The single diffractive band cuts shown in Fig. 4.23 and Fig. 4.24 are chosen such that all the single diffractive monte carlo events are included inside the bands. Table 4.9 list the equations of the upper and lower straight lines used as single diffractive detector correlation cuts. These straight line equations are used as inputs during the reconstruction of data for the single diffractive event selection.

#### 4.4.4 Halo rejection

Beam halo background is the most abundant background for the single diffractive events. From the halo distribution plots in Fig. 4.8, it can be seen that the proton

side halo is approximately 10 times greater than the anti-proton side halo. To reject halo events from the event selection sample trigger scintillators are used. Figure 4.7 illustrates the halo tagging mechanism for the forward detectors. The black line in the figure shows the path of a proton halo track, since in this case the halo particle hits the A1U and A2U scintillators early. The halo bit is set in this case as there is a hit in the early time window and an hit in the in-time window in the diagonally opposite side spectrometer. In order to reject the halo tracks for the event selection, the tracks with halo bits ON on either of the diagonally opposite side detectors are rejected.

#### 4.4.5 Detector fiducial cuts

Fiducial cuts are used to equalize the acceptance of the spectrometers on the proton and the anti proton side. Applying the fiducial cuts also give better halo rejection. In the elastic analysis it was observed that once a proton has passed through a specific region of a detector the anti proton would also pass through a similar but a little bit wider region of the diagonally opposite side detector. But due to the finite size of the detectors the equivalent regions may not be completely covered by the second detector. This effect is particularly more pronounced at the edges of the detectors.

The calculation of good fiducial regions for the four spectrometers is described in details in the elastic analysis. In this method the proton and the anti-proton side spectrometers are divided into cells. For each of the cells in the spectrometer the effective cell location on the diagonally opposite side spectrometer is calculated by using the equation

$$x_p = \frac{L_{xp}}{L_{x\bar{p}}} x_{\bar{p}} \quad (4.4)$$

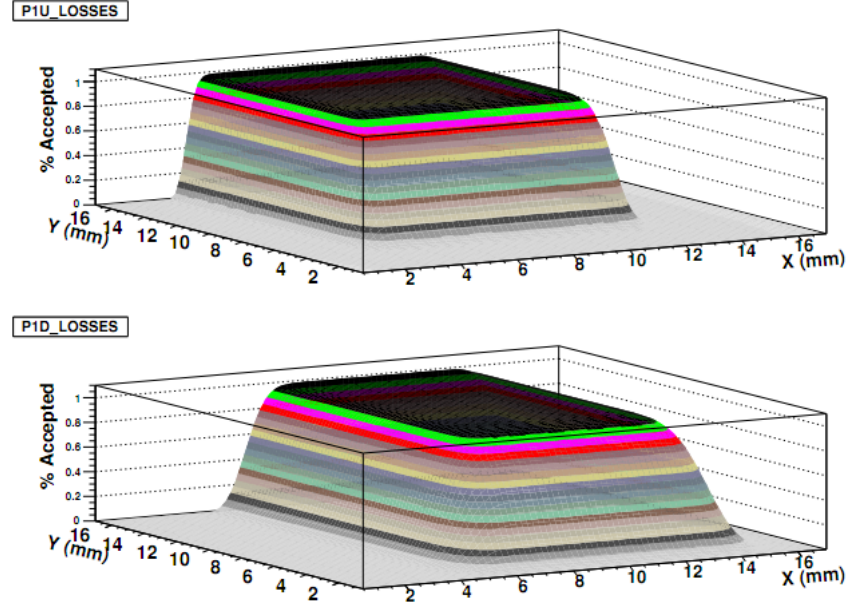


Figure 4.25. Fraction of events accepted in the P1U and P1D detectors due to the finite size of the detector (relative acceptance) [1].

where  $L_{xp}$ ,  $L_{x\bar{p}}$  are the effective lengths in the horizontal plane and  $L_{yp}$ ,  $L_{y\bar{p}}$  are the effective length in the vertical plane. Once there is a particle in the proton side spectrometer, one can calculate the acceptance for the equivalent cell on the anti-proton side. With this method cell by cell acceptance can be calculated for each of the spectrometers. After calculating the relative acceptances fiducial cuts are applied to detectors to use only the regions such that the relative acceptance is more than 98%. The fiducial cuts are applied only to the P1 and A1 detectors. Figure 4.25 shows the active area of the P1U and P1D detectors. The black region in the Lego plot shows 100% relative acceptance. The table shows the active regions of the A1 and P1 detector that are used in the analysis.

#### 4.5 Corrections to single diffractive cross section

To calculate the differential cross section from the raw distribution of events various correction factors have to be applied. The differential cross section can be written in terms of the raw distribution and correction factor as follows

$$\frac{d\sigma}{d|t|} = \left( \frac{1}{\mathcal{L} \times A \times \epsilon} \right) \frac{dN}{d|t|} \quad (4.5)$$

- $\frac{d\sigma}{d|t|}$  is the differential cross section.
- $\frac{dN}{d|t|}$  is the raw distribution of events.
- $\mathcal{L}$  is the integrated luminosity of the data set.
- $A$  is the geometrical acceptance. This is made up of two acceptances  $A_{fpd}$  which is the geometric acceptance of the FPD detectors and  $A_{lm}$  which is the geometric acceptance of the luminosity monitors. The second term has to be included because of hit requirement in the luminosity monitors.
- $\epsilon$  is the efficiency, this has also two parts. First one is the  $\epsilon_{trig}$  which is the trigger efficiency and the second is the efficiency of the luminosity monitor  $\epsilon_{lm}$

Each of these correction factors are described in details in the following sections

##### 4.5.1 Geometric acceptance

The FPD spectrometers do not have complete  $\phi$  coverage. Figure 4.26 shows the phi coverage of a single detector. The concentric ellipses are the contours of equal  $|t|$ , it can be seen from the figure that for a given  $|t|$  value the spectrometer has a different acceptance. Because of this finite coverage of the detector in phi each  $|t|$  bin of data has to be corrected for the geometric acceptance of the detector. In the single diffractive differential cross section calculation each of the  $|t|$  bins of data has a

different coverage in  $\phi$ . The acceptance correction corresponds to the fraction of the  $|t|$  ellipse that is not covered by the detector for each  $|t|$  bin.

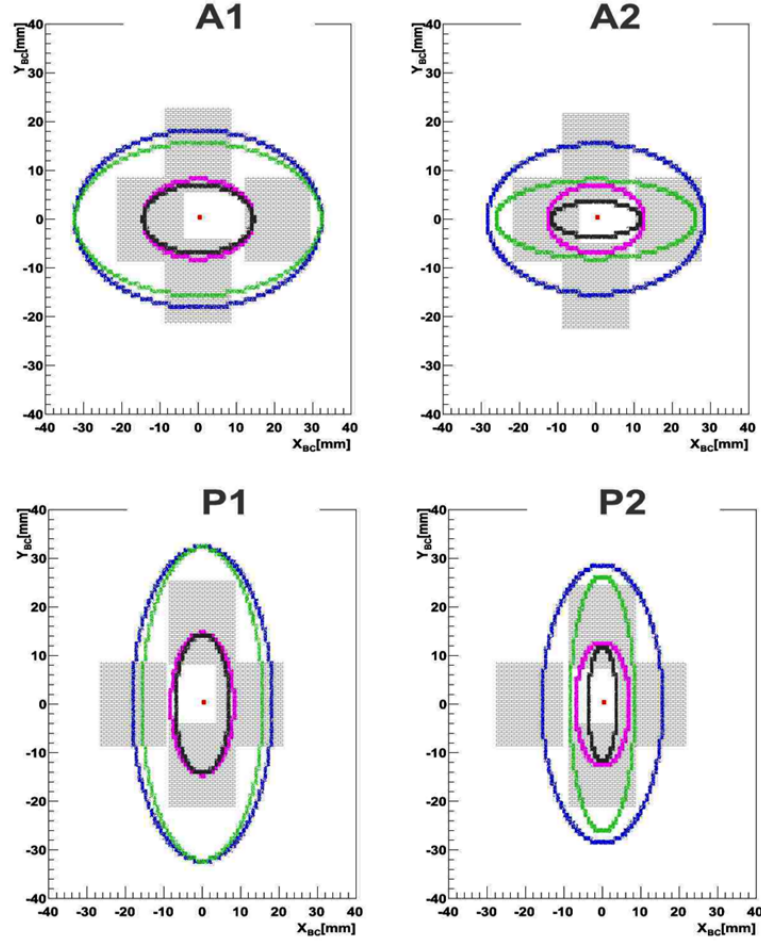


Figure 4.26. Fraction of events accepted in the P1U and P1D detectors due to the finite size of the detector. Beam shapes for 5 kinematic situations  $((\xi, |t|), \text{color}) = ((0,0), \text{red}); ((0,2.5), \text{blue}); ((0.08,2.5), \text{green}); ((0,0.05), \text{pink})$  and  $((0.08,0.05), \text{grey})$ .

In order to calculate the dependence of geometric acceptance for each  $|t|$  bin, the Monte Carlo method described in previous sections is used. The acceptance of a given spectrometer is defined as follows

$$A_{GEO} = \frac{N(\text{Reconstructed})}{N(\text{Generated})} \quad (4.6)$$

Figure 4.27 show the geometric acceptance of the four spectrometers in bins of  $|t|$  for three different acceptance functions with single diffractive slope of 4.02 GeV, 3.00 GeV and 5.00 GeV. It can be seen that the change in the acceptance because of the choice of ansatz function is relatively small. This topic is revisited in more detail during the calculation of the systematics.

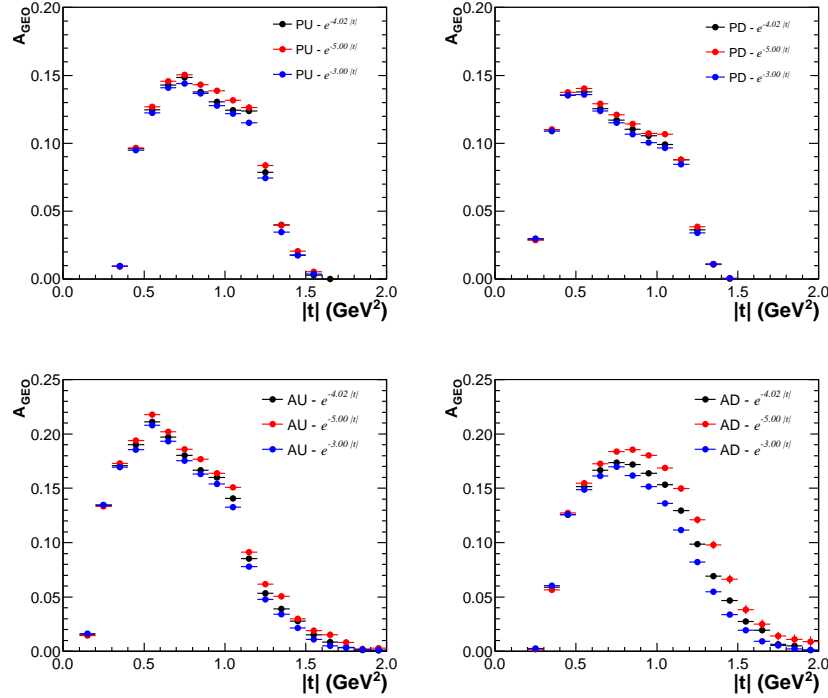


Figure 4.27. The change in the acceptance function of four spectrometers due to choice of ansatz function.

The effect of the beam smearing is shown in Fig. 4.28. The figure shows the plots of the acceptance function for a un-smearred and smeared beam, again the changes to the acceptance function is very small because of the beam smearing. Finally to corrected for the limited acceptances of the spectrometers the acceptance function corresponding to the anzahl function with a slope of -4.02 has been used.

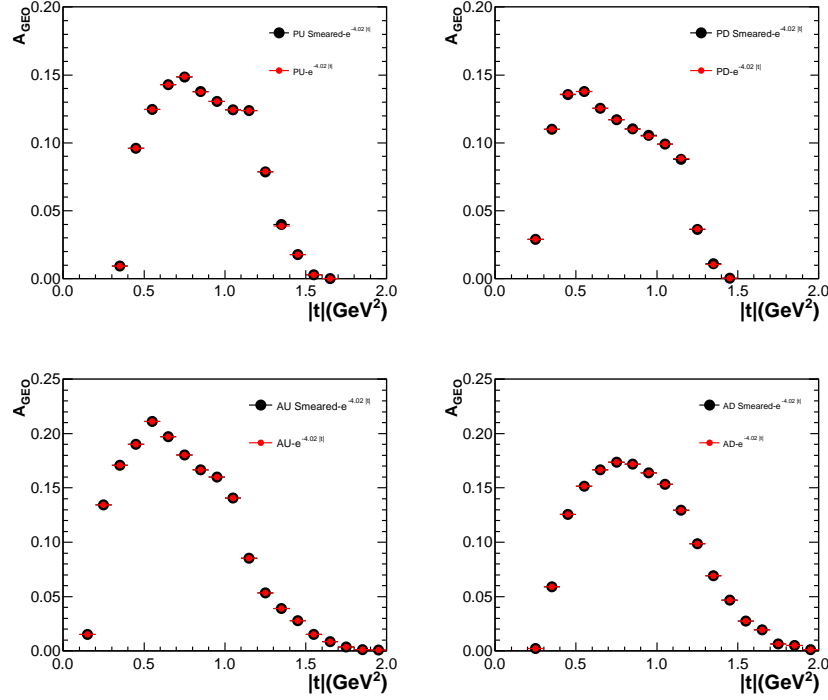


Figure 4.28. The change in the acceptance function of four spectrometers due beam smearing.

#### 4.5.2 Trigger efficiencies

The trigger, hit and selection efficiencies for the detectors used in the analysis are calculated in such a way that a single efficiency is obtained for each of the detectors. To calculate the efficiencies elastic events are used which is orthogonal

sample for the single diffractive events. One of the objectives is to calculate the  $|t|$  dependence of the trigger efficiency. For this purpose the efficiencies are calculated in bins of  $|t|$ . Since single diffractive events and elastic events have different kinematics,  $\xi = 0$  for elastic events vs.  $\xi > 0$  for single diffractive events. It is necessary to verify if single diffractive events and elastic events hit the same region of the detector for a given bin of  $|t|$ . The trigger efficiencies are direct functions of where the particles hit the detectors. If the protons from single diffractive events and elastic events hit the same region of detector for a given  $|t|$  bin, then the efficiencies calculated from the elastic events can be used to calculate the efficiencies for the single diffractive events.

Figure 4.29 to 4.36 show the hit maps for the A1U, A2U, A1D, A2D, P1U, P2U, P1D and P2D detectors respectively. The black points show the hits from single diffractive event selection and the red point shows hits from the elastic events. It can be seen from the figure that the hits go to same region of the detectors in each  $|t|$  bin. This shows that the efficiencies for the single diffractive events can be calculate using the elastic event selection.

The motivation to calculate the trigger efficiencies of the detectors in this analysis is because of the differences in hit finding and event selection in the FPD reconstruction as compared to the elastic reconstruction. Another objective in this trigger efficiency calculation is to have a larger statistics sample for the calculation of the efficiencies. To calculate the efficiencies of the individual detectors we use the triggers that were configured for this purpose: 1)TXX, which requires only one TIGHT hit in the first proton and anti-proton detectors and can be used to calculate the efficiencies of the second detectors. 2)XTXT which can be used to calculate the efficiencies of the second detectors in similar way.

In the first step, the efficiency calculation method used in the elastic analysis is applied to FPD reconstruction dataset to calculate the trigger efficiencies. As



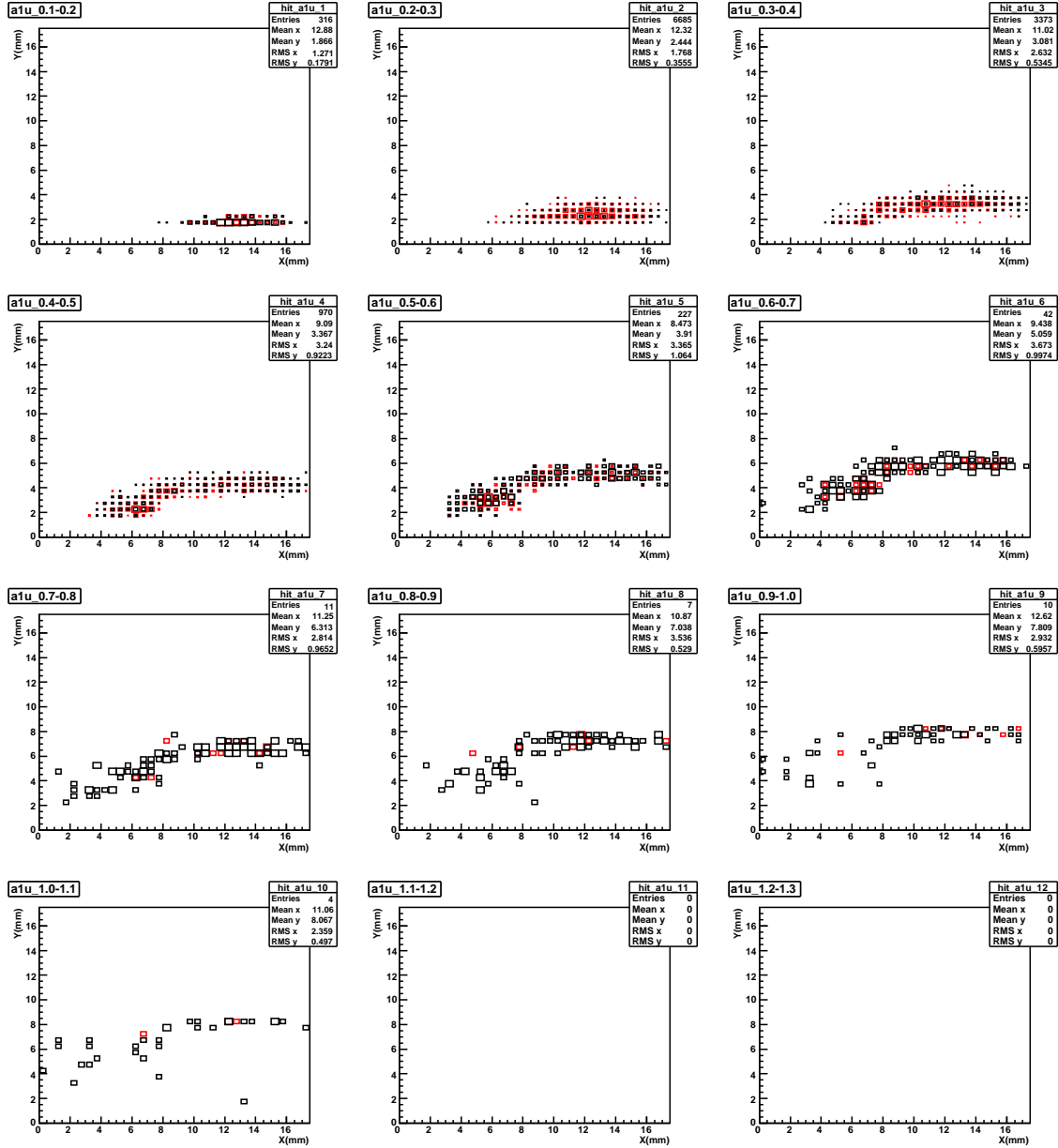


Figure 4.29. Hit maps for the elastic events (red) compared to the single diffractive events (black) for the detector A1U.

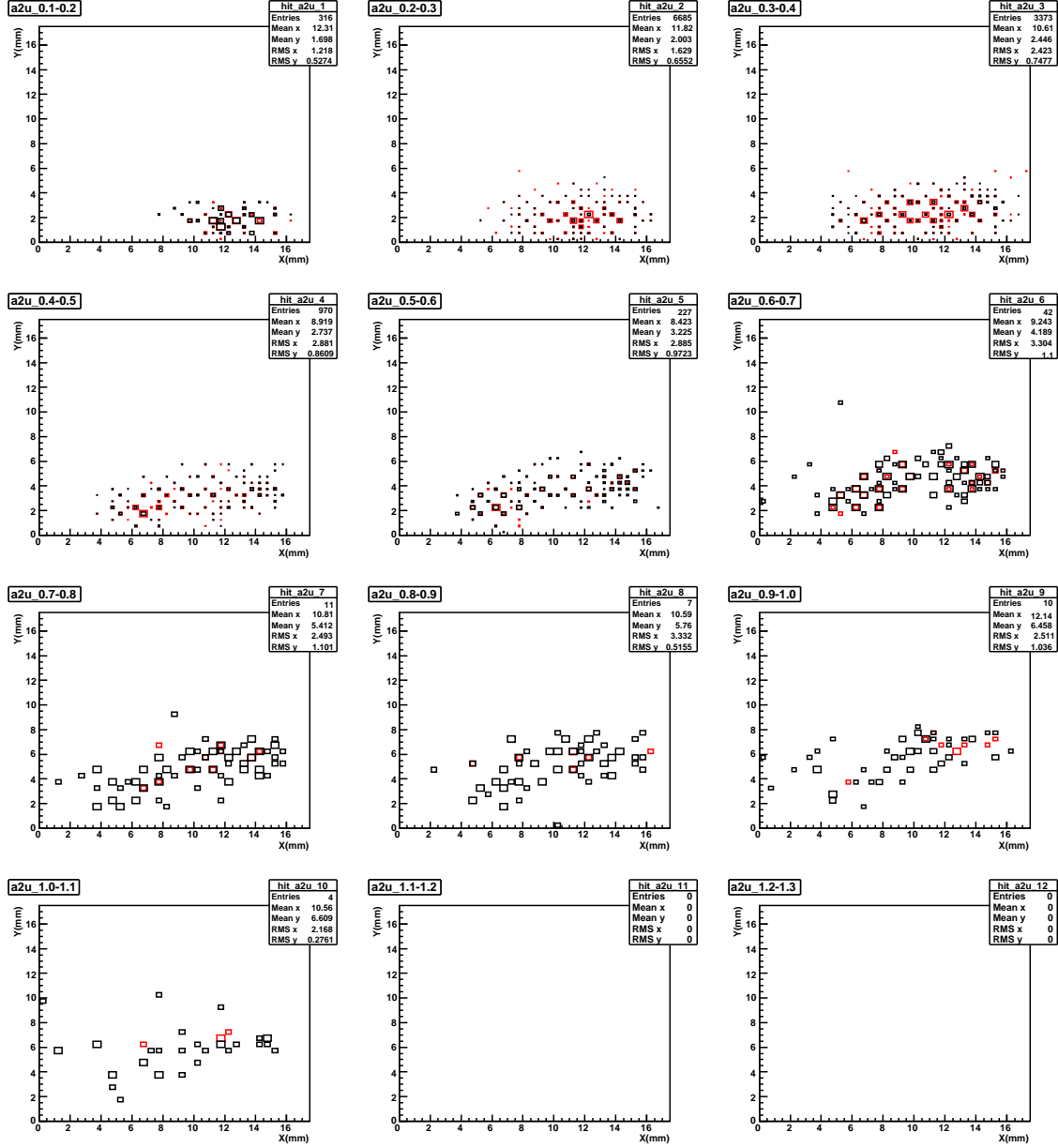


Figure 4.30. Hit maps for the elastic events (red) compared to the single diffractive events (black) for the detector A2U.

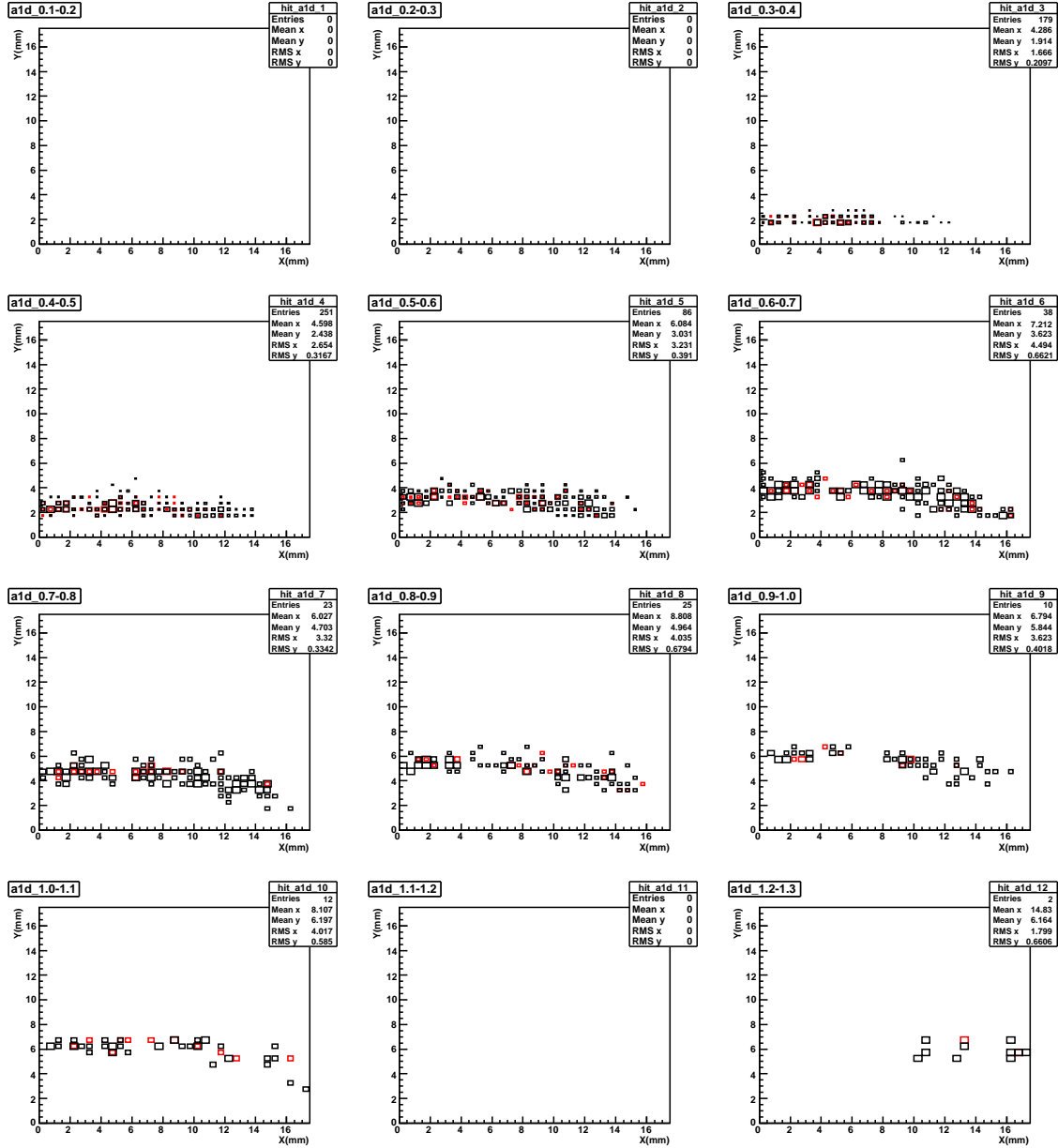


Figure 4.31. Hit maps for the elastic events (red) compared to the single diffractive events (black) for the detector A1D.

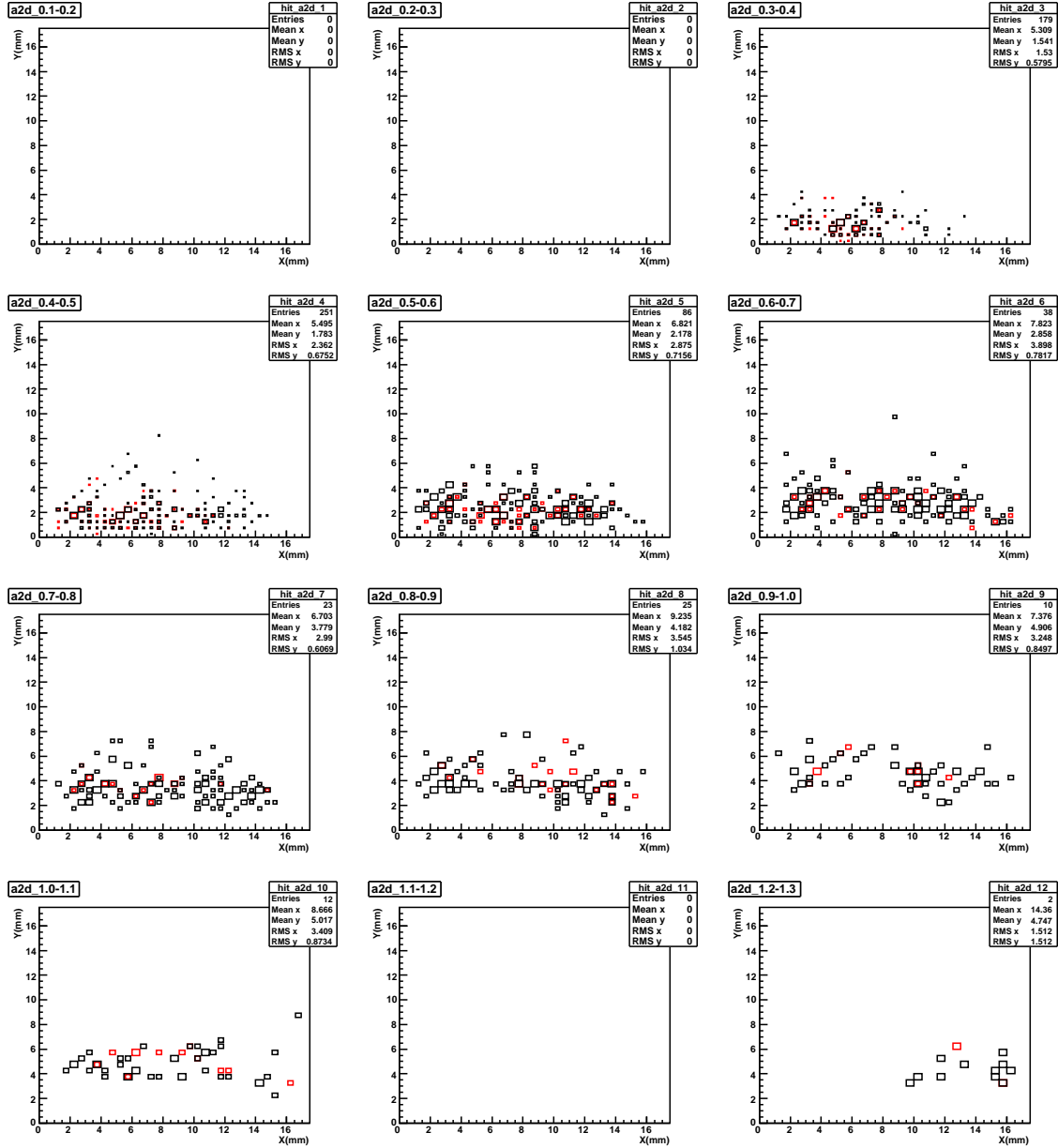


Figure 4.32. Hit maps for the elastic events (red) compared to the single diffractive events (black) for the detector A2D.

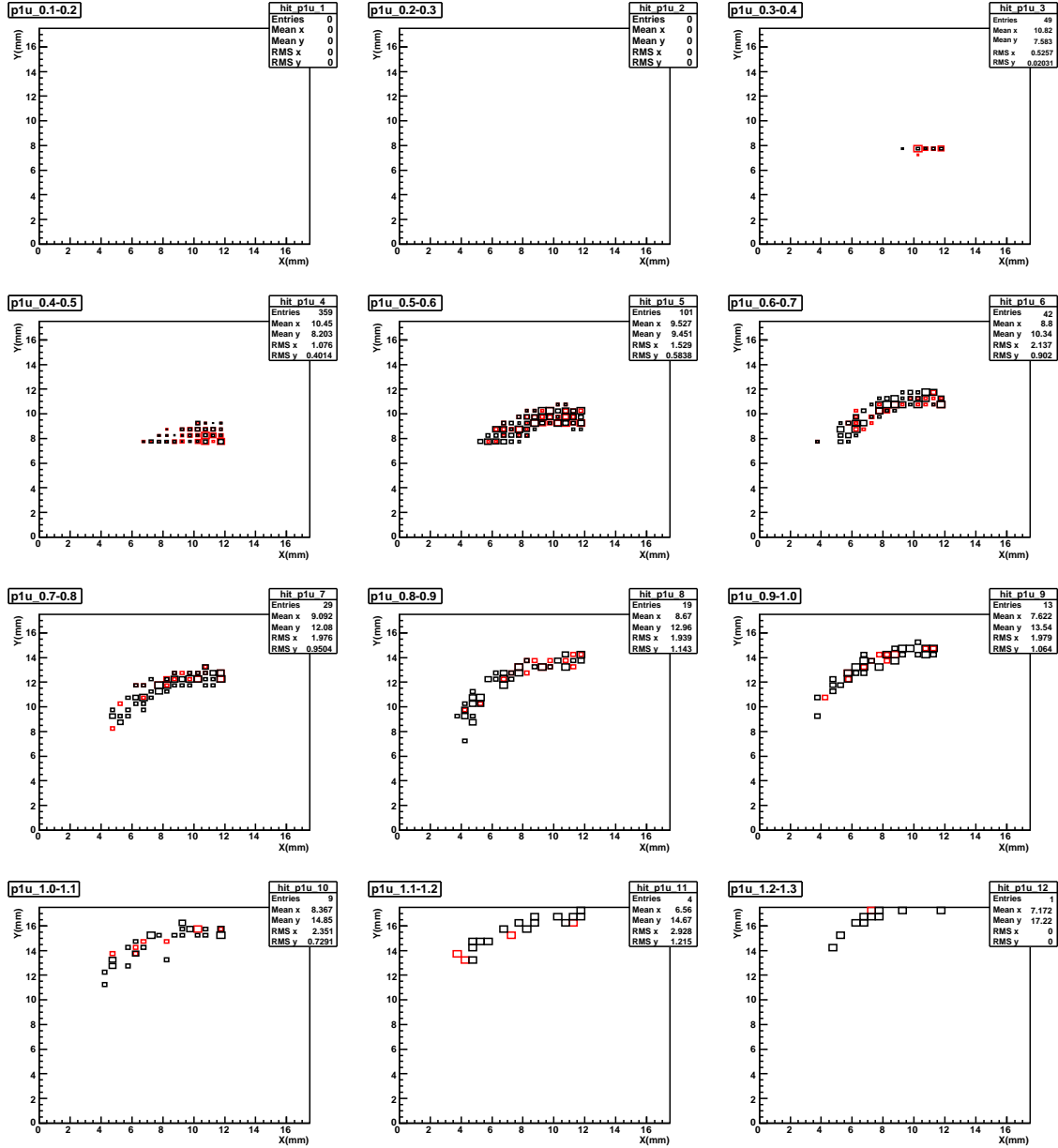


Figure 4.33. Hit maps for the elastic events (red) compared to the single diffractive events (black) for the detector P1U.

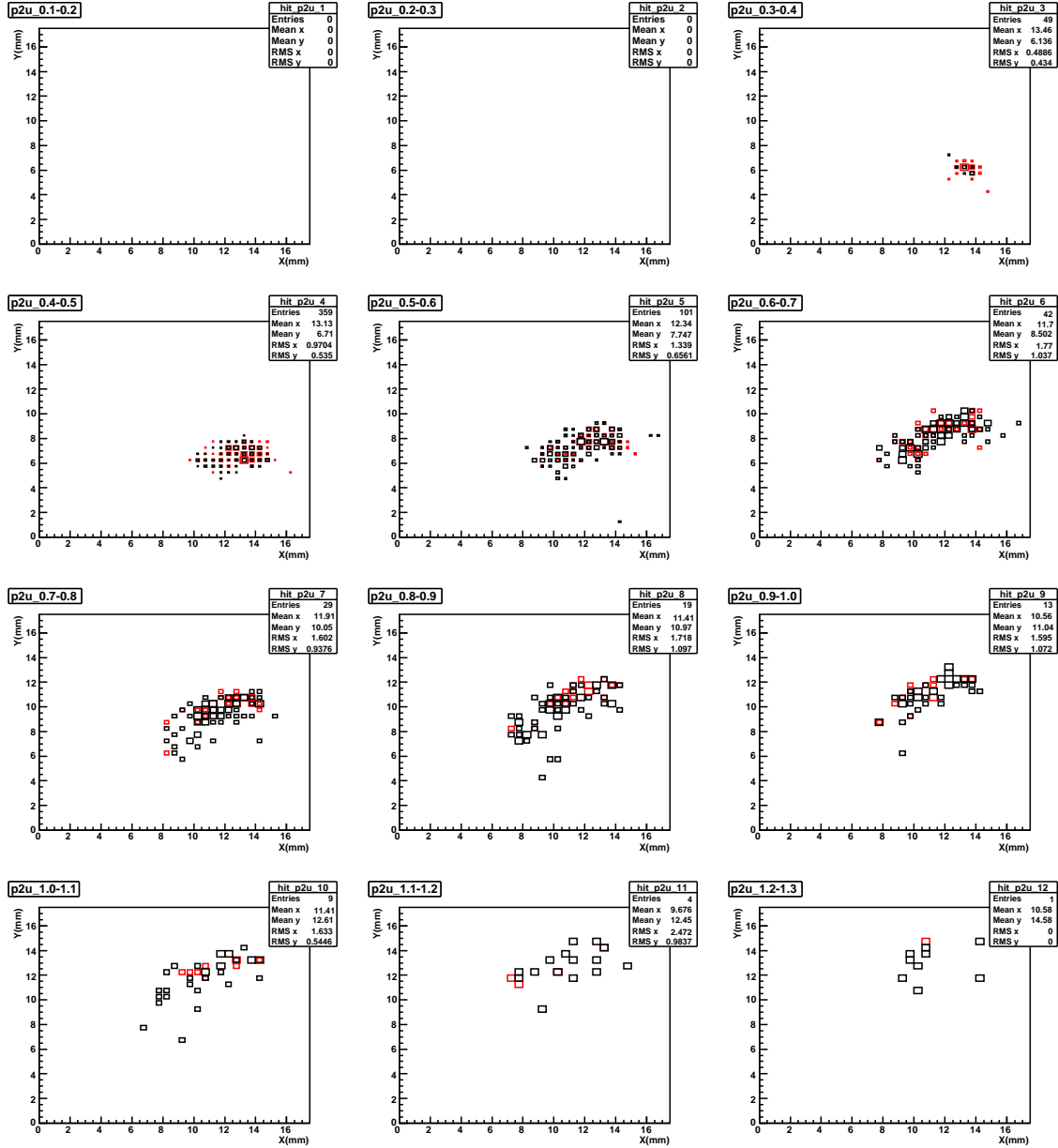


Figure 4.34. Hit maps for the elastic events (red) compared to the single diffractive events (black) for the detector P2U.

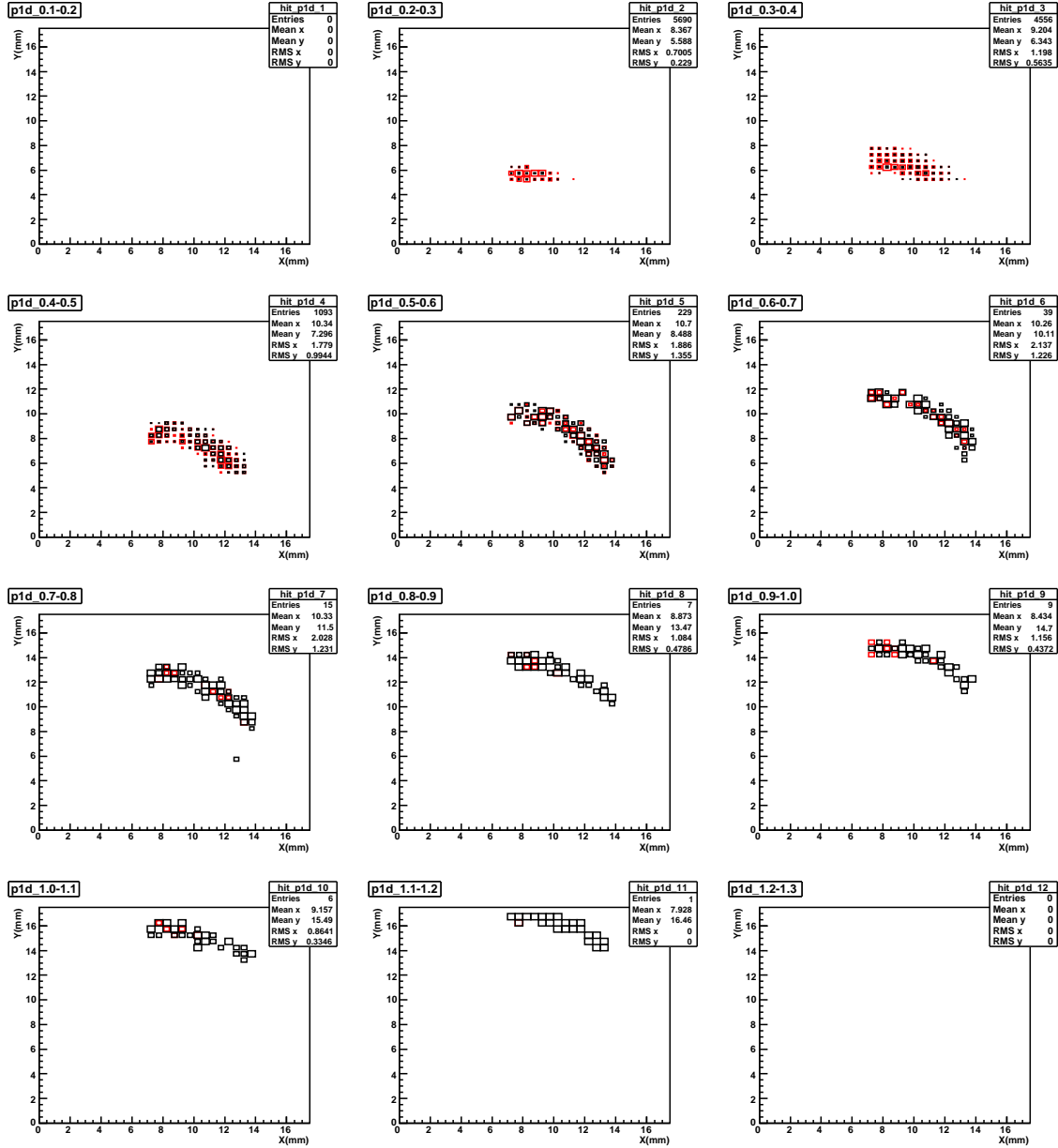


Figure 4.35. Hit maps for the elastic events (red) compared to the single diffractive events (black) for the detector P1D.

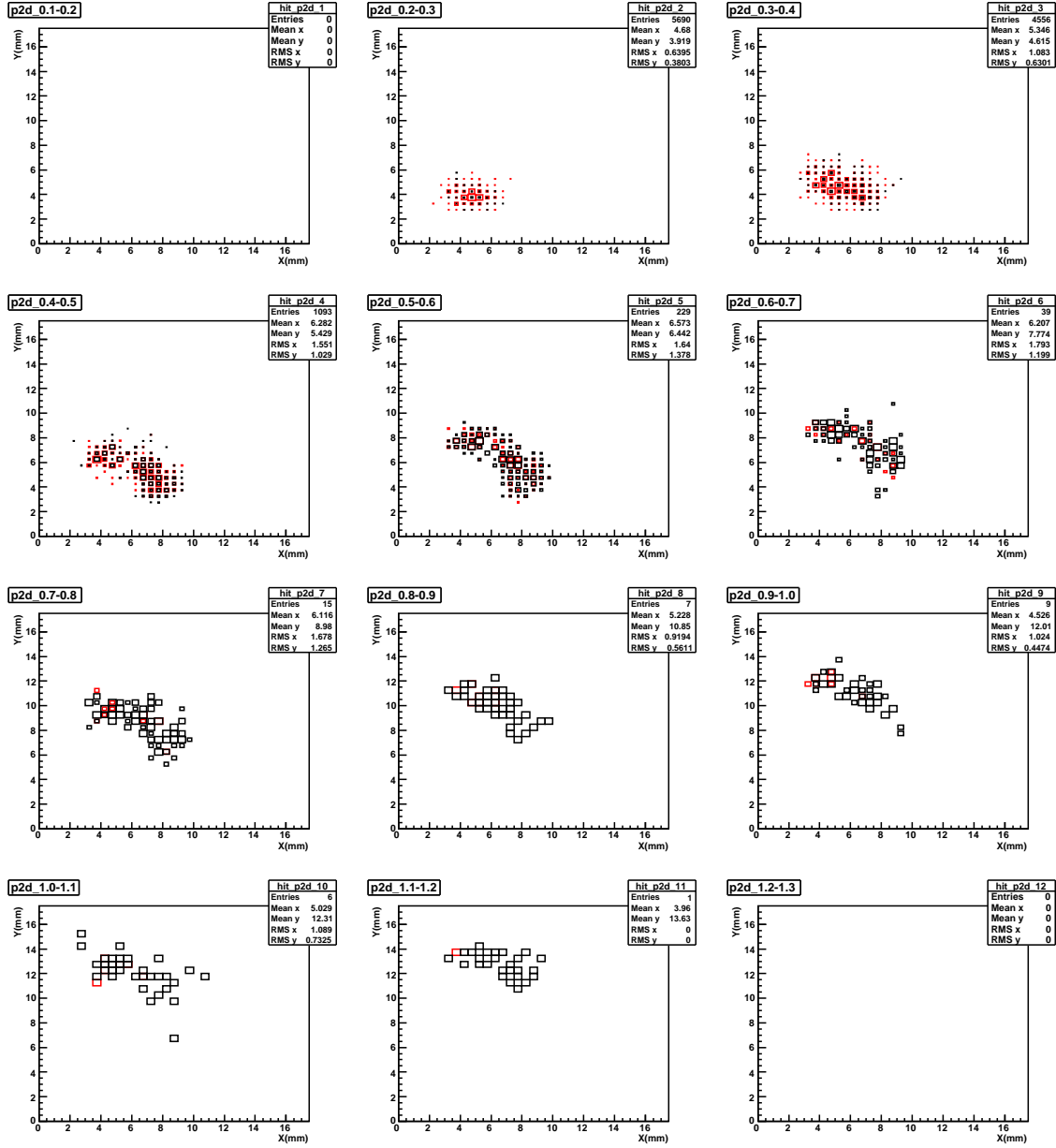


Figure 4.36. Hit maps for the elastic events (red) compared to the single diffractive events (black) for the detector P2D.



an example the steps to calculate the trigger efficiencies of A2U detector using the method used in the elastic analysis is described below, for the sake of clarity this sample would be called TT-XT sample.

- Choose events with ELAS2 trigger in the TTX configuration.
- Demand that all the detectors except for A2U detector has tight hits.
- Demand that the hits in the detectors A1U and P1D are inside the good fiducial region described in the event selection.
- Demand that hits in the A1U and P1D are within the elastic correlation band.
- The number of events satisfying the above conditions gives the denominator.

In addition to the above conditions if the event also has a tight hit in the A2U detector then the event is counted in the numerator. The ratio of the number of the events in the numerator to denominator gives the combined trigger, hit and selection efficiency of the A2U detector. In order to have more statistics for the sample used to calculate the efficiencies the TT (Tight, Tight) condition on the P1D and P2D detectors is relaxed and a track is demanded instead of the two tight hits. This track could come from a Loose or Medium hit as well. This sample is called Track-XT sample. Similarly to calculate the first detector efficiencies the ELAS2 trigger with TTX configuration is used.

Table 4.10 shows the trigger efficiencies calculated for the FPD detectors using both the samples using the above mentioned method. It can be seen that both the samples gives similar values of the efficiencies. In this case it is better to use the Track-TT sample because it has higher statistics. In this sample only a forward track on the diagonally opposite side spectrometer is required, so this is limited by only the LOOSE trigger efficiency which is much higher than the TIGHT trigger requirement. So in order to calculate the trigger efficiencies we use the Track-TT sample.

Table 4.10. Efficiencies for the FPD detectors using the TT-XT and Track-XT samples

Detector	Track-XT Sample	TT-XT Sample
A1U	$0.704 \pm 0.109$	$0.701 \pm 0.009$
A1D	$0.615 \pm 0.069$	$0.604 \pm 0.032$
P1U	$0.572 \pm 0.235$	$0.583 \pm 0.023$
P1D	$0.683 \pm 0.205$	$0.681 \pm 0.004$
A2U	$0.366 \pm 0.006$	$0.363 \pm 0.004$
A2D	$0.377 \pm 0.021$	$0.372 \pm 0.016$
P2U	$0.571 \pm 0.026$	$0.546 \pm 0.016$
P2D	$0.579 \pm 0.007$	$0.576 \pm 0.004$

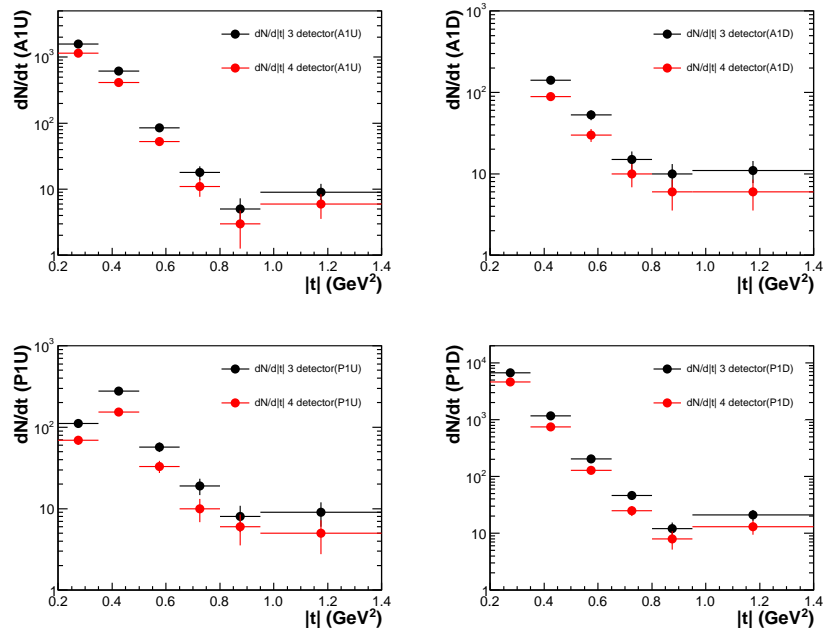


Figure 4.37. Distribution of 3 detector hit events and 4 detector hit events for the calculation of trigger efficiencies of the first detectors.

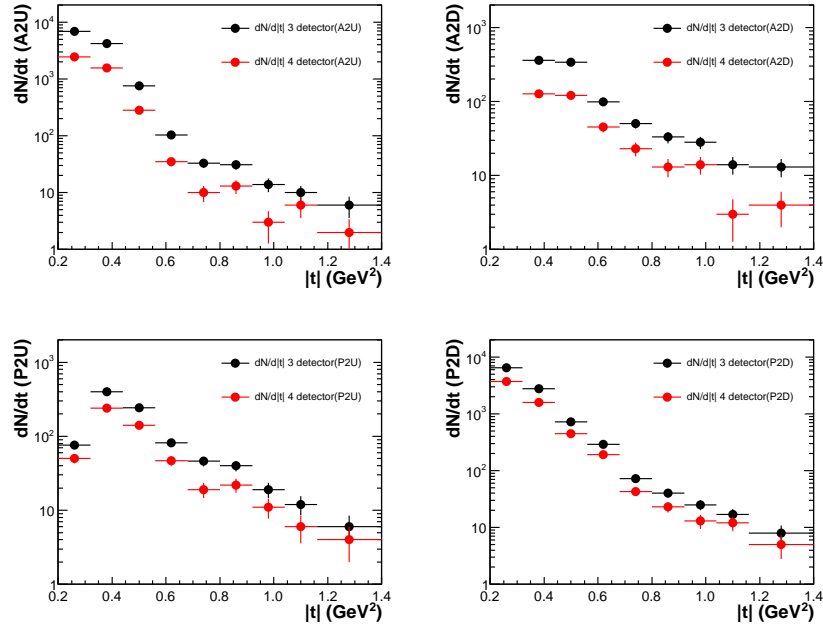


Figure 4.38. Distribution of 3 detector hit events and 4 detector hit events for the calculation of trigger efficiencies of the second detectors.

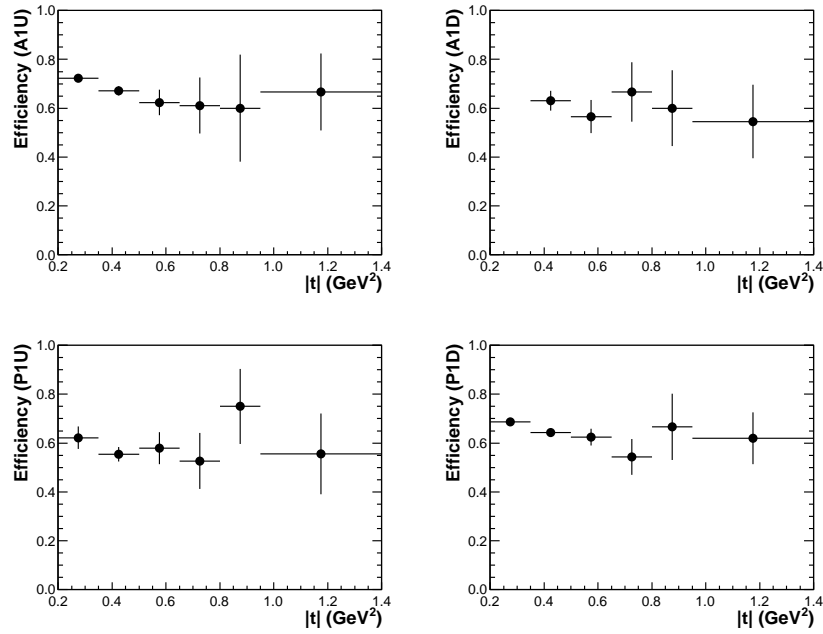


Figure 4.39. Efficiencies for the first detectors of the A-side and P-side spectrometers given as a function of  $|t|$ .

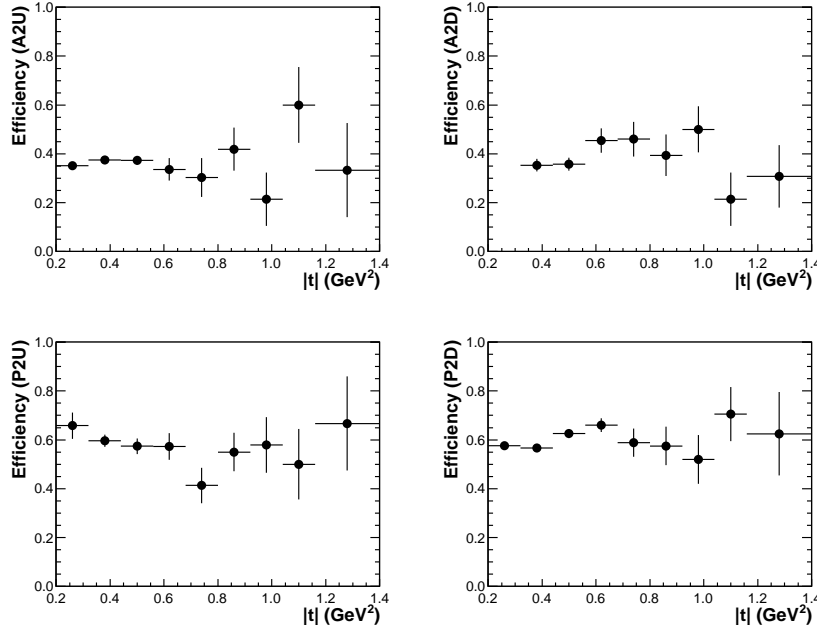


Figure 4.40. Efficiencies for the second detectors of the A-side and P-side spectrometers given as a function of  $|t|$ .

The next important thing for efficiencies is to check the  $|t|$  dependence. Figure 4.37 shows the number of events for 3 detector hits (XT-Track) in  $|t|$  bins ( $\frac{dN}{d|t|}$ ) in black and 4 detector hits (TT-Track) in bins of  $|t|$  for the first detectors of the four spectrometers used in the analysis. Figure 4.38 shows the number of 3 detector hits events (TX-Track) and 4 detector hit events (TT-Track) in bins of  $|t|$  for the second detectors for the four spectrometers. Figure 4.39 shows the bin by bin trigger efficiencies for the first detectors of the spectrometers. This is obtained by dividing the number of events in 4 detector hit histogram by the 3 detector hit histograms. The error bars shown in the trigger efficiency plots are binomial error bars. The next Fig. 4.40 shows the trigger efficiencies for the second detectors of the spectrometers. It can be seen that there is very less  $|t|$  dependence of the trigger efficiencies. Thus the trigger efficiencies for the detectors are taken to be single numbers instead of

fitted functions. Table 4.11 shows the trigger efficiencies for the eight detectors and the associated errors. These errors are binomial errors.

Table 4.11. Combined efficiencies for the FPD detectors using Track-XT samples which includes trigger efficiency, hit finding efficiency and selection efficiency

Detector	Efficiencies
A1U	$0.704 \pm 0.009$
A1D	$0.615 \pm 0.032$
P1U	$0.572 \pm 0.023$
P1D	$0.683 \pm 0.004$
A2U	$0.366 \pm 0.004$
A2D	$0.377 \pm 0.016$
P2U	$0.571 \pm 0.016$
P2D	$0.579 \pm 0.004$

From the the table 4.11 it can be seen that the efficiencies obtained for all the detectors is higher than those in the elastic analysis. This is due to the fact that the elastic analysis used different hit finding and different algorithm to select hits for the track reconstruction. The  $|t|$  dependence observed in the elastic analysis could be due to the maximum ADC hit finding method. In this method in elastic analysis the maximum ADC hit is found in the detector and the if it is not inside the detector correlation band the event is reject, at higher  $|t|$  the resolution of the detectors become worse so more hits are rejected on this basis, this could be reason of the lower efficiency at higher  $|t|$  values in the elastic analysis.

To cross check the new trigger efficiencies, elastic events are selected using the event selection described in the elastic analysis note. The data used to select the elastic events is from the Fpd reconstruction describe in the previous sections. The efficiencies values are same as derived above. Using the geometric acceptances from

the elastic analysis the elastic cross section is calculated. Figure 4.41 shows the differential cross section distribution calculated using the Fpd reconstruction and the elastic analysis data points. This proves the point that the Fpd reconstruction really has a higher efficiency. This also shows the validation of all the other steps of the analysis and the fact that the fpd reconstruction is consistent with the elastic data as well as the single diffractive data.

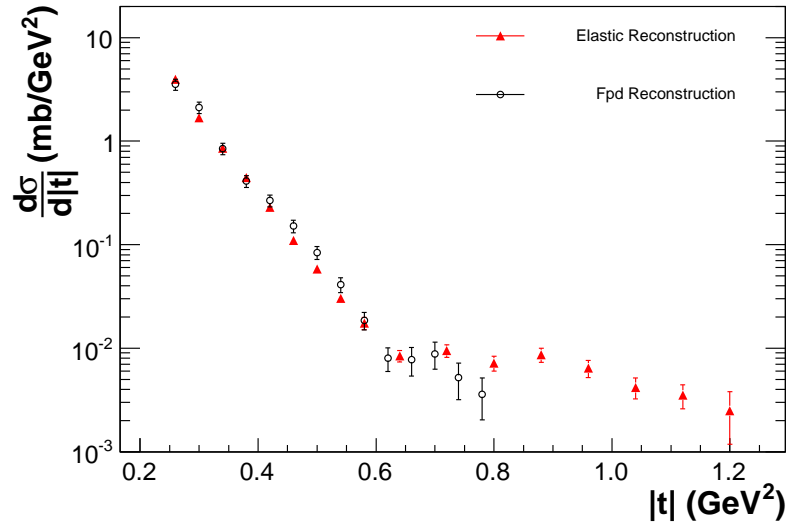


Figure 4.41. Elastic differential cross section distribution calculated using the Fpd reconstruction and data point from the elastic analysis.

### 4.5.3 Luminosity

The luminosity of the special FPD store 4647 was determined using a new algorithm [60]. The basic idea is based on the fact that both the data sets have inclusive jet triggers. The integrated luminosity for the special store is determined by calculating the ratio of the number of events with inclusive jet triggers in the store 4647 and the number of events with inclusive jet triggers in RunIIa. Since the

efficiencies of the jet triggers is same from the 4647 store and the RunIIa dataset the following equation holds

$$\frac{N_{Fpd}}{\mathcal{L}_{Int,Fpd}} = \frac{N_{RunIIa}}{\mathcal{L}_{Int,RunIIa}} \quad (4.7)$$

Here  $N$  is the number of events for each datasets with inclusive jet triggers. Since the prescales for the RunIIa and the Fpd store are different, the prescale factors have to be taken into account for the above equations. There are no un-prescaled inclusive jet triggers in the Fpd store. Also the the jet trigger efficiencies are assumed to be same but the vertex efficiency due to different beam shape has to be taken into account for the calculation of the luminosity. The final equation that is used is given by

$$\mathcal{L}_{Int,Fpd} = \left( \frac{N_{Fpd} \cdot P_{Fpd}}{N_{RunIIa}} \right) \cdot \frac{\epsilon_{RunIIa}}{\epsilon_{Fpd}} \cdot \mathcal{L}_{Trig,RunIIa} \quad (4.8)$$

In the above equation  $P_{Fpd}$  is the prescale of the trigger in the Fpd dataset,  $\epsilon$  is the vertex efficiency for the two datasets and  $\mathcal{L}_{Trig,RunIIa}$  is the integrated luminosity of a given trigger in RunIIa dataset.

Table 4.12. Integrated luminosity for different run ranges in store 4647 calculated using the ratio of inclusive jet triggers

Run Numbers	Integrated Luminosity, $\mathcal{L}_{Int}(\text{nb}^{-1})$
215417-215421	$4.50 \pm 0.99$
215424-215430	$13.8 \pm 2.1$
215443	$1.41 \pm 0.13$
215445-215449	$6.77 \pm 1.1$
215433-215449	$12.6 \pm 1.6$

The table 4.12 shows the integrated luminosity obtained for the different run ranges. For this analysis the run ranges 215433-215449 are used. This gives a total integrated luminosity of  $12.6 \pm 1.6 \text{ nb}^{-1}$  for this analysis.

#### 4.5.4 High mass single diffractive fraction

In this analysis the single diffractive events which hit the luminosity monitor on the opposite side of the forward track. This implies that the events with  $M_x > 11.3 \text{ GeV}$  are selected. In order to correct the measure cross section for all  $M_x$  values the measured cross section is divided by the efficiency of the cut. The efficiencies of the single diffractive events that hit the luminosity monitor on the opposite side is calculate using Monte Carlo (PYTHIA) [61]. In this the case the data sample that is used for the proton side and anti-proton side are  $n(N) > 0 \ \&\& \ n(S) = 0$  and  $n(N) = 0 \ \&\& \ n(S) > 0$ , the fraction of these events out of the total single diffractive sample is  $0.218 \pm 0.006$  for both the cases as the cross section is symmetric for both the protons and anti-protons.



#### 4.6 Background estimation and subtraction

The main background after the single diffractive event selection is the untagged halo events. This type of background comes in because of the limited efficiency of the trigger scintillators on the diagonally opposite side spectrometers which are used to tag tracks as halo tracks. As an example consider the case of selecting forward tracks in PD spectrometer. In this case the PD track is tagged as a halo track if one of the two diagonally opposite side spectrometer A1U or A2U has a out of time trigger scintillator ON (Hit-Bit ON). If the efficiencies of the A1U and A2U trigger scintillators are given as  $\epsilon(A1U)$  and  $\epsilon(A2U)$  then the efficiency of tagging halo track is given by  $\epsilon(A1U)$  OR  $\epsilon(A2U)$

$$\epsilon(A1U) \text{ OR } \epsilon(A2U) = \epsilon(A1U) + \epsilon(A2U) - \epsilon(A1U) \cdot \epsilon(A2U) \quad (4.9)$$

The above expression is valid when the good fiducial regions are used in each of the above mentioned detectors.

The efficiencies of each of the scintillators are calculated using halo tracks that have been already tagged using the opposite side spectrometers. The tracks with SD\_PRO trigger or SD\_PBAR trigger are chosen depending whether it is a A-side or P-side detector. Then the efficiency of a trigger scintillator is given as follows (A1U)

$$\epsilon(A1U) = \frac{N(A1U \text{ Hitbit}) + N(A2U \text{ Hitbit})}{N(A2U \text{ Hitbit})} \quad (4.10)$$

Figures 4.42 to 4.45 show the trigger scintillator efficiencies for all the eight detectors used in the analysis as a function of  $|t|$ . It can be seen from the figures that there is no  $|t|$  dependence of the trigger scintillator efficiencies. This result is not unexpected, since the trigger scintillators are just a cube of scintillator material.

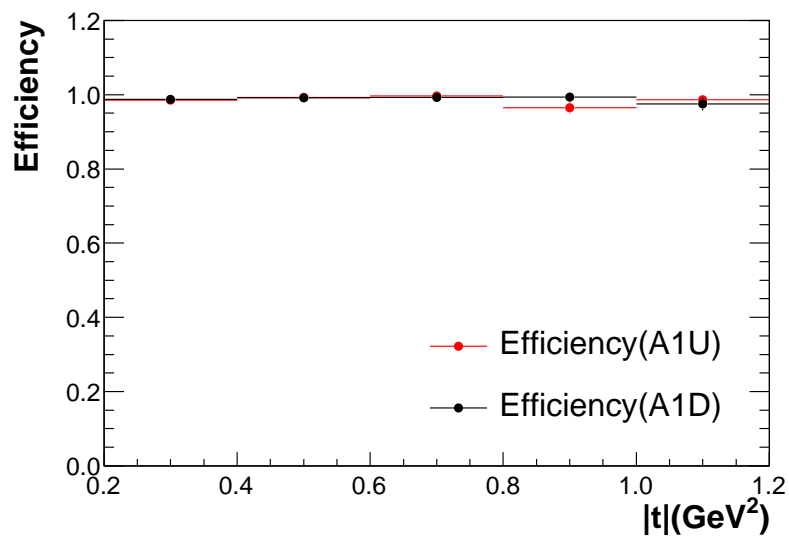


Figure 4.42. Efficiencies of the trigger scintillators for the A1U and A1D detectors.

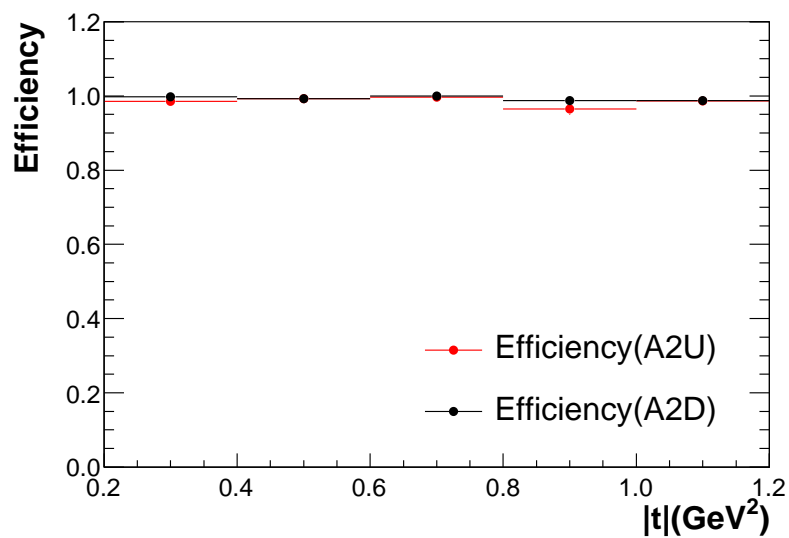


Figure 4.43. Efficiencies of the trigger scintillators for the A2U and A2D detectors.

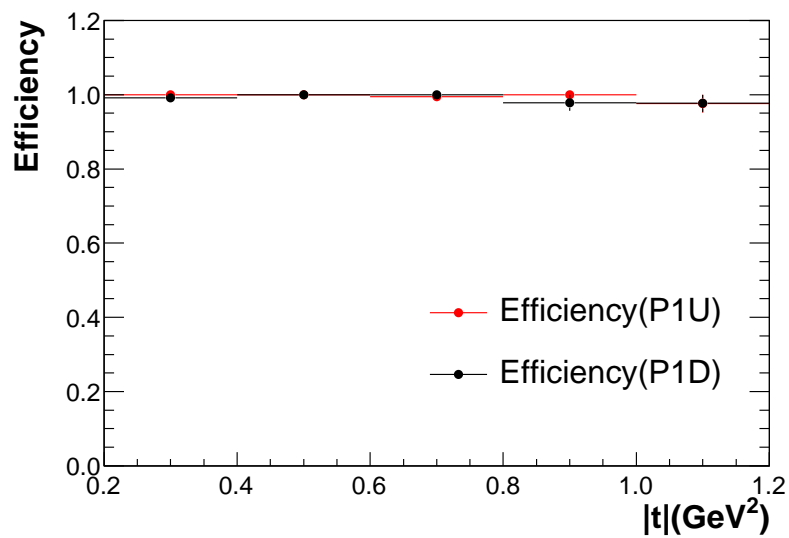


Figure 4.44. Efficiencies of the trigger scintillators for the P1U and P1D detectors.

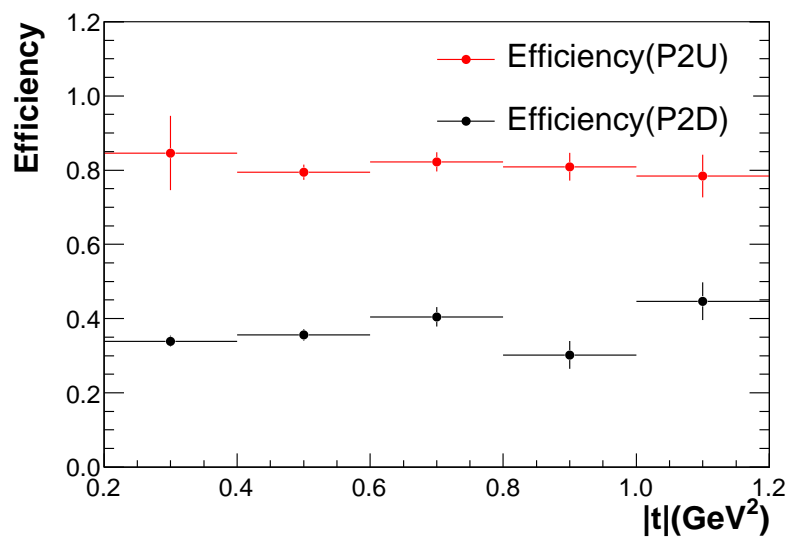


Figure 4.45. Efficiencies of the trigger scintillators for the P2U and P2D detectors.

Table 4.13 shows the efficiencies of the trigger scintillators for the eight detectors of interest. The lower efficiency of the P2 scintillators is believed to be due to radiation damage from showering of halo protons in the electrostatic separators.

Table 4.13. Trigger scintillator efficiencies

Detector	Efficiencies
A1U	$0.9904 \pm 0.0017$
A1D	$0.9912 \pm 0.0022$
P1U	$0.9934 \pm 0.0055$
P1D	$0.9903 \pm 0.0047$
A2U	$0.9904 \pm 0.0017$
A2D	$0.9951 \pm 0.0019$
P2U	$0.8053 \pm 0.0143$
P2D	$0.3549 \pm 0.0094$

The next step to estimate the background is to calculate the effective halo cross section. This is based on track events that have been tagged as halo using the one of the trigger scintillators on the diagonally opposite side. To calculate the effective halo cross section, all of the correction factor used in the determination of the signal are applied. Figure 4.46 shows the effective cross section of the tagged halo distribution.

This tagged halo cross section does not represent a background to the single diffractive cross section ( $\sigma_{sd}$ ), since it can be simply removed using the halo veto– the residual background ( $\sigma_{bg}$ ) is due to the inefficiency of the scintillators, which leads to untagged halo. Table 4.14 gives the spectrometer halo tagging efficiency ( $\mathcal{E}_{Halo}$ ), determined using Eq.4.9. Another source of untagged halo, would be an acceptance difference between diagonally opposite spectrometers, but the need for such a correction is removed by applying fiducial cuts to equalize the effective acceptance. The final

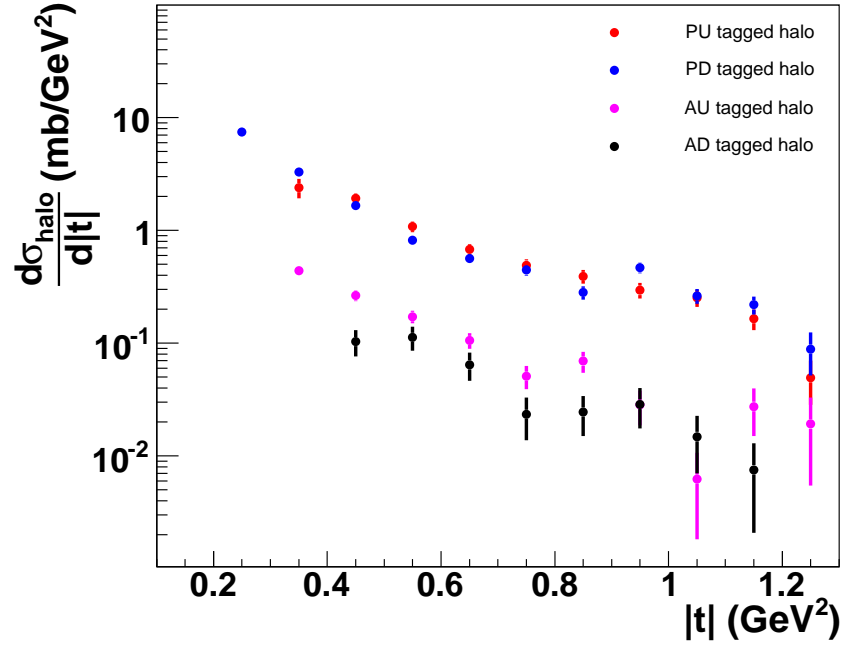


Figure 4.46. Tagged halo track cross section distribution in the four spectrometers.

residual background cross section that must be subtracted from the single diffractive cross section is thus given as

$$\sigma_{bg} = (1 - \mathcal{E}_{Halo}) \cdot \sigma_{halo} \quad (4.11)$$

Table 4.14. Halo tagging efficiencies ( $\mathcal{E}_{Halo}$ ) for the vertical FPD spectrometers

Detector	Eff. Halo Tagging ( $\mathcal{E}_{Halo}$ )
AU Track	$0.9976 \pm 0.0024$
AD Track	$0.9971 \pm 0.0029$
PU Track	$0.9847 \pm 0.0153$
PD Track	$0.9895 \pm 0.0105$

## 4.7 Kinematics of diffraction

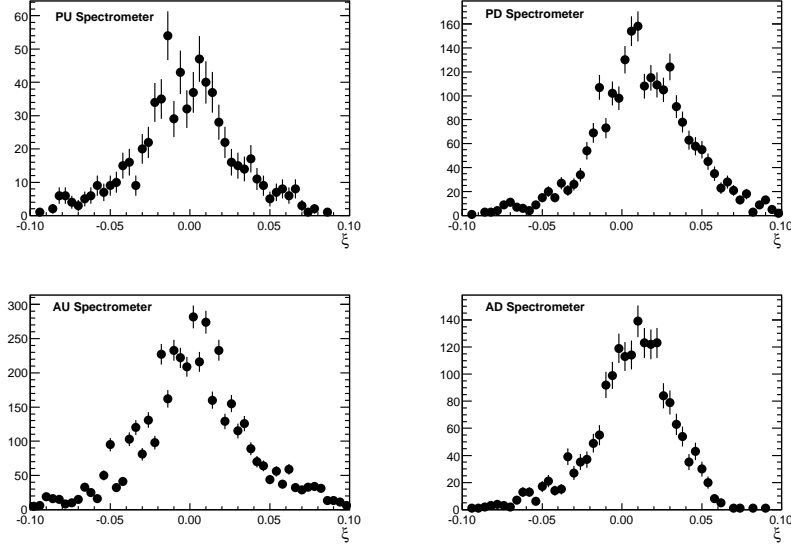


Figure 4.47.  $\xi$ -distribution of the single diffractive events in each spectrometers.

Since we use quadrupole spectrometers to measure diffraction, our  $\xi$  resolution is quite modest  $\sim 0.02$ . Nevertheless in Fig. 4.47 we show the distribution for the four spectrometers, this qualitatively meets the theoretical expectations. Theoretically  $d\sigma/d\xi = 1/\xi^{1.08}$  convoluted with a Gaussian of resolution 0.02, we thus expect a peak near  $\xi = 0$  with a slight tail in the positive direction.

Due to the diffractive system being boosted opposite to the detected proton (anti-proton), we expect an asymmetry in the track  $\eta$  distribution. This is shown in Fig. 4.48 where the asymmetry for the proton and anti-proton events are clearly observed and are in opposite directions.

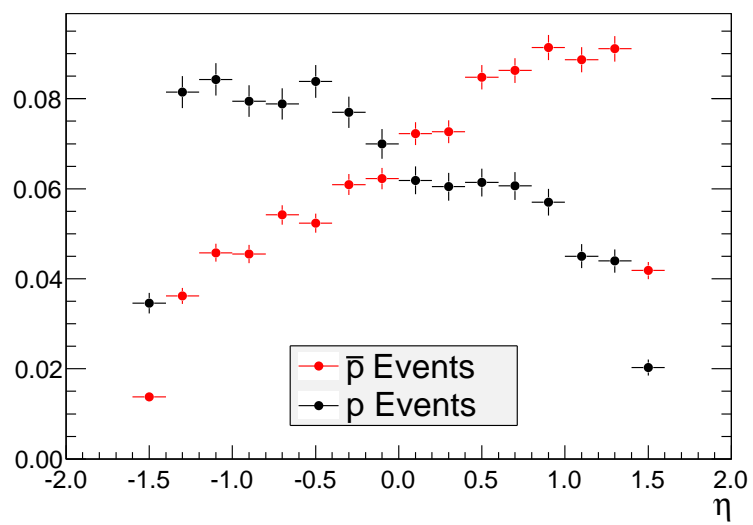


Figure 4.48.  $\eta$ -distribution of the central tracks for  $p$  and  $\bar{p}$  single diffractive events.

## CHAPTER 5

### RESULTS

#### 5.1 Single diffractive differential cross section

The single diffractive cross section is calculated using the following equation

$$\frac{d\sigma}{d|t|} = \left( \frac{1}{\mathcal{L} \times A \times \mathcal{E}} \right) \frac{dN}{d|t|} \quad (5.1)$$

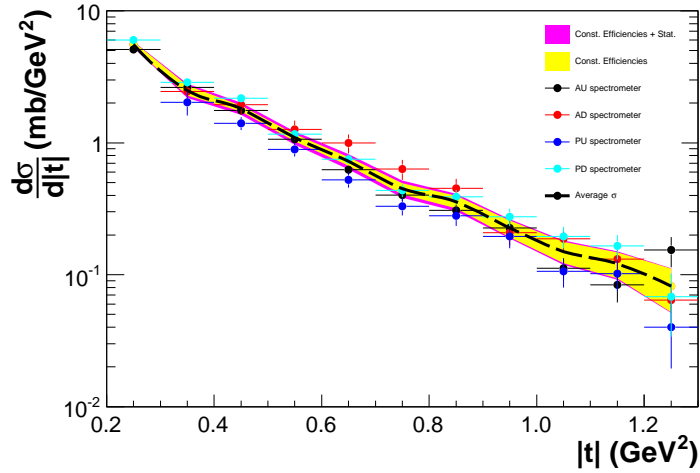


Figure 5.1. Single diffractive differential cross section  $\frac{d\sigma_{sd}}{d|t|}$  per GeV calculated using all four vertical spectrometers. The black dashed line shows the average of the cross section for each bin in  $|t|$ .

Here  $\frac{dN}{d|t|}$  is the raw distribution of the number of the events.  $\mathcal{L}$  is the total integrated luminosity of the number of events and is same for all the spectrometers and  $A$  is the acceptance of the spectrometer; this quantity is spectrometer dependent. The acceptance includes the geometrical acceptance and the acceptance due to the



hits in the luminosity monitor.  $\mathcal{E}$  is the combined efficiency of the spectrometer which includes the trigger efficiency, hit efficiency and the selection efficiency. This is also a spectrometer dependent quantity.

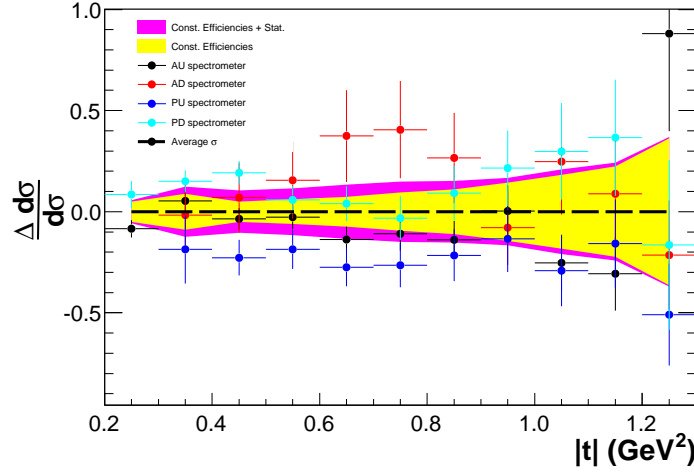


Figure 5.2. Deviation of the cross section in each bin of  $|t|$  from the average cross section for all the four spectrometers.

Figure 5.1 shows the single diffractive differential cross section  $\frac{d\sigma_{sd}}{dt}$  per GeV calculated using all of the four forward spectrometers. This plot shows the scatter of the cross section calculated using the four spectrometers. The dashed line shows the simple average (un-weighted) of the measurements of the cross section in each bin. The shaded yellow region shows the statistical uncertainty of the average cross section and the magenta shaded region shows the error introduced due to the statistical error in the calculation of the trigger efficiencies. This is a part of the total systematic uncertainty.

Figure 5.2 shows the deviation of the cross section measurements from the mean. The y-axis of the plot shows the difference in the cross section for the average divided

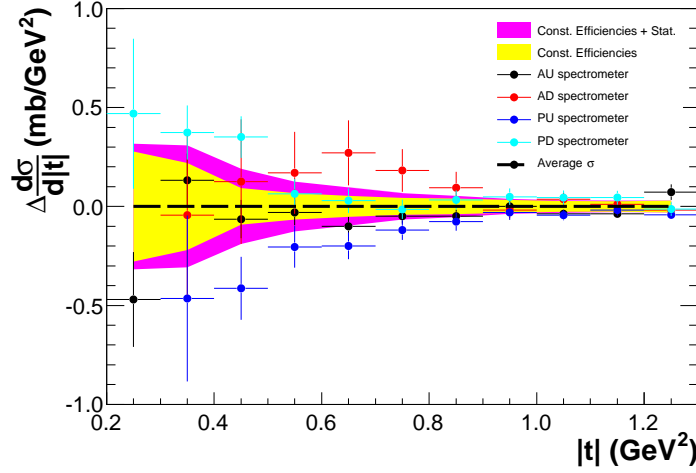


Figure 5.3. Difference between the cross section measurement for the four spectrometers from the average value.

by the cross section in that bin. Figure 5.3 shows the difference in the cross section of each spectrometer from the mean.

#### 5.1.1 Weighted average

In order to combine the cross section measurements from the four different spectrometers the individual cross section for each of the spectrometers should be weighted appropriately. The first weighting method used is simply the number of events in each spectrometer. In order to calculate the weighted average the following equation is used

$$\bar{\sigma}_{sd} = \sum_{i=1}^4 w_i \cdot \sigma_i \quad (5.2)$$

The errors are calculated according to the formula

$$E(\bar{\sigma}_{sd}) = \sqrt{\left( \sum_{i=1}^4 w_i^2 \cdot E(\sigma_i)^2 \right)} \quad (5.3)$$

Table 5.1. AU Spectrometer, Column 1 is the  $|t|$  value, column 2 is the raw number of events, column 3 is the raw number of events multiplied by the prescale, column 4 the acceptance of the forward spectrometer, column 5 is after the acceptance correction, column 6 is after the Luminosity correction, column 7 is after trigger efficiency correction, column 8 is after the LM efficiency correction, column 9 is the halo background, column 10 is the cross section, column 11 is after the acceptance correction of the LM and 12 and 13 are the statistical and systematic errors respectively

$ t $	$N$	$N_1$	$A_{geo}$	$N_2 = N_1/A_{geo}$	$N_3 = N_2/\mathcal{L}$	$N_4 = N_3/\mathcal{E}$	$N_5 = N_4/\mathcal{E}_{LM}$	Bkg.	$\sigma$	$\sigma/A_{LM}$	(stat.)	(syst.)
0.25	1348	46780	0.134	3.48e+05	0.0276	0.107	0.11	0	1.1	5.06	0.14	0.259
0.35	889	30760	0.171	1.8e+05	0.0143	0.0555	0.057	2.25e-05	0.57	2.62	0.0893	0.134
0.45	657	22880	0.19	1.2e+05	0.00954	0.037	0.0381	1.35e-05	0.381	1.75	0.0693	0.0893
0.55	446	15410	0.211	7.29e+04	0.00579	0.0225	0.0231	8.78e-06	0.231	1.06	0.051	0.0541
0.65	248	8430	0.197	4.28e+04	0.0034	0.0132	0.0135	5.41e-06	0.135	0.621	0.0401	0.0317
0.75	141	4950	0.18	2.74e+04	0.00218	0.00845	0.00868	2.6e-06	0.0868	0.398	0.0341	0.0204
0.85	102	3510	0.166	2.11e+04	0.00167	0.00649	0.00667	3.53e-06	0.0667	0.306	0.0308	0.0156
0.95	71	2480	0.16	1.55e+04	0.00123	0.00478	0.00491	1.44e-06	0.0491	0.225	0.0272	0.0115
1.05	31	1080	0.141	7.68e+03	0.000609	0.00236	0.00243	3.18e-07	0.0243	0.111	0.0204	0.00571
1.15	15	490	0.0853	5.74e+03	0.000456	0.00177	0.00182	1.4e-06	0.0182	0.0834	0.0219	0.00425
1.25	16	560	0.0532	1.05e+04	0.000835	0.00324	0.00333	9.8e-07	0.0333	0.153	0.039	0.00781

Table 5.2. AD Spectrometer, Column 1 is the  $|t|$  value, column 2 is the raw number of events, column 3 is the raw number of events multiplied by the prescale, column 4 the acceptance of the forward spectrometer, column 5 is after the acceptance correction, column 6 is after the Luminosity correction, column 7 is after trigger efficiency correction, column 8 is after the LM efficiency correction, column 9 is the halo background, column 10 is the cross section, column 11 is after the acceptance correction of the LM and 12 and 13 are the statistical and systematic errors respectively

$ t $	$N$	$N_1$	$A_{geo}$	$N_2 = N_1/A_{geo}$	$N_3 = N_2/\mathcal{L}$	$N_4 = N_3/\mathcal{E}$	$N_5 = N_4/\mathcal{E}_{LM}$	Bkg.	$\sigma$	$\sigma/A_{LM}$	(stat.)	(syst.)
0.35	256	8890	0.0588	1.51e+05	0.012	0.0517	0.0532	0	0.532	2.44	0.155	0.151
0.45	437	15050	0.126	1.2e+05	0.00952	0.041	0.0422	2.49e-06	0.422	1.94	0.0942	0.12
0.55	340	11810	0.151	7.8e+04	0.00619	0.0267	0.0274	2.7e-06	0.274	1.26	0.0694	0.0777
0.65	297	10220	0.167	6.13e+04	0.00487	0.021	0.0216	1.54e-06	0.216	0.99	0.0585	0.0611
0.75	194	6770	0.174	3.9e+04	0.00309	0.0133	0.0137	5.61e-07	0.137	0.629	0.0459	0.0388
0.85	140	4790	0.172	2.79e+04	0.00221	0.00954	0.0098	5.9e-07	0.098	0.45	0.0387	0.0278
0.95	64	2100	0.164	1.28e+04	0.00102	0.00439	0.00451	6.9e-07	0.0451	0.207	0.0263	0.0128
1.05	51	1770	0.153	1.15e+04	0.000916	0.00395	0.00406	3.56e-07	0.0406	0.186	0.0265	0.0115
1.15	29	1050	0.129	8.11e+03	0.000644	0.00278	0.00285	1.81e-07	0.0285	0.131	0.0247	0.00809
1.25	11	390	0.0986	3.96e+03	0.000314	0.00135	0.00139	0	0.0139	0.0639	0.0196	0.00395

Table 5.3. PU Spectrometer, Column 1 is the  $|t|$  value, column 2 is the raw number of events, column 3 is the raw number of events multiplied by the prescale, column 4 the acceptance of the forward spectrometer, column 5 is after the acceptance correction, column 6 is after the Luminosity correction, column 7 is after trigger efficiency correction, column 8 is after the LM efficiency correction, column 9 is the halo background, column 10 is the cross section, column 11 is after the acceptance correction of the LM and 12 and 13 are the statistical and systematic errors respectively

$ t $	$N$	$N_1$	$A_{geo}$	$N_2 = N_1/A_{geo}$	$N_3 = N_2/\mathcal{L}$	$N_4 = N_3/\mathcal{E}$	$N_5 = N_4/\mathcal{E}_{LM}$	Bkg.	$\sigma$	$\sigma/A_{LM}$	(stat.)	(syst.)
0.35	30	1680	0.00937	1.79e+05	0.0142	0.0436	0.0448	3.01e-06	0.448	2.05	0.381	0.117
0.45	201	11950	0.0961	1.24e+05	0.00987	0.0302	0.0311	2.42e-06	0.311	1.42	0.102	0.0814
0.55	164	9800	0.125	7.87e+04	0.00624	0.0191	0.0196	1.36e-06	0.196	0.901	0.0714	0.0515
0.65	115	6630	0.143	4.64e+04	0.00368	0.0113	0.0116	8.51e-07	0.116	0.531	0.0503	0.0304
0.75	72	4360	0.149	2.93e+04	0.00233	0.00712	0.00732	6.17e-07	0.0732	0.336	0.0401	0.0192
0.85	55	3410	0.138	2.48e+04	0.00197	0.00602	0.00619	4.92e-07	0.0619	0.284	0.0388	0.0162
0.95	38	2260	0.131	1.73e+04	0.00137	0.00421	0.00432	3.7e-07	0.0432	0.198	0.0327	0.0113
1.05	20	1180	0.124	9.49e+03	0.000753	0.00231	0.00237	3.18e-07	0.0237	0.109	0.0247	0.0062
1.15	18	1120	0.124	9.04e+03	0.000717	0.0022	0.00226	2.07e-07	0.0226	0.104	0.0247	0.00591
1.25	4	280	0.079	3.55e+03	0.000281	0.000862	0.000886	6.19e-08	0.00886	0.0406	0.0203	0.00232

Table 5.4. PD Spectrometer, Column 1 is the  $|t|$  value, column 2 is the raw number of events, column 3 is the raw number of events multiplied by the prescale, column 4 the acceptance of the forward spectrometer, column 5 is after the acceptance correction, column 6 is after the Luminosity correction, column 7 is after trigger efficiency correction, column 8 is after the LM efficiency correction, column 9 is the halo background, column 10 is the cross section, column 11 is after the acceptance correction of the LM and 12 and 13 are the statistical and systematic errors respectively

$ t $	$N$	$N_1$	$A_{geo}$	$N_2 = N_1/A_{geo}$	$N_3 = N_2/\mathcal{L}$	$N_4 = N_3/\mathcal{E}$	$N_5 = N_4/\mathcal{E}_{LM}$	Bkg.	$\sigma$	$\sigma/A_{LM}$	(stat.)	(syst.)
0.25	338	20300	0.029	7e+05	0.0555	0.14	0.144	1.37e-05	1.44	6.62	0.366	0.332
0.35	612	36400	0.11	3.31e+05	0.0263	0.0664	0.0683	6.02e-06	0.683	3.13	0.129	0.157
0.45	551	33030	0.136	2.43e+05	0.0193	0.0488	0.0502	3.04e-06	0.502	2.3	0.0997	0.116
0.55	297	17850	0.138	1.29e+05	0.0103	0.026	0.0267	1.5e-06	0.267	1.22	0.0722	0.0615
0.65	178	10580	0.125	8.43e+04	0.00669	0.0169	0.0174	1.03e-06	0.174	0.798	0.0608	0.0401
0.75	99	5830	0.117	4.98e+04	0.00395	0.00999	0.0103	8.16e-07	0.103	0.471	0.0481	0.0236
0.85	78	4800	0.11	4.36e+04	0.00346	0.00875	0.00899	5.17e-07	0.0899	0.412	0.0474	0.0207
0.95	58	3460	0.105	3.29e+04	0.00261	0.00661	0.00679	8.55e-07	0.0679	0.311	0.0416	0.0156
1.05	38	2260	0.0991	2.28e+04	0.00181	0.00458	0.0047	4.81e-07	0.047	0.216	0.0356	0.0108
1.15	29	1710	0.0885	1.93e+04	0.00153	0.00388	0.00398	4.02e-07	0.0398	0.183	0.0345	0.00916
1.25	5	290	0.0364	7.96e+03	0.000632	0.0016	0.00164	1.62e-07	0.0164	0.0753	0.0342	0.00378

Here  $\bar{\sigma}_{sd}$  is the mean cross section and  $E(\bar{\sigma}_{sd})$  is the error of the mean. The  $w_i$  are the weights assigned to each spectrometer. The weights are calculated from the number of events in each bin.

Table 5.5. Number of single diffractive events in each FPD spectrometer

Detector	N Events
AU	4352
AD	1846
PU	720
PD	2286

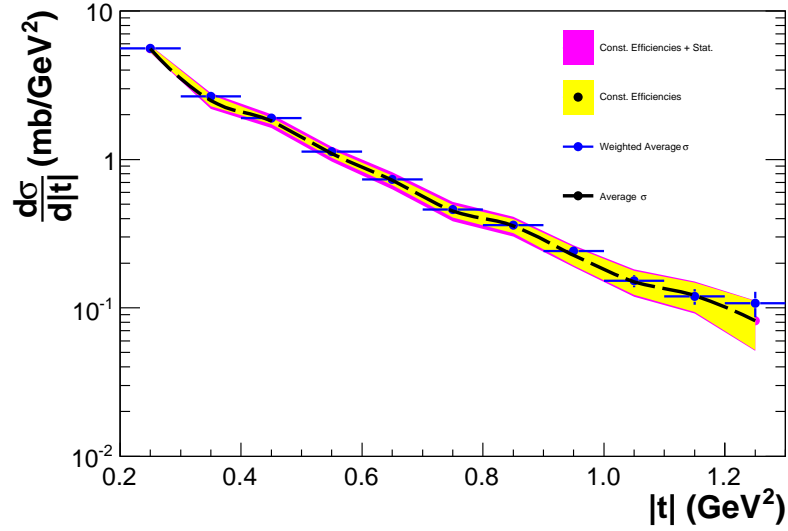


Figure 5.4. The weighted average of the single diffractive cross section calculated by weighting the four spectrometers according to the number of events. The black dashed line shows the simple average.

Table 5.5 shows the total number of single diffractive events in each spectrometer. Figure 5.4 shows the weighted average of the cross sections. This is compared with the simple average of the cross section (dashed line).

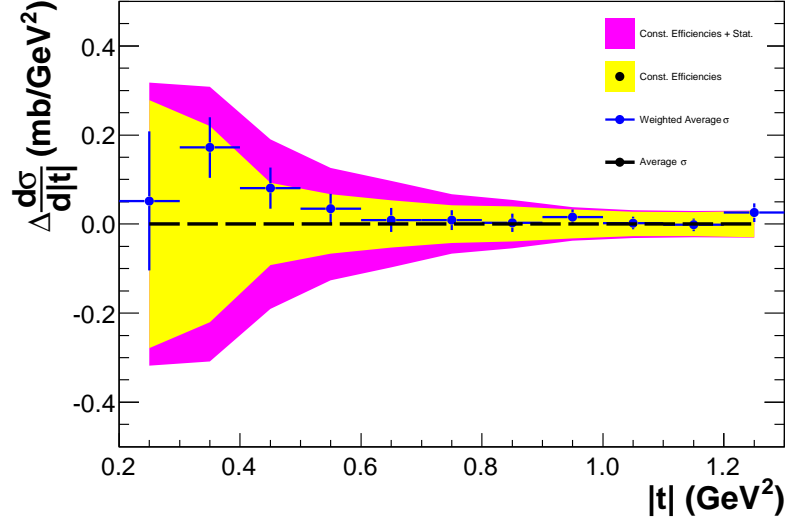


Figure 5.5. Difference between the simple average and the weighted average for the single diffractive cross section.

Figures 5.5 and 5.6 shows the difference and the deviation from the simple average. From these two plots it can be seen that the averaging method does not bias the cross section measurement significantly. For the sake of correctness the weighted average is used.

Since the event-weighting method is influenced strongly by the low- $|t|$  acceptance and somewhat by statistical fluctuations, we also have calculated weights based on the acceptance of the spectrometer in each bin multiplied by the efficiency of the spectrometer (this applies a higher weighting to the spectrometer that should have the best statistical power, removing the effect of statistical fluctuations). Figures 5.7



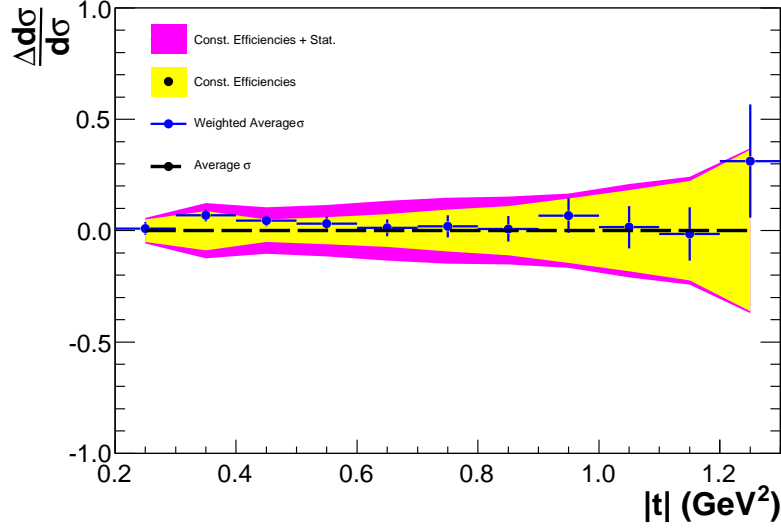


Figure 5.6. Deviation from the from the simple average and the weighted average for the single diffractive cross section.

and 5.8 show the cross section and the deviation of the cross section from the simple mean.

Figure 5.9 shows the single diffractive differential cross section calculated by weighting each spectrometer according to the number of events in them. This includes the statistical errors and the and statistical error for the trigger efficiencies with is a part of the systematic uncertainty.

### 5.1.2 Systematic uncertainties

The main sources of the systematic uncertainties for the single diffractive cross section measurement are the following

- Luminosity measurement.
- Trigger efficiency measurement.
- Luminosity monitor efficiency.
- Fraction of single diffractive events hitting the Luminosity monitor

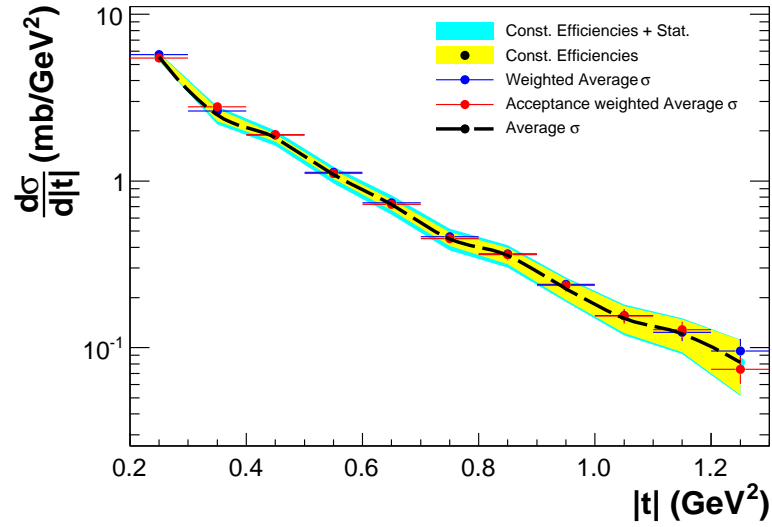


Figure 5.7. The weighted average of the single diffractive cross section calculated by weighing the four spectrometers according to the number of events and using the acceptance weighted average. The black dashed line shows the simple average.

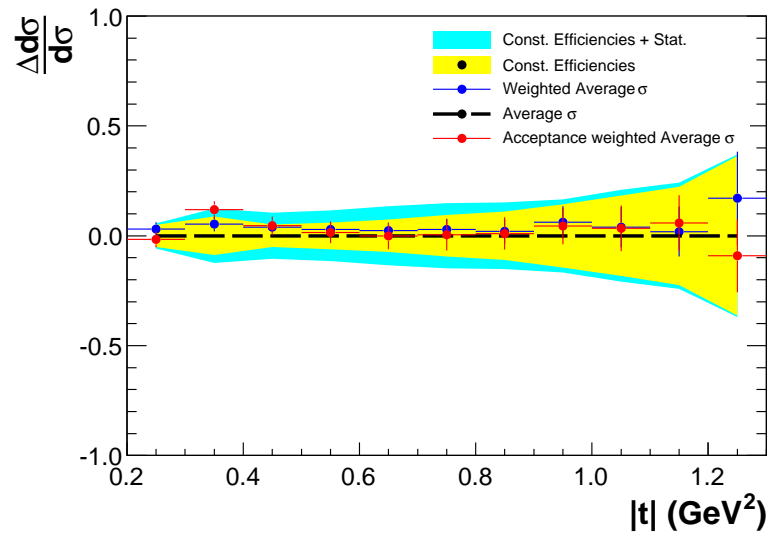


Figure 5.8. Deviation from the from the simple average and the acceptance weighted average for the single diffractive cross section.

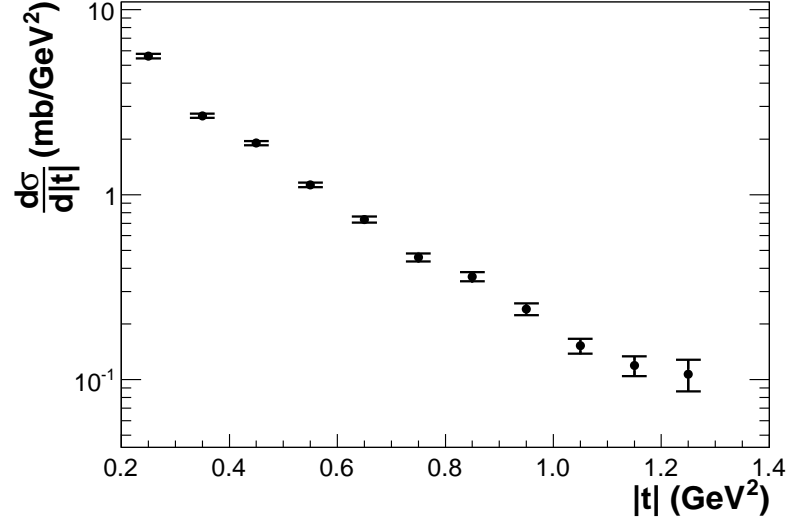


Figure 5.9. The single diffractive differential cross section including the statistical error and statistical errors from the trigger efficiency calculations which are a part of the systematic uncertainty.

- Calculation of Acceptance (choice of ansatz function)
- Beam smearing.

From the above list, the luminosity measurement, luminosity monitor efficiencies, and the fraction of diffractive events hitting the luminosity monitor add an overall normalization uncertainty that is fixed for all  $|t|$  bins.

Table 5.6. Systematic uncertainties from the constant factors

Syst. source	Value( $X$ )	$\frac{\delta X}{X}$
Luminosity	$12.6 \pm 1.6 \text{ nb}^{-1}$	0.126
LM efficiency(N)	0.968	0.004
LM efficiency(S)	0.935	0.004
LM acceptance	0.218	0.006
Total Const. Syst.		0.126

In Table 5.6 it can be seen that the error due to the calculation of luminosity is the largest uncertainty, and the other error sources are negligible compared to it. In the case of LM efficiency, either the north side or the south side is added, but not both.

#### 5.1.2.1 Trigger Efficiency Systematic Uncertainty

In order to calculate the systematic uncertainty introduced by the trigger efficiencies, which have been calculated assuming that there is no  $|t|$  dependence of the efficiencies, the central values of the efficiency for each  $|t|$  bin is used to recalculate the single diffractive cross section. Figure 5.10 shows the cross section calculated using the bin-by-bin trigger efficiencies. The black dashed line shows the cross section calculated using the single values of the trigger efficiencies.

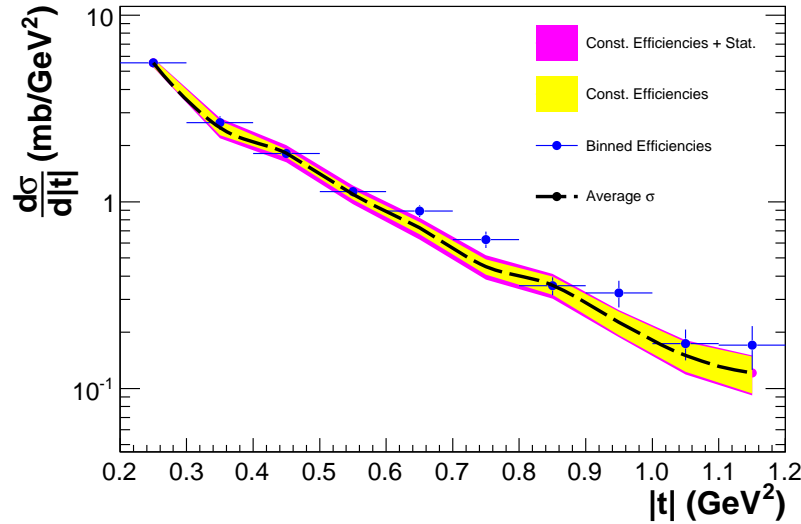


Figure 5.10. The single diffractive differential cross section calculated using bin-by-bin efficiencies, the dashed line show the mean cross section measurement.

Figure 5.11 shows the difference of the cross section from the mean cross section. Figure 5.12 shows the deviation of the cross section calculated from the bin by bin efficiencies from the mean cross section measurement.

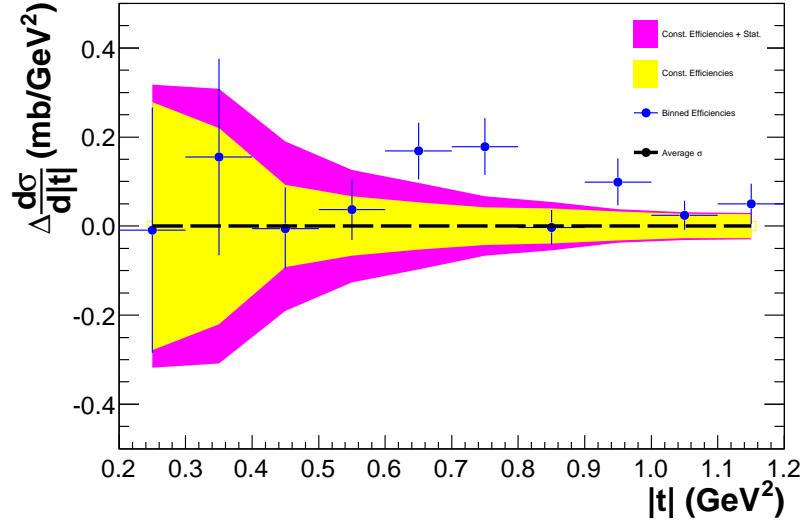


Figure 5.11. Difference between the differential cross section calculated using bin-by-bin efficiencies from the mean cross section.

It can be seen in Fig. 5.12 that by using bin by bin efficiencies, the cross section values are systematically higher for  $|t| > 0.6$ . The additional uncertainty due to the trigger efficiencies are obtained by taking the weighted average of the bin-by-bin deviation. This extra systematic uncertainty is shown in Fig. 5.12 by the blue dashed line and is equal to 0.05 (5%).

#### 5.1.2.2 Ansatz function systematics

To calculate the acceptance of the spectrometers an ansatz function is used; this function has the form  $e^{(-4.02|t|)}$ . In order to evaluate the systematics introduced due to the choice of the ansatz function the slope of the function is varied by 1.0 GeV

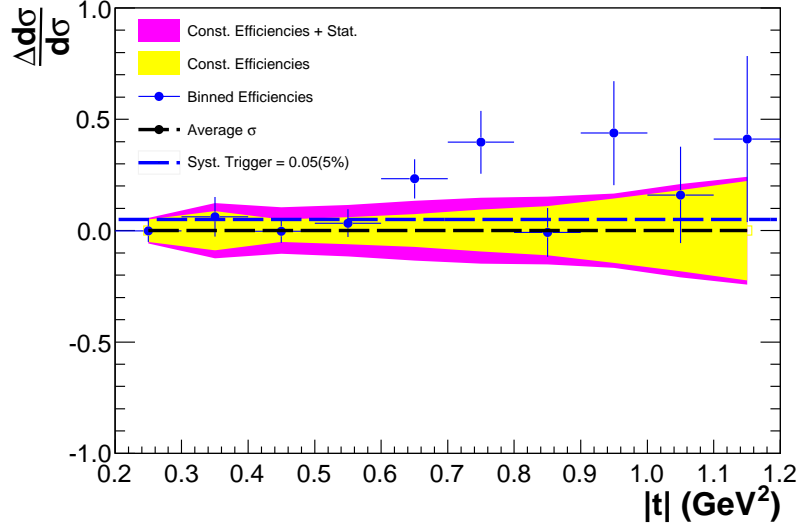


Figure 5.12. Deviation of the differential cross section calculated using bin-by-bin efficiencies from the mean cross section.

on either side and new acceptance functions are calculated. The variation of slope by 1.0 GeV is an overestimate, but is useful to demonstrate the effects on the final cross section measurements.

Figure 5.13 shows the cross section calculated by using the ansatz function  $e^{(-5.00|t|)}$  and  $e^{(-3.00|t|)}$ ; the dashed line shows the cross section using the ansatz function  $e^{(-4.02|t|)}$ .

Figures 5.14 and 5.15 show the difference and deviation from the mean cross section measurement. It can be seen that the cross section values from the different ansatz functions are well within the statistical error of the mean cross section. The deviations are negligible compared to the systematics for the luminosity measurement. No additional systematics are needed to account for the choice of the ansatz function.

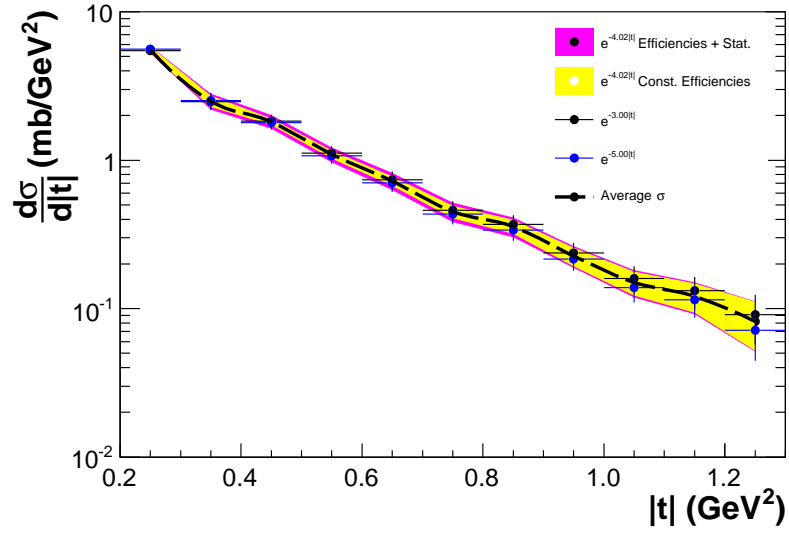


Figure 5.13. The single diffractive differential cross section obtained using different ansatz functions.

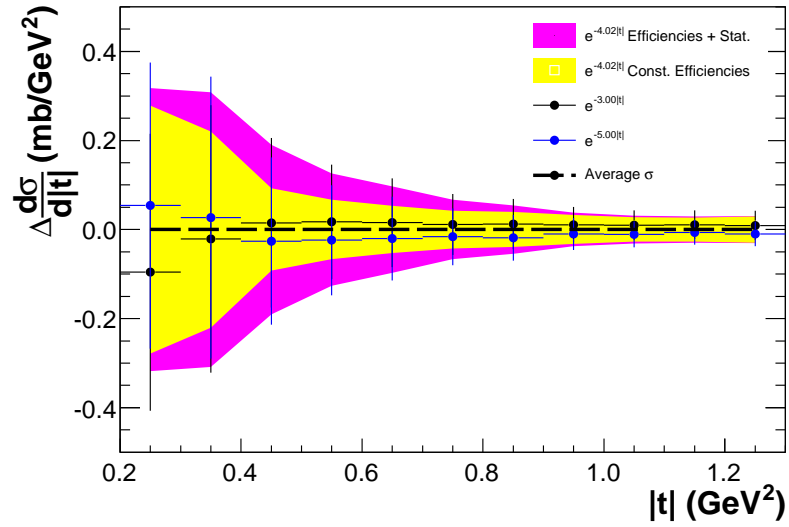


Figure 5.14. Difference between the single diffractive differential cross section obtained using different ansatz functions from the mean.

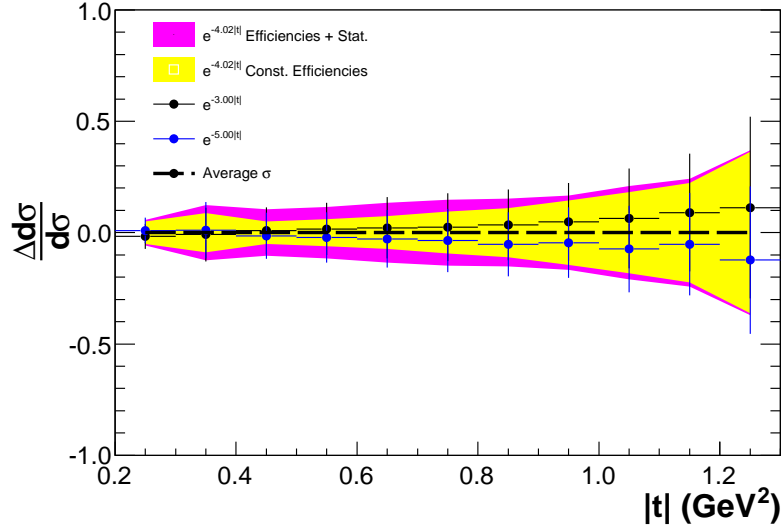


Figure 5.15. Deviation of the single diffractive differential cross section obtained using different ansatz functions from the mean.

#### 5.1.2.3 Beam smearing systematics

The standard cross section calculation includes the z-vertex uncertainty in the acceptance correction. To investigate the effects of the vertex smearing, the cross sections are calculated using the un-smear z-vertex acceptance. Figure 5.16 shows the cross sections using the un-smear acceptances.

Figure 5.17 shows the difference between the smeared and un-smear cross sections, it can be seen that beam smearing does not introduce any new systematic uncertainty.

#### 5.1.2.4 Total systematic uncertainties

The total systematic uncertainties are calculated using the method described in the previous sections. Table 5.3 lists the contributions from the different sources of systematic uncertainties.



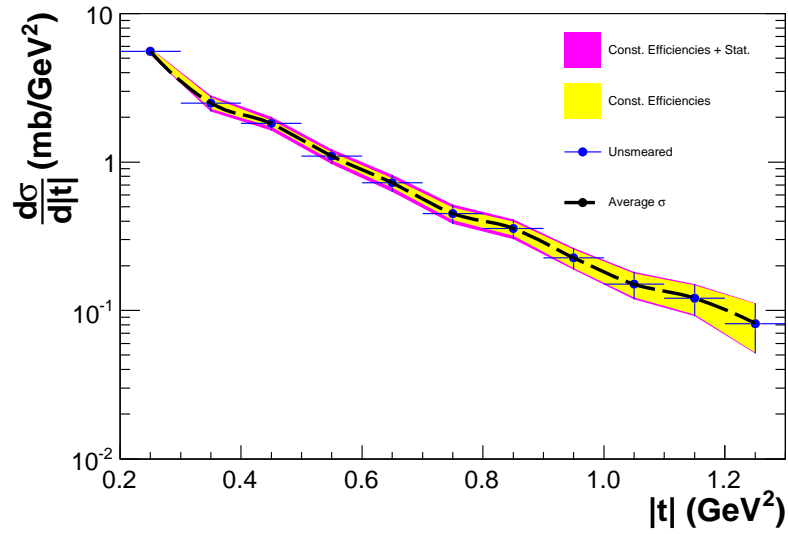


Figure 5.16. The single diffractive differential cross section using un-smeared z-vertex acceptance. The dashed lines shows the mean cross section obtained by using a smeared vertex to calculate the acceptance.

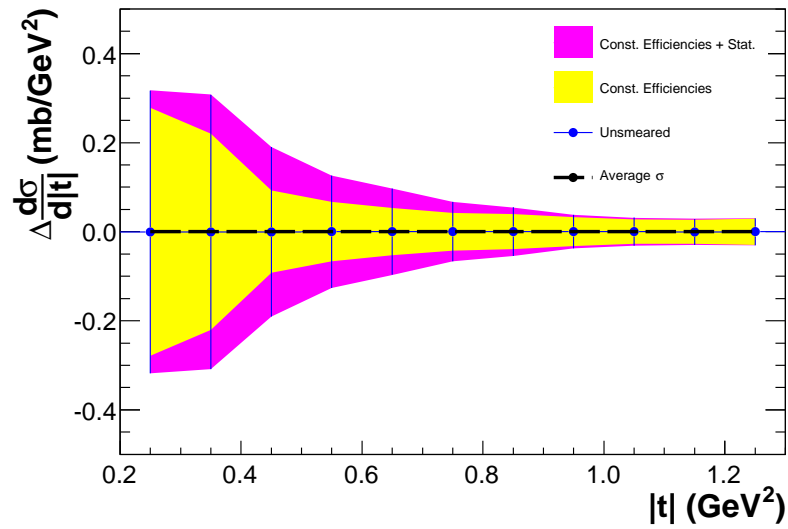


Figure 5.17. Difference between the single diffractive differential cross section using an un-smeared z-vertex acceptance and the mean.

Table 5.7. Total systematic uncertainties for the single diffractive cross section measurement

Syst. source	Value( $X$ )	$\frac{\delta X}{X}$
Luminosity	$12.6 \pm 1.6 \text{ nb}^{-1}$	0.126
LM efficiency(N)	0.968	0.004
LM efficiency(S)	0.935	0.004
LM acceptance	0.218	0.006
Trigger efficiencies (syst.)		0.050
Trigger efficiencies (stat.)		bin-wise

### 5.1.3 Single diffractive differential cross section

Figure 5.18 shows the single diffractive differential cross section including the statistical and systematic errors. The closed error bars represent the statistical errors and the open error bars show the systematic errors. The systematic errors are asymmetric because of the systematics of the trigger efficiencies.

The shaded region in the differential cross section plot, Fig. 5.18 shows the systematic uncertainty in the normalization of the differential cross section.

## 5.2 Total single diffractive cross section

To calculate the total single diffractive cross section ( $\sigma_{sd}$ ), the first step is to fit the differential cross section distribution. The fit function is motivated by the UA4 fitting functions [62] of the form  $A \cdot e^{(B \cdot |t| + C \cdot |t|^2)}$ . Figure 5.19 shows the fit to the single diffractive differential cross section using the above mentioned equation. Using the values of the fitted parameters the total single diffractive cross section in the range  $0.2 < |t| < 1.3$  is given by

$$\sigma_{sd} (0.2 < |t| < 1.3) = 1.347 \pm 0.044 \text{ (stat.)} \pm 0.169 \text{ (syst.) mb}$$

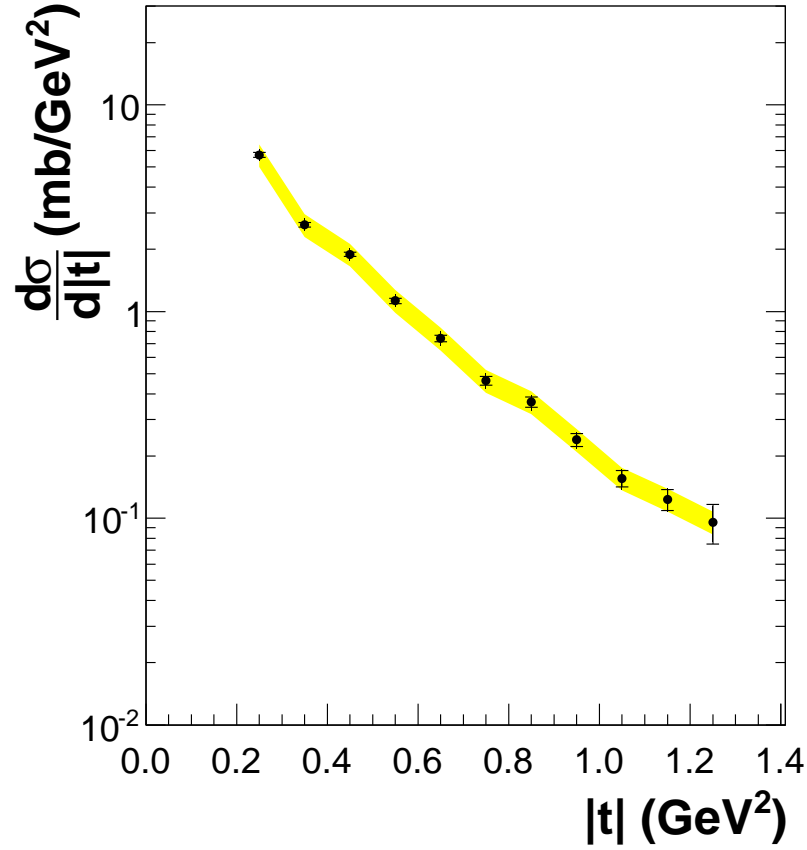


Figure 5.18. Single diffractive differential cross section  $\frac{d\sigma_{sd}}{d|t|}$  including the statistical and systematic errors.

Note that this is the single-sided cross section (average of proton and anti-proton spectrometers); the total single diffractive cross section (double-sided) is twice the single-sided cross section.

Figure 5.20 shows a single exponential ( $A \cdot e^{(B \cdot |t|)}$ ) fit to the data. It can be seen that seen from the  $\chi^2/NDF$  that the experimental data is not well-described by a single exponential function.

In order to evaluate the single diffractive cross section for  $|t| < 1.3$  GeV<sup>2</sup> the fitted function from the data is extrapolated to  $|t| = 0$ . Figure 5.21 shows the fitted

Table 5.8. Table of single diffractive differential cross section values after performing a weighted average; the statistical and bin by bin systematic errors are given. In addition to the systematic errors there is a addition uncertainty 12.6% in the normalization

$ t (\text{ GeV}^2)$	$\sigma(\text{mb/GeV})$	Error (stat.)	Error (syst.)
0.25	5.721	0.174	0.310
0.35	2.628	0.081	0.165
0.45	1.890	0.045	0.122
0.55	1.127	0.033	0.075
0.65	0.741	0.027	0.053
0.75	0.463	0.021	0.033
0.85	0.365	0.020	0.025
0.95	0.239	0.017	0.015
1.05	0.156	0.014	0.011
1.15	0.123	0.014	0.008
1.25	0.096	0.018	0.006

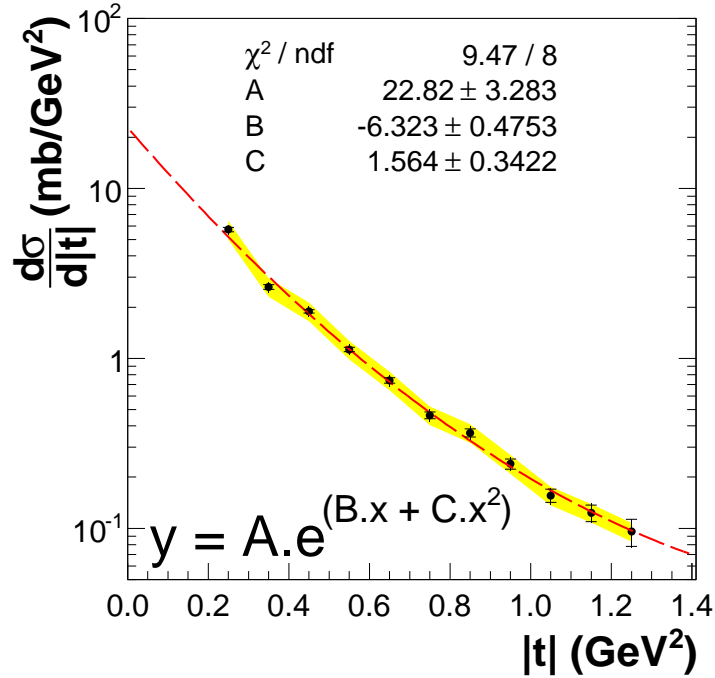


Figure 5.19. Single diffractive differential cross section  $\frac{d\sigma_{sd}}{d|t|}$  fitted to a function  $A \cdot e^{(B \cdot |t| + C \cdot |t|^2)}$ .

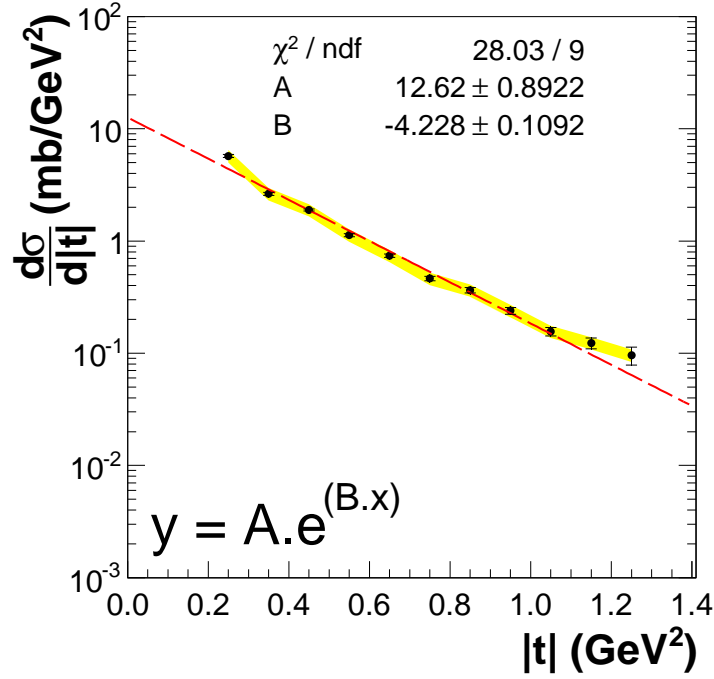


Figure 5.20. Single diffractive differential cross section  $\frac{d\sigma_{sd}}{d|t|}$  fitted to a simple exponential function  $A \cdot e^{(B \cdot |t|)}$ .

differential cross section extrapolated to zero. It can be seen that for  $|t| < 0.2 \text{ GeV}^2$  there are no experimental data points. Extrapolation of the non-linear function will thus have significant uncertainty. The figure shows the extrapolation and the low  $|t|$  data points from the UA4 experiment. Since it is implied from Goulianos's renormalization that the single diffractive cross sections are similar for 1.96 TeV and 546 GeV, the extrapolation appears to underestimate the true value. Integrating the fit function from  $|t|=0.0$  to  $1.3 \text{ GeV}^2$  the single diffractive cross section for the single side is given as

$$\sigma_{sd}(0.0 < |t| < 1.3) = 3.975 \pm 0.324 \text{ (stat.)} \pm 0.501 \text{ (syst.) mb}$$

To have a better estimate of the cross section from  $|t|=0.0$  to  $1.3 \text{ GeV}^2$ , the UA4 low  $|t|$  data points are included in the fit  $(A \cdot e^{(B \cdot |t| + C \cdot |t|^2)})$ . To combine the data

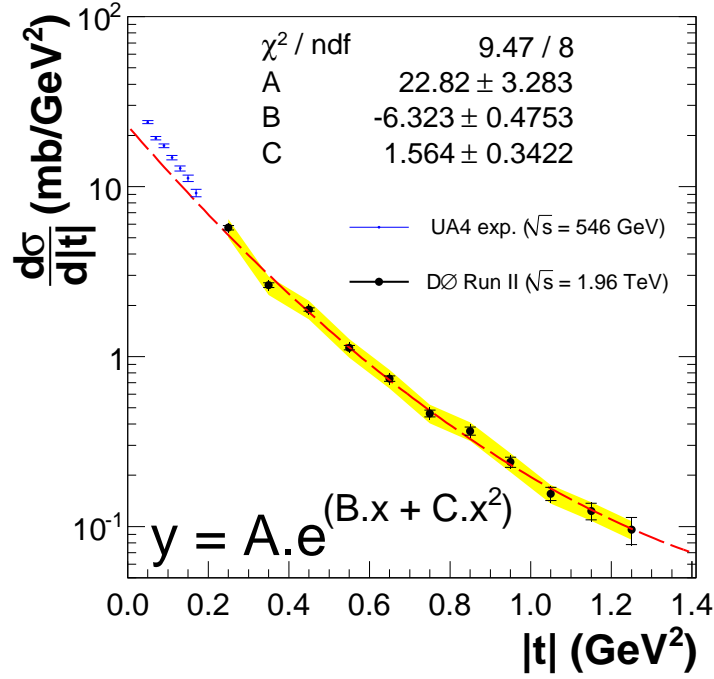


Figure 5.21.  $A \cdot e^{(B \cdot |t| + C \cdot |t|^2)}$  fit to the single diffractive differential cross section  $\frac{d\sigma_{sd}}{d|t|}$  showing the UA4 data points at low  $|t|$ .

samples requires inclusion of the normalization uncertainty of the DØ data in addition to the statistical and bin-by-bin systematic errors. To include the normalization shift in the fitting of the data, the mean values of the DØ data are shifted within the range of  $\pm 12.6\%$  (Normalization uncertainty) in increments of  $\pm 1\%$ . The DØ data are then combined with the UA4 data and are fitted to the function  $A \cdot e^{(B \cdot |t| + C \cdot |t|^2)}$ . Figure 5.22 shows the variation of  $\chi^2/NDF$  of the fit as a function of the normalization shift. The minimum value of  $\chi^2/NDF$  is the best fit line. Figure 5.23 shows the fitting results after including the UA4 data points. The total cross section using this fit is given as

$$\sigma_{sd}(0.0 < |t| < 1.3) = 4.841 \pm 0.048 \text{ (stat.)} \pm 0.609 \text{ (syst.) mb}$$

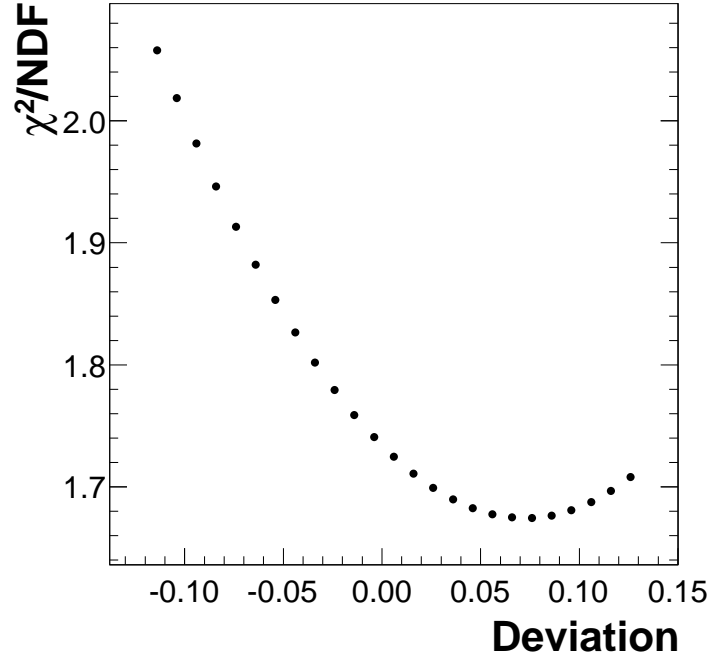


Figure 5.22. Variation of  $\chi^2/NDF$  as a function of variation of normalization for the DØ data points to include the UA4 data in the fit. The fit function used here is  $A \cdot e^{(B \cdot |t| + C \cdot |t|^2)}$ .

Table 5.9 shows the total single diffractive cross section, which is twice the single side cross section as the proton and anti-proton cross sections are symmetric.

### 5.3 Comparison with theory

Figure 5.24 shows the theoretical single diffractive cross section along with measurements from various experiments. It can be seen that the single diffractive cross section does not vary significantly with  $\sqrt{s}$  [30]. Figure 5.23 shows the comparison of the DØ single diffractive differential cross section with measurements from the UA4 and UA8 experiments. Table 5.10 lists the total single diffractive cross section calculated in various experiment at different center of mass energy collisions. The results from DØ are consistent with expectations.

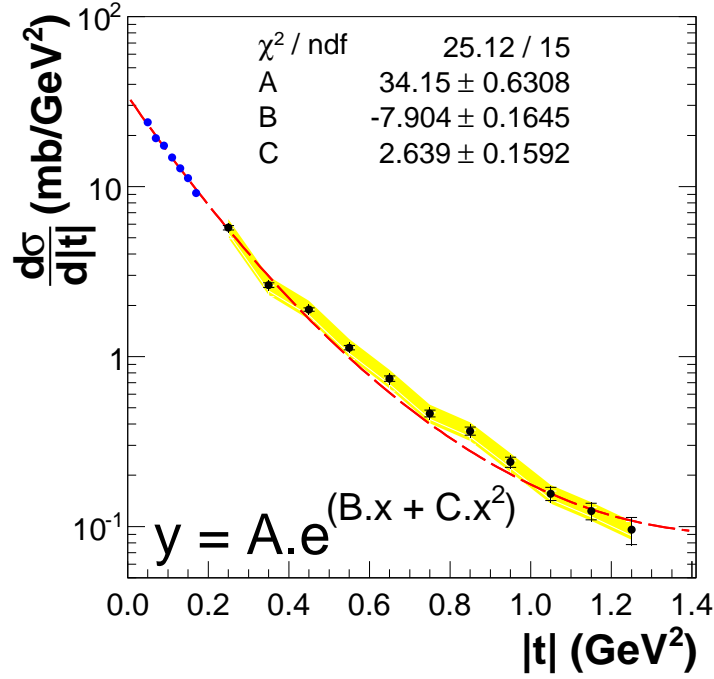


Figure 5.23. Fit for the single diffractive differential cross section  $\frac{d\sigma_{sd}}{d|t|}$  from DØ including the UA4 low  $|t|$  data, the fit line corresponds to the minimum  $\chi^2/NDF$  of the fit.

#### 5.4 Conclusions

In this dissertation I have presented a measurement the single diffractive differential cross section  $\left(\frac{d\sigma}{d|t|}\right)$  at  $\sqrt{s} = 1.96$  TeV center-of-mass energy for the first time. The single diffractive events were selected using the DØ central detector and the Forward Proton Detectors. The  $|t|$  of the forward protons were measured using the FPD system. The analysis presents the measurement of the differential cross section of the single diffractive events as a function of  $|t|$  in the range  $0.2 < |t| < 1.3 \text{ GeV}^2$ . The differential cross section measurement is in general agreement with theoretical and experimental expectations.



Table 5.9. Total single diffractive cross section ( $\sigma_{sd}$ ) calculated using different methods

Calc. method	$ t $ range	Total $\sigma_{sd}$
DØ Data fit	0.2 - 1.3	$2.694 \pm 0.044$ (stat.) $\pm 0.338$ (syst.) mb
DØ Data fit + extrapolation	0.0 - 1.3	$7.950 \pm 0.324$ (stat.) $\pm 1.007$ (syst.) mb
DØ Data + UA4 Data fit	0.0 - 1.3	$9.681 \pm 0.048$ (stat.) $\pm 1.219$ (syst.) mb

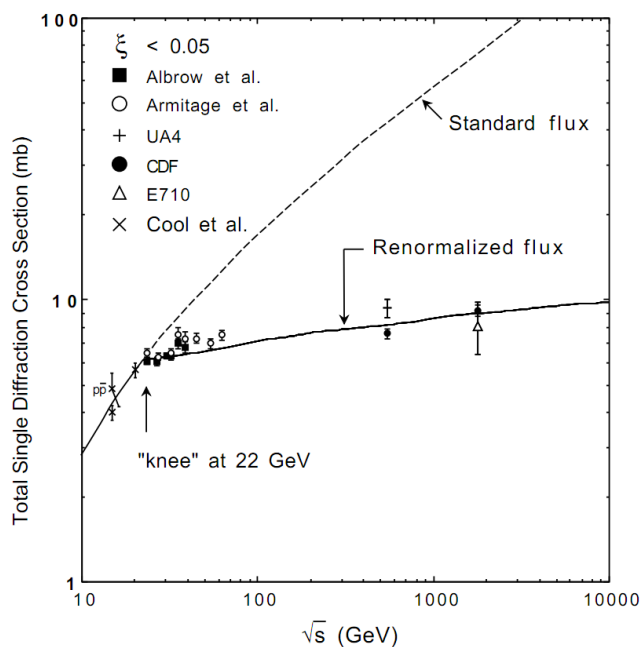


Figure 5.24. Single diffractive cross section as a function of  $\sqrt{s}$ , theory and different experimental results.

Table 5.10. Total single diffractive cross section ( $\sigma_{sd}$ ) measured in different experiments

Experiment	$\sqrt{s}$	$\sigma_{sd}$
UA4	546 GeV	$9.4 \pm 0.7$ mb
CDF	546 GeV	$7.89 \pm 0.33$ mb
E710	1.8 TeV	$8.1 \pm 1.7$ mb
CDF	1.8 TeV	$9.46 \pm 0.44$ mb
DØ Data fit + extrapolation	1.96 TeV	$7.950 \pm 0.324$ (stat.) $\pm 1.007$ (syst.) mb
DØ + UA4	1.96 TeV	$9.681 \pm 0.048$ (stat.) $\pm 1.219$ (syst.) mb

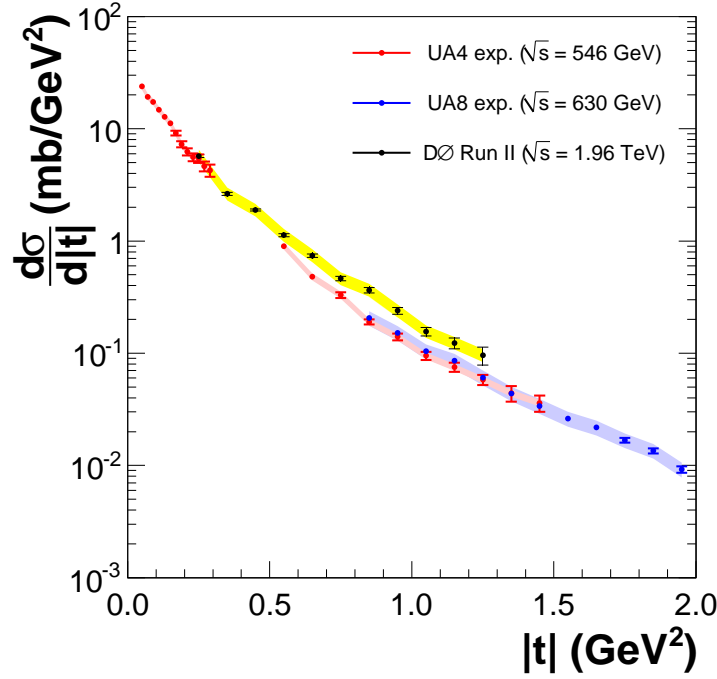


Figure 5.25. Single diffractive differential cross section  $\frac{d\sigma_{sd}}{d|t|}$  compared with the UA4 and UA8 results.

We have compared our measurement to previous measurements at lower center of mass energy by UA4 ( $\sqrt{s}=546$  GeV) and UA8 ( $\sqrt{s}=630$  GeV). There is good agreement with the low  $|t|$  UA4 data, although our data has a somewhat higher cross section at high  $|t|$ . In order to compare the absolute normalization of our data to the other experiments, we have made a PYTHIA Monte Carlo correction to account for the fact that the “high mass” single diffractive event requirement only captures a part (21% of the total cross section) due to the Luminosity Monitor cut, which puts an effective cut of  $M_X > 11.6$  GeV. The total single diffraction cross section in the region  $0.2 < |t| < 1.3 \text{ GeV}^2$  corrected for  $M_X > 0$  gives  $2.694 \pm 0.044(\text{stat.}) \pm 0.338(\text{syst.})$  mb. Extrapolating to  $|t| = 0$  gives a cross section of  $7.950 \pm 0.324$  (stat.)  $\pm 1.007$  (syst.) mb.

APPENDIX A  
EXCLUSIVE  $H^0$  AT ATLAS FPD

### A.1 Central exclusive process

In this document we present a feasibility study of the possibility of observing the standard model Higgs boson ( $H^0$ ) at the LHC using the proposed FP420 and FP220 (Forward Proton Detectors) in the central exclusive production (CEP) channel. We have considered two decay channels  $H^0 \rightarrow b\bar{b}$  for a light Higgs ( $M_H = 120$  GeV) and  $H^0 \rightarrow WW^*$  for a heavier Higgs ( $M_H = 160$  GeV). Central exclusive production refers to the process  $pp \rightarrow p + \phi + p$ , where the '+' sign indicates the presence of large rapidity gap between the two intact outgoing protons and  $\phi$  is the decay products of the central system that is produced. Thus the final state only consists of two outgoing protons and the decay products of the central system. The two outgoing proton would be detected in the forward proton detectors at either 220 m or 420 m depending on their momentum loss. The decay products of the central system would be detected in the main ATLAS detector. Rapidity gaps generally not required because of the large number of minimum bias pile-up events, which would likely fill the forward/backward rapidity intervals with particles. This does not affect the ability of the proton detectors to tag the outgoing protons. In this note we study Higgs production, but note that these proton detectors allow study of many other exclusive processes, both within and beyond the standard model [63, 64].

There are several reasons why the central exclusive process is attractive for the study of new physics, despite the large reduction in signal cross section compared to traditional production mechanisms. Since the outgoing protons are intact and scatter only through small angles, to a very good approximation the primary di-gluon system is in  $J_Z = 0$ ,  $C$ -even and  $P$ -even state [65], where  $J_Z = 0$  is the projection of the proton's angular momentum along the beam axis. This permits the determination of the quantum numbers for the CEP Higgs boson, which is predominantly in  $0^{++}$  state. The mass of the central resonance can be precisely (with a resolution of 2 to

3 GeV) determined from the momentum loss of the outgoing protons, irrespective of the decay channel of the central system. Finally a competitive signal to background ratio may be achievable [66, 67, 68, 69, 63].

The primary purpose of this document is to evaluate the pile-up background which arises when a non-diffractive hard scattering event providing a similar signature to a Higgs decay occurs in the same bunch crossing with another event or events that yield two outgoing protons. At typical LHC operating luminosities pileup backgrounds can become quite large, threatening the usefulness of the CEP process.

In the following sections we discussed the potential of the FP420 and FP220 detectors to observe a CEP-produced standard model Higgs boson, which could contribute to the discovery of the Higgs and/or the measurement of its properties (mass, quantum numbers). One of the main goals of the forward detectors is to exploit the  $b\bar{b}$  decay channel. This channel is not generally considered at the LHC due to overwhelming backgrounds. In the subsequent sections we provide a brief overview of the theoretical predictions and a survey of the uncertainties of the expected cross sections. We consider a Higgs mass of 120 GeV in the case of the  $b\bar{b}$  decay channel. We then apply a set of new exclusivity variables, described below to exploit the unique characteristics of the CEP signature. The suppression of the  $b\bar{b}$  background due to the  $J_Z = 0$  selection rule and the superior mass resolution of the forward proton detectors allow us to take advantage the large branching ratio of the  $b\bar{b}$  decay channel.

We next consider the decay channel  $H^0 \rightarrow WW^*$  with  $M_H = 160$  GeV (where the cross section of this channel is near its maximum), where one of the  $W$  is has an off-shell mass. We have applied similar exclusivity variables to those used in the  $b\bar{b}$  decay channel, but had to develop some new variables for the  $WW^*$  channel.

In addition to the potential for the discovery of the SM Higgs boson, the FP420 and FP220 provide attractive prospects for the MSSM and NMSSM scenarios. The FP420 program also has the ability to probe the CP-structure of Higgs sector by measuring the azimuthal asymmetry of the outgoing tagged protons or by studying the correlation between the decay products.

## A.2 Missing Mass Method

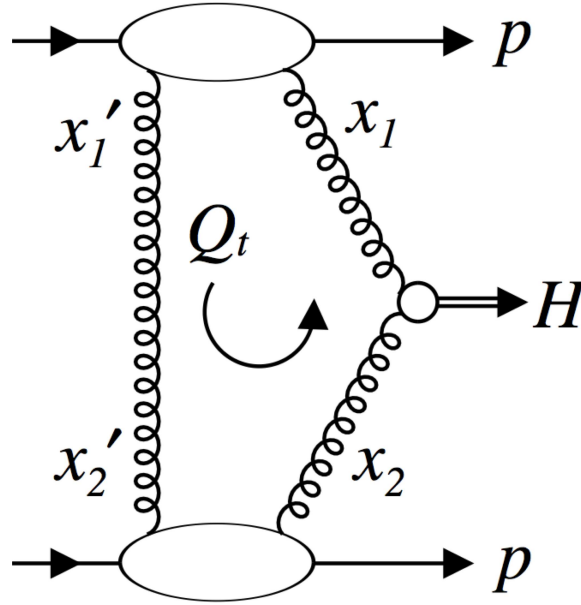


Figure A.1. Diagram for the the production of Central Exclusive Higgs, Gluon is exchanged between the protons which conserves the color and the the proton stays intact in the final state. The process can be written as  $pp \rightarrow p + H^0 + p$ .

Figure A.1 shows the Feynman diagram for the Higgs via the central exclusive mechanism. The outgoing protons in the final state remain intact and can be tagged using the forward proton detectors. Their momentum and collision vertex can be measured. The decay products are measured in the central detector. Since the process is central exclusive there are no other particles in the final state from the hard scatter.

Here the Missing Mass method [70] has been used to reconstruct the Higgs mass using the Forward Proton Detectors (FPD). The protons that are deflected at small angles with a sufficient momentum loss are detected by the Forward Proton Detectors located at 220 m or 420 m upstream and downstream of the ATLAS detector.

$$\xi_1 = \frac{\Delta p_1}{p_1}, \xi_2 = \frac{\Delta p_2}{p_2}$$

and the reconstructed mass of the central system is then

$$\Delta M = \sqrt{\xi_1 \xi_2 s}$$

where  $\sqrt{s} = 14$  GeV, the center of mass collision energy. For example a 1% loss in the fractional momentum of the protons gives a central system of 140 GeV. The mass resolution of the Higgs depends only of the resolution of  $\xi_1$  and  $\xi_2$ , which is expected to be in the 2 to 3 GeV range, far superior to that obtainable using the decay products in the central detector.

## APPENDIX B

### EXCLUSIVE $H^0 \rightarrow b\bar{b}$ AT ATLAS FPD



### B.1 $H^0 \rightarrow b\bar{b}$ Decay Channel

In the case of the  $H_0 \rightarrow b\bar{b}$  decay channel we consider a 120 GeV Higgs mass. We note that in this mass range, we only have acceptance using the 420 m detectors. The cross section times branching ratio for the Exclusive Higgs  $pp \rightarrow p + H_0 + p$  for a 120 GeV mass was predicted to be  $3 \times 0.6 = 1.86$  fb. The cut efficiencies must be included in order to get a correct estimate of the effective cross section. The signal signature is

- Two final state protons detected in the 420 m forward proton detectors
- Two back-to-back  $b$  jets in the central detector
- Very little other activity in the detector outside the  $b$ -jet cones

Potentially the most serious background for this channel is pile-up background consisting of inclusive  $b\bar{b}$  production combined with two single diffractive protons from other proton-proton interactions in the same bunch crossing. The cross section for  $gg \rightarrow b\bar{b}$  is 500  $\mu\text{b}$ . There is a  $p_T$  cut at the generator level of 25 GeV so that the effective cross section is about 7.5  $\mu\text{b}$ .

The primary challenge in this decay channel is the suppression of this background. This has been estimated to be the largest background at the LHC because of the large number interactions in each bunch crossing at high luminosity. The cross section for pileup events is given by the following expression:

$$\sigma_{\text{eff}} = N(N-1)P_i^2 Q \sigma_{b\bar{b}}$$

where  $\sigma_{\text{eff}}$  is the cross section for the pile up events,  $N$  is the number of minimum bias events (a luminosity dependent number,  $N \sim 35$  at full luminosity).  $Q$  is the rejection factor obtained using precision timing to reject events where the timing vertex is inconsistent with the central silicon vertex ( $Q=0.025$ ) [71],  $P_i$  is the probability of an

interaction giving a proton in the proton detector acceptance ( $P_i=0.012$  for 420 m detectors) and  $\sigma_{b\bar{b}}$  is the input cross section for the hard scattering. \*\*\*Andy says 4 should not be included since it is already incorporated in the 0.012 factor

The largest non-pileup background is the exclusive production of  $gg \rightarrow b\bar{b}$ ; this is an irreducible background because this is an exclusive process and thus yields  $b$  jets and correlated final state protons. This process is suppressed by the P-even  $J_z = 0$  selection rule [72], but with an estimated cross section of  $500 \text{ fb}^{-1}$  could still contribute if the pile-up background can be sufficiently suppressed. We do not consider this background here.

#### B.1.1 Monte Carlo

Exclusive Higgs events  $pp \rightarrow p + H^0 + p$  were generated using the EXHUME Monte Carlo generator [73] within the ATHENA framework. The  $b\bar{b}$  decay mode was chosen explicitly in the Monte Carlo ( $M_H = 120 \text{ GeV}$ ). The signal events were passed through the ATLFAST simulation, which is a parametrization of the full ATLAS detector simulation. The momentum fractions of the final state generation level protons from EXHUME were calculated, smeared with a Gaussian error of  $2 \text{ GeV}$  (corresponding to the resolution of the proton detectors) and added to the event.

For the pile-up background, the inclusive  $b\bar{b}$  background was generated using PYTHIA 6.4 [74] with a minimum transverse momentum,  $p_T > 25.0 \text{ GeV}$  and the default ATLAS tune. These events were also passed through the ATLFAST simulation. The fake protons for the pile up events were generated using a POMWIG proton parametrization function [75]. The parametrization function used was

$$\frac{d\sigma^{SD}}{\sigma_T \cdot dt \cdot dx_L} = 1.1483 \times 10^{-2} \cdot \xi^{-1.11}$$

The  $\xi_1$  and  $\xi_2$  obtained for each event from the above parametrization were added to the background events.

### B.1.2 Exclusivity variables

The following kinematic cuts on the  $b$ -jets were used to select jets consistent with Higgs boson decay:  $P_T^1 > 45$  GeV and  $P_T^2 > 30$  GeV,  $|\eta| > 2.5$ ,  $|\Delta\eta| > 1.0$ ,  $170^\circ > \Delta\phi > 190^\circ$ . The protons were required to be within the acceptance of the 420 m detectors:  $0.002 < (\xi_1, \xi_2) < 0.015$ .

We next introduce the following exclusivity variables to reduce the pileup background to manageable levels. The first two variables  $R_j$  and  $\Delta y$  demand kinematic consistency between the central system and the forward protons, while the latter two tracking variables ( $N_T$  and  $N_C$ ) take advantage of the non-exclusive nature of pileup backgrounds.

- Ratio of missing mass and dijet mass,  $R_j$

$$R_j = \frac{2}{\Delta M} p_T \cosh(\eta - y)$$

where  $y = 0.5 \ln \left( \frac{\xi_1}{\xi_2} \right)$  is the rapidity constructed from the proton detectors,  $\eta$  is pseudorapidity and  $p_T$  are the transverse energy of the leading jet,  $\Delta M$  is the missing mass from the proton detectors and  $\xi_1, \xi_2$  are the fractional momentum loss of the protons.  $R_j$  was found to be a slightly more robust variable than the more traditional  $R_{jj}$  which makes use of the leading two jets.

- Difference between rapidity of the protons and pseudorapidity of the jets,  $\Delta y$

$$\Delta y = 0.5 \ln \left( \frac{\xi_1}{\xi_2} \right) - 0.5(\eta_1 + \eta_2)$$

where  $\eta_1$  and  $\eta_2$  are the pseudo-rapidity of the first and the second  $b$  jets from the central detector.

- Number of tracks outside the jet cone,  $N_T$

$N_T$  is the number of tracks outside the cone of  $\Delta R = 0.7$  outside the  $b$  jets where  $\Delta R = \sqrt{(\Delta\eta)^2 + (\Delta\phi)^2}$ .

- Number of tracks outside the jet cone and  $60^\circ$  away from the  $b$  jets i.e.  $\Delta\phi > 60^\circ$ ,

$N_c$

where  $\Delta\phi$  is the angle between the  $b$  jet and a track.

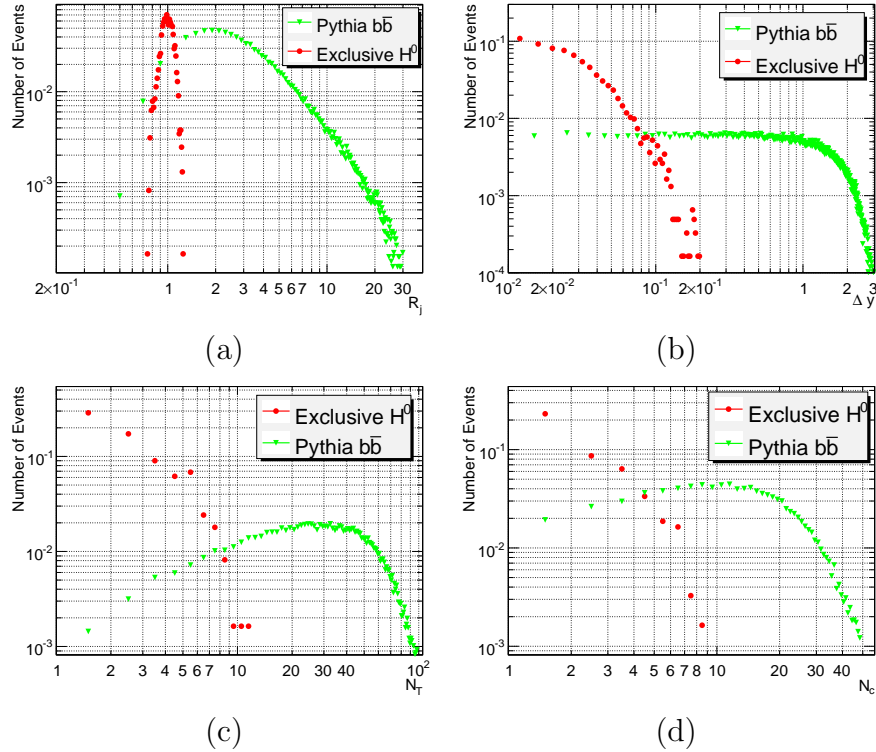


Figure B.1. Exclusive  $b\bar{b}$  signal (red points) compared with pileup background (green points) for (a)  $R_j$ , (b)  $\Delta y$ , (c)  $N_T$ , and (d)  $N_c$ .

Figure B.1 shows the distributions of the exclusivity variables for the signal and background samples. Figure B.1(a)–(b) show that  $R_j$  and  $\Delta y$ , respectively,

are sharply peaked in the case of exclusive signal events, whereas in the case of pileup events the distribution is much flatter due to the fact that the pileup protons are from random single diffractive events, not associated with the central system. Figure B.1(c)–(d) show the tracking variables which also show powerful discrimination between low multiplicity exclusive events and high multiplicity background events.

### B.1.3 Efficiencies of Cuts

Table B.1 shows the rejection and efficiency for the cuts used in this analysis. It should be noted that no trigger efficiency has been included; in order to retain a high trigger efficiency it will be necessary to have a reasonably low threshold dijet trigger at Level 1, and gain substantial rejection at Level 2 from the FP420 detectors. Discussions with experts indicate such a strategy is feasible. The kinematical cuts refers to the basic selection cuts listed in the previous section. For each cut, the table lists its individual value, efficiency, and rejection. The  $N_c$  and  $N_T$  cuts have both been applied as it is possible to make a tighter cut on the orthogonal region variable cut maintaining acceptable efficiency, and gain some rejection over the simple tracking variable. The events that pass the kinematic and exclusivity cuts are then subjected to a final cut on the mass window, which provides significant additional rejection, demonstrating the benefit of the superior mass resolution of the proton detectors.

### B.1.4 Results

Table B.2 shows the number of signal and background events, number of interactions, and significance for different luminosity scenarios and integrated luminosities. The luminosity used for the  $30 \text{ fb}^{-1}$  sample is  $10^{33} \text{ cm}^{-2} \text{ s}^{-1}$ ; for the  $60 \text{ fb}^{-1}$  sample the numbers are given for both  $1$  and  $2 \times 10^{33} \text{ cm}^{-2} \text{ s}^{-1}$  (to demonstrate the dramatic increase in pileup background with time); for the  $300 \text{ fb}^{-1}$  sample an instantaneous lu-

Variable	Cuts	$H^0$	$b\bar{b}$
Kinematic Cuts	(see text)	0.061	0.062
$R_j$	0.85 to 1.15	0.925	0.038
$\Delta y$	$< 0.1$	0.905	0.060
$N_c$	$< 2$	0.777	0.031
$N_T$	$< 4$	0.810	0.010
$N_c$ and $N_T$	2 and 4	0.734	0.008
$\Delta M_{420+420}$	118.3, 121.7 GeV	0.723	0.014

Table B.1. Individual efficiency and rejection of different selection variables applied in the  $H^0 \rightarrow b\bar{b}$  decay channel.

minosity of  $1 \times 10^{34} \text{ cm}^{-2} \text{ s}^{-1}$  is used. Only pileup background is shown here—although this dominates at high luminosity the contribution from other backgrounds warrant further study at low luminosity. By tightening the exclusivity cuts at high luminosity (and by getting smarter with experience), it may be possible to better control the backgrounds at high luminosity (although the trigger issues will become more difficult). It is clear that a Standard Model CEP Higgs to  $b\bar{b}$  will be extremely difficult to observe, however, there are several models, including popular SUSY MSSM models which predict a dramatic increase in the Higgs cross section, which could make this a viable channel for Higgs discovery as well as measurement of properties, such as mass and quantum numbers [76, 77].

$\mathcal{L}(\text{fb}^{-1})$	$H^0$ (Signal)	$N$	$b\bar{b}$	Significance
30	2.3	3.5	1.12	2.15
60	4.5	3.5	2.24	3.0
60	4.5	7	10.8	1.35
150	11	18	184	0.85
300	23	35	1520	0.6

Table B.2. Number of signal and background events, number of interactions, and significance for  $H^0 \rightarrow b\bar{b}$  decay channel.

## APPENDIX C

### EXCLUSIVE $H^0 \rightarrow WW^*$ AT ATLAS FPD

### C.1 $H^0 \rightarrow WW^*$ decay channel

For Higgs Bosons in the intermediate mass region  $\sim 160$  GeV, the  $H_0 \rightarrow WW^*$  decay channel dominates Higgs production as shown in Fig. C.1. The cross section for this channel at 160 GeV is 1.6 fb [78].

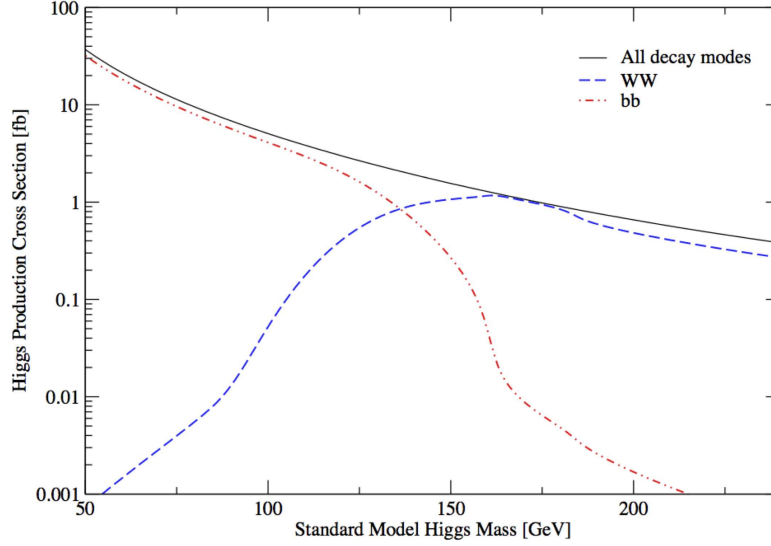


Figure C.1. Cross section times the Branching ratio for the production of Central Exclusive Higgs ( $pp \rightarrow p + H^0 + p$ ) in the  $WW^*$  and  $b\bar{b}$  decay channel. .

The  $W$  bosons produced from the Higgs decay will subsequently decay; Table C.1 lists the different decay modes and their branching ratios, where  $j$  is a jet and  $\ell$  is a lepton ( $e$ ,  $\mu$ , or  $\tau$ ). In this analysis we have primarily considered the

Table C.1. Branching ratios of the  $WW^*$  into the different possible decay channels.

Decay	Branching Ratio
$\mu\nu jj$	10.27%
$e\nu jj$	10.27%
$\tau\nu jj$	10.27%
$jjjj$	58.94%
$\ell\nu\ell\nu$	10.27%



semileptonic decay channel with a muon in the final state  $WW^* \rightarrow \mu\nu jj$ . The cross section  $\times$  branching ratio for this particular decay signature is thus 0.17 fb.

The leading order background for this process is  $W + 2j$  production with the  $W$  decaying in the semileptonic mode  $W \rightarrow \mu\nu$  along with two pileup protons. The cross section for  $W + 2j$  production is estimated to be 2.5 nb. The second leading background comes from the continuum  $WW^*$  production with the  $W$  bosons decaying in the same manner  $WW^* \rightarrow \mu\nu jj$ . The cross section for this process is given to be 181 pb. The pileup background is calculated in the same way as for the  $b\bar{b}$  case, but using the  $W$  backgrounds:

$$\sigma_{\text{eff}} = N(N-1)P_i^2 Q \sigma_{WW^*, W+2j}$$

the only difference is that the  $P_i$  factor depends on the proton detectors used, since both 220 m ( $P_i=0.03$ ) and 420 m ( $P_i=0.012$ ) detectors have acceptance.

### C.1.1 Monte Carlo

The events again generated using EXHUME Monte Carlo generator by selecting the  $H^0 \rightarrow WW^*$  decay channel, and passing the events through ATLfast. EXHUME does not allow the selection of a specific branching ratio—all final states are generated according to their branching ratio. As in the previous case the final state protons were smeared using a 2 GeV Gaussian resolution. For the backgrounds we used the official full detector simulation CSC data sets for  $W + 2j$  (generated with ALPGEN) and  $WW^*$  (generated with HERWIG):

- $W + 2j \rightarrow \text{alpgen.008228.AlpgenJimmyWmunuNp2VBFCut}$
- $WW^* \rightarrow \text{trig1_misal1_csc11.005985.WW_Herwig.recon.v12000601.}$

The pileup protons were handled in the same way as for the  $b\bar{b}$  case.

### C.1.2 Exclusivity variables

The following kinematical cuts were used for the  $WW^*$  analysis:  $p_T^{jet1} p_T^{jet2} > 25.0$  GeV and  $|\eta| < 3.2$ ;  $p_T^\mu > 20.0$  GeV and  $|\eta| < 2.5$ ;  $\cancel{E}_T > 25.0$  GeV. The kinematic variables for the  $WW^*$  case  $r_{cm}$  and  $\Delta y_{jj}$ , defined below, are similar to the  $b\bar{b}$  variables. We have determined that it is better to simply ignore the rapidity of the leptonic  $W$ , and use the rapidity of the hadronic  $W$  as an estimate of the Higgs rapidity, rather than trying to account for the neutrino ambiguity. We also developed a new variable  $\Delta y M$  which takes into account both the mass difference and the rapidity difference (it has a large correlation with the previous two variables). The two tracking variables ( $N_T$  and  $N_C$ ) are basically the same as in the  $b\bar{b}$  case, and are not defined again here.

- Ratio of cluster mass and missing mass,  $r_{cm}$

$$r_{cm} = \frac{m_c}{\Delta M}$$

Where  $m_c = \sqrt{p_T^2(jj\ell) + m_{jj\ell}^2} + \cancel{E}_T$ ,  $\Delta M$  is the missing mass measured at the FPDs and is given by  $\Delta M = \sqrt{\xi_1 \xi_2 s}$  and  $m_{jj\ell}^2$  is invariant mass of the di-jets and the lepton.

- Difference in the rapidity and pseudorapidity,  $\Delta y_{jj}$

$$\Delta y_{jj} = \left| \frac{1}{2}(\eta_{j1} + \eta_{j2}) - \frac{1}{2} \log \left\{ \frac{\xi_1}{\xi_2} \right\} \right|$$

where  $\frac{1}{2} \log \left\{ \frac{\xi_1}{\xi_2} \right\}$  is the rapidity measured by the proton detectors

- Combined variable of rapidity and mass difference,  $\Delta y M$

$$\Delta y M = \cosh^{-1} \left\{ \frac{\Delta M}{2(p_T^1 + p_T^2)} \right\} - 0.5(\eta^1 + \eta^2) + 0.5 \log \left\{ \frac{\xi_1}{\xi_2} \right\}$$

Figure C.2 shows the major exclusivity variables for signal and background in (a)  $r_{cm}$  (b)  $\Delta y_{jj}$ , (c)  $\Delta y_M$  and (d)  $N_T$ , clearly demonstrating the separation between the signal (red curve) and backgrounds (blue and green curves).

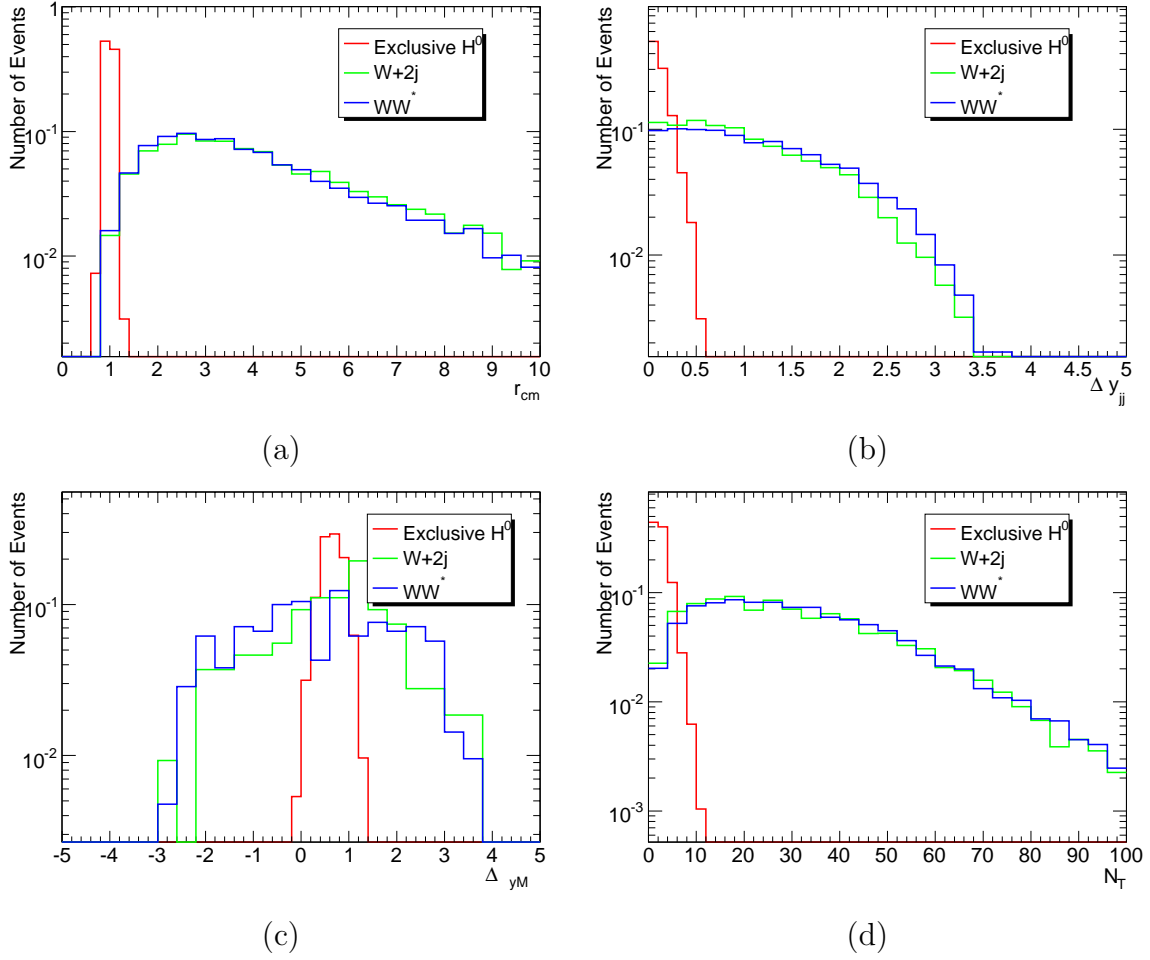


Figure C.2. CEP Higgs signal in  $WW^*$  channel (red line) compared with the  $W + 2j$  (green) and  $WW^*$  (blue) backgrounds for (a)  $r_{cm}$  (b)  $\Delta y_{jj}$   $\Delta y_M$  and (d)  $N_T$ .

### C.1.3 Efficiency of Cuts

Table C.2 lists the efficiency and rejection of each variable for the signal and both backgrounds. It can be seen that the  $R_{cm}$  variable gives a signal efficiency near

100% and a background rejection of  $\sim 100$  and  $\sim 50$  in the case of  $W + 2j$  and  $WW^*$  background. The cuts have been tuned to give the maximum signal efficiency and have not been optimized for background rejection. For example, the cut on the  $N_T$  variable at 8 is a very loose cut and as shown in Fig. C.2(d) a much higher background rejection can be achieved by making the cut tighter at higher luminosity, as needed.

Figure C.3 shows the mass window cut before and after the  $R_{cm}$  cut. It can be seen that the  $R_{cm}$  cut biases the mass window in the case of background, so the rejection factor listed in the Table C.3 is an overestimate. It can be seen from Fig. C.3 that the rejection is overestimated by a factor of  $\sim 10$ . To account for this the rejection for both the backgrounds is reduced by a factor of 10 in the estimates for total signal and background events. In the last line the roman pot acceptances for are listed or the signal events for combination of roman pots at 420+420m and 420+220m respectively.

Table C.2. Efficiency and rejection of different variables applied sequentially in the case of  $H^0 \rightarrow WW^* \rightarrow \mu\nu jj$  decay channel.

Variable	Cuts	$H^0$	$W + 2j$	$WW^*$
$R_{cm}$	0.6 to 1.3	1.0	0.020	0.025
$\Delta y_{jj}$	$< 0.4$	0.98	0.0045	0.0041
$\Delta y_M$	0 to 1.3	0.95	0.0032	0.0026
$N_T$	8	0.94	0.0003	0.0002
$\Delta M_{420+420}$	156.5 to 163.5 GeV	0.68	$2.9 \times 10^{-5}$	$1.5 \times 10^{-5}$
$\Delta M_{420+220}$	154.5 to 165.5 GeV	0.81	$4.6 \times 10^{-5}$	$2.5 \times 10^{-5}$
RP Acc.(420+420)	0.002 to 0.015	0.12	-	-
RP Acc. (220 + 420)	-	0.57	-	-

Table C.3 lists the total efficiencies of the signal and background events. The first line named as *Kinematicalcuts* + *BR* lists the efficiencies after the initial kinematical cuts listed in the event selection section multiplied by the branching ratio

Table C.3. Total efficiency for signal and background  $H^0 \rightarrow WW^*$  decay channel.

Cuts	$H^0$	$W + 2j$	$WW^*$
kinematical cuts + BR	0.01924	0.0313	0.1421
Exclusivity Cuts + $\Delta M(420 + 420)$	0.00175	$8.92 \times 10^{-7}$	$2.06 \times 10^{-6}$
Exclusivity Cuts + $\Delta M(420 + 220)$	0.0062	$1.43 \times 10^{-6}$	$3.59 \times 10^{-6}$

which is 10.41% in the case of the given channel. In the second line the signal and background efficiencies are given after the exclusivity cuts and the mass window cut for  $420 + 420m$  RPs after the correction factor of 10 that is discussed in the previous paragraph. The next line is for the case of  $420 + 220m$  RPs. Here by exclusivity cuts we mean that  $R_{cm}$ ,  $\Delta y_{jj}$ ,  $\Delta yM$  and  $N_T$  cuts put together.

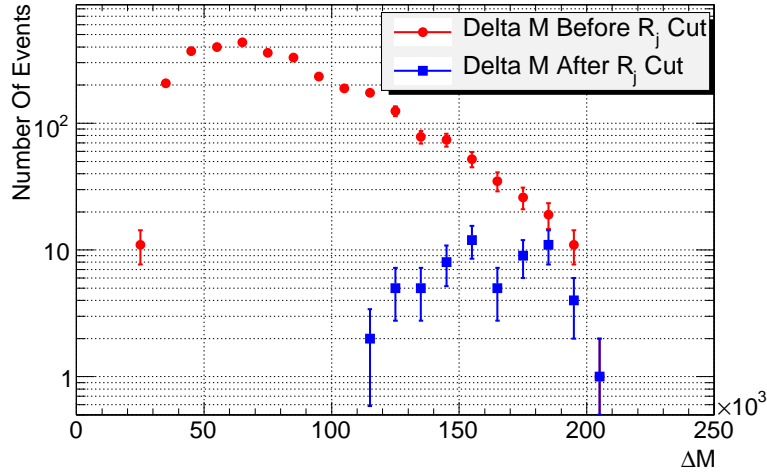


Figure C.3. Effect of  $R_{cm}$  cut on the  $\Delta M$  distribution of the background; the correlation between these cuts decreases the effectiveness of the Mass Window cut..

### C.1.4 Results

Table C.4 gives the expected number of signal events versus the number of background events at different luminosities for the two different backgrounds for RPs at  $420 + 420m$ . In Table C.4 the number  $N$  is the number of interactions, which depends on the instantaneous luminosity and factors into the pileup rate as discussed earlier. It can be seen that although the number of signal events is large compared to the background, showing the background is under control and justifying the loose cuts, the overall number of signal events is small. At higher luminosities the cuts can be made tighter to improve background rejection for the  $150\text{fb}^{-1}$  and  $300\text{fb}^{-1}$  luminosity cases.

Table C.4. Number of signal and background events and significance for RPs at  $420 + 420$  meters in  $H^0 \rightarrow WW^* \rightarrow \mu\nu jj$  decay channel.

$\mathcal{L}(\text{fb}^{-1})$	$H^0$ (Signal)	$N$	$W + 2j$	$WW^*$	Total BG	Significance
30	0.061	3.5	$2.8 \times 10^{-3}$	$3.5 \times 10^{-4}$	$3.15 \times 10^{-3}$	1.23
60	0.122	7	$2.0 \times 10^{-2}$	$3.4 \times 10^{-3}$	$2.34 \times 10^{-2}$	0.78
150	0.306	17.5	0.348	0.060	0.408	0.48
300	0.611	35	2.864	3.344	6.208	0.33

Table C.5 shows the same numbers as in table 5 but in the case when the RPs at  $420 + 220m$  is used instead of  $420 + 420m$ . It can be seen that there is a significant increase in the number of signal events. This is due to the fact that the RPs at  $420 + 220m$  have better acceptance for a Higgs of mass  $160\text{GeV}$ . But there is still scope to improve the signal to background ratio by optimizing the exclusivity cuts.

Table C.6 gives an estimate of the total number of signal events in all the decay channels that can be possibly seen at different luminosities. It is important to estimate the total number of signal events because of the low cross-section and

Table C.5. Number of Signal and background events for RPs at  $420 + 220$  meters in  $H^0 \rightarrow WW^* \rightarrow \mu\nu jj$  decay channel.

$\mathcal{L}(\text{fb}^{-1})$	$H^0$ (Signal)	$N$	$W + 2j$	$WW^*$	Total BG	Significance
30	0.217	3.5	0.160	0.028	0.188	0.498
60	0.433	7	1.536	0.280	1.816	0.321
150	1.083	17.5	26.44	4.820	31.26	0.193
300	2.165	35	217.936	39.73	257.67	0.134

low number of signal events in this channel. Including all the decay channels in the  $420 + 420m$  and the  $420 + 220m$  along with the signal efficiencies give a considerable amount of signal events.

Table C.6. Total Number of Signal events in  $H^0 \rightarrow WW^*$  channel for the Forward Proton detectors at  $420 + 420m$

$\mathcal{L}(\text{fb}^{-1})$	$\mu\nu jj$	$e\nu jj$	$e\nu e\nu$	$\mu\nu\mu\nu$	$\mu\nu e\nu$	Total
30	0.099	0.102	0.066	0.061	0.125	0.452
60	0.198	0.203	0.131	0.122	0.249	0.904
150	0.496	0.507	0.328	0.306	0.623	2.261
300	0.992	1.016	0.655	0.612	1.246	4.521

Table C.7. Efficiency and rejection of different variables applied sequentially in the case of  $H^0 \rightarrow WW^* \rightarrow \mu\nu jj$  decay channel after cuts were made tighter.

Variable	Cuts	$H^0$	$W + 2j$	$WW^*$
$R_{cm}$	0.6 to 1.1	0.948	0.020	0.025
$\Delta y_{jj}$	$< 0.2$	0.753	0.0045	0.0041
$\Delta y_M$	0 to 1.0	0.708	0.0032	0.0026
$N_T$	4	0.583	0.0003	0.0002
$\Delta M_{420+420}$	156.5 to 163.5 GeV	0.476	$2.9 \times 10^{-5}$	$1.5 \times 10^{-5}$
$\Delta M_{420+220}$	154.5 to 165.5 GeV	0.496	$4.6 \times 10^{-5}$	$2.5 \times 10^{-5}$
RP Acc.(420+420)	0.002 to 0.015	0.089	-	-
RP Acc. (220 + 420)	-	0.250	-	-



## REFERENCES

- [1] C. Avila and M. E. Pol, “Measurement of the elastic differential cross section in  $p\bar{p}$  scattering at  $\sqrt{s}=1.96$  TeV,” d0-NOTE-6056.
- [2] M. K. Gaillard, P. D. Grannis, and F. J. Sciulli, “The standard model of particle physics,” *Rev. Mod. Phys.*, vol. 71, pp. S96–S111, 1999.
- [3] S. Weinberg, “A model of leptons,” *Phys. Rev. Lett.*, vol. 19, no. 21, pp. 1264–1266, Nov 1967.
- [4] D. J. Gross and F. Wilczek, “Asymptotically free gauge theories. i,” *Phys. Rev. D*, vol. 8, no. 10, pp. 3633–3652, Nov 1973.
- [5] Y. Fukuda *et al.*, “Evidence for oscillation of atmospheric neutrinos,” *Phys. Rev. Lett.*, vol. 81, pp. 1562–1567, 1998.
- [6] K. Nakamura and P. D. Group, “Review of particle physics,” *Journal of Physics G: Nuclear and Particle Physics*, vol. 37, no. 7A, p. 075021, 2010. [Online]. Available: <http://stacks.iop.org/0954-3899/37/i=7A/a=075021>
- [7] V. Barone and E. Predazzi, *High-Energy Particle Diffraction (Theoretical and Mathematical Physics)*. Springer, 2002.
- [8] F. Halzen and A. D. Martin, *Quarks and Leptons: An Introductory Course in Modern Particle Physics*. Wiley, 1984.
- [9] J. D. Jackson, *Classical Electrodynamics Third Edition*. Wiley, 1998.
- [10] A. Brandt *et al.*, “Cross-section measurements of hard diffraction at the SPS collider,” *Phys. Lett.*, vol. B421, pp. 395–404, 1998.

- [11] K. M. Mauritz, “Hard single diffraction in anti-proton proton collisions at 1800-GeV and 630-GeV center-of-mass energies,” 1999, ph.D. Thesis (Advisor: John M. Hauptman).
- [12] L. R. Coney, “Diffractive W and Z boson production in proton anti-proton collisions at  $s^{*1/2} = 1800\text{-GeV}$ ,” 2000, ph.D. Thesis (Advisor: Mitchell Wayne).
- [13] T. L. Edwards, “Diffractively produced Z bosons in the muon decay channel in p-pbar collisions at  $s^{*1/2} = 1.96\text{ TeV}$ , and the measurement of the efficiency of the D0 Run II luminosity monitor,” 2006, ph.D. thesis (advisors: Brian Cox, Terry Wyatt).
- [14] J. D. Bjorken, “A Full acceptance detector for the SSC,” invited talk given at Int. Conf. on Hadron Spectroscopy, College Park, MD, Aug 12-16, 1991.
- [15] F. Abe *et al.*, “Measurement of  $p\bar{p}$  single diffraction dissociation at  $\sqrt{s}=546$  and 1800 gev,” *Phys. Rev. D*, vol. 50, no. 9, pp. 5535–5549, Nov 1994.
- [16] T. Affolder *et al.*, “Double diffraction dissociation at the fermilab tevatron collider,” *Phys. Rev. Lett.*, vol. 87, no. 14, p. 141802, Sep 2001.
- [17] D. Acosta *et al.*, “Inclusive double-pomeron exchange at the fermilab tevatron  $\bar{p}p$  collider,” *Phys. Rev. Lett.*, vol. 93, no. 14, p. 141601, Sep 2004.
- [18] P. D. B. Collins, “An Introduction to Regge Theory and High-Energy Physics,” cambridge 1977, 445p.
- [19] M. L. Good and W. D. Walker, “Diffraction dissociation of beam particles,” *Phys. Rev.*, vol. 120, no. 5, pp. 1857–1860, Dec 1960.
- [20] J. R. Forshaw and D. A. Ross, *Quantum Chromodynamics and the Pomeron (Cambridge Lecture Notes in Physics)*. Cambridge University Press, 1997.
- [21] B. Cox and J. R. Forshaw, “Double diffraction dissociation at high t,” *Phys.Lett.*, vol. B434, pp. 133–140, 1998.

- [22] T. Regge, “Introduction to complex orbital momenta,” *Il Nuovo Cimento (1955-1965)*, vol. 14, pp. 951–976, 1959, 10.1007/BF02728177.
- [23] —, “Bound states, shadow states and mandelstam representation,” *Il Nuovo Cimento (1955-1965)*, vol. 18, pp. 947–956, 1960, 10.1007/BF02733035.
- [24] I. I. Pomeranchuk, “Equality of the nucleon and antinucleon total interaction cross section at high energies,” *Zh. Eksp. Teor. Fiz.*, vol. 34, no. 3, pp. 725–728, 1958.
- [25] A. Donnachie and P. V. Landshoff, “Total cross-sections,” *Phys. Lett.*, vol. B296, pp. 227–232, 1992.
- [26] L. B. Okun, “The Life and Legacy of Pomeranchuk,” in *Proceedings of the International Conference. Held 24-28 January 2003 in Moscow, Russia. Published by World Scientific Publishing Co. Pte. Ltd., 2003. ISBN 9789812702883*, pp. 3–20, Feb. 2003, pp. 3–20.
- [27] S. Donnachie, “Probing the pomeron,” *CERN Cour.*, vol. 39N3, pp. 29–31, 1999.
- [28] A. Donnachie and P. V. Landshoff, “Small  $x$ : Two pomerons!” *Phys. Lett.*, vol. B437, pp. 408–416, 1998.
- [29] C. Adloff *et al.*, “A measurement of the proton structure function  $F_2(x, Q^2)$  at low  $x$  and low  $Q^2$  at HERA,” *Nucl. Phys.*, vol. B497, pp. 3–30, 1997.
- [30] K. A. Goulianos, “Diffractive Interactions of Hadrons at High-Energies,” *Phys.Rept.*, vol. 101, p. 169, 1983.
- [31] M. Froissart, “Asymptotic behavior and subtractions in the mandelstam representation,” *Phys. Rev.*, vol. 123, no. 3, pp. 1053–1057, Aug 1961.
- [32] F. Abe *et al.*, “Measurement of the anti-proton proton total cross-section at  $\sqrt{s} = 546\text{-GeV}$  and  $1800\text{-GeV}$ ,” *Phys.Rev.*, vol. D50, pp. 5550–5561, 1994.
- [33] —, “Measurement of small angle anti-proton - proton elastic scattering at  $\sqrt{s} = 546\text{-GeV}$  and  $1800\text{-GeV}$ ,” *Phys.Rev.*, vol. D50, pp. 5518–5534, 1994.

- [34] —, “Measurement of anti-p p single diffraction dissociation at  $s^{*}(1/2) = 546$ -GeV and 1800-GeV,” *Phys.Rev.*, vol. D50, pp. 5535–5549, 1994.
- [35] K. A. Goulianos, “Renormalization of hadronic diffraction and the structure of the pomeron,” *Phys.Lett.*, vol. B358, pp. 379–388, 1995, fermilab Server has both preprint and published versions of paper.
- [36] Fermilab. (2001, Dec.) History of fermi national accelerator laboratory. [Online]. Available: <http://www.fnal.gov/pub/about/whatis/history.html>
- [37] W. R. Innes *et al.*, “Observation of structure in the  $\Upsilon$  region,” *Phys. Rev. Lett.*, vol. 39, p. 1240, 1977.
- [38] S. Abachi *et al.*, “Observation of the top quark,” *Phys. Rev. Lett.*, vol. 74, pp. 2632–2637, 1995.
- [39] F. Abe *et al.*, “Observation of top quark production in  $\bar{p}p$  collisions,” *Phys. Rev. Lett.*, vol. 74, pp. 2626–2631, 1995.
- [40] A. Alavi-Harati *et al.*, “Observation of direct CP violation in  $K_{S,L} \rightarrow \pi\pi$  decays,” *Phys. Rev. Lett.*, vol. 83, pp. 22–27, 1999.
- [41] J. Sielaff, “Observation of nu/tau charged-current interactions,” 2001.
- [42] J. D. Cockcroft and E. T. S. Walton, “Artificial Production of Fast Protons,” *nature*, vol. 129, pp. 242–+, Feb. 1932.
- [43] S. Abachi *et al.*, “The DØ detector,” *Nuclear Instruments and Methods in Physics Research Section A: Accelerators, Spectrometers, Detectors and Associated Equipment*, vol. 338, no. 2-3, pp. 185 – 253, 1994.
- [44] V. Abazov *et al.*, “The muon system of the Run II DØ detector,” *Nuclear Instruments and Methods in Physics Research Section A: Accelerators, Spectrometers, Detectors and Associated Equipment*, vol. 552, no. 3, pp. 372 – 398, 2005.
- [45] S. Abachi, “The DØ upgrade: The Detector and its physics,” fERMILAB-PUB-96-357-E.

- [46] M. A. Strang, “First observation of dijet events with an antiproton tag at  $\sqrt{s} = 1.96$ -TeV using the DØ Forward Proton Detector,” fERMILAB-THESIS-2005-23.
- [47] M. K. Rominsky, “Measurement of the double differential dijet mass cross section in pp(bar) collisions at  $\sqrt{s} = 1.96$  TeV,” fERMILAB-THESIS-2009-30.
- [48] P. Gutierrez, “The DØ silicon tracker,” *Nuclear Instruments and Methods in Physics Research Section A: Accelerators, Spectrometers, Detectors and Associated Equipment*, vol. 383, no. 1, pp. 21 – 26, 1996, development and Application of Semiconductor Tracking Detectors.
- [49] D. Lincoln, “New technologies in the DØ central tracker upgrade,” *Nuclear Instruments and Methods in Physics Research Section A: Accelerators, Spectrometers, Detectors and Associated Equipment*, vol. 379, no. 3, pp. 424 – 426, 1996, proceedings of the Sixth International Conference on Instrumentation for Experiments at e+ e- Colliders.
- [50] A. Gordeev *et al.*, “Technical design report of the forward preshower detector for the DØ upgrade,” fERMILAB-PUB-98-416-E.
- [51] T. Ferbel, *Experimental techniques in high-energy nuclear and particle physics; 2nd ed.* Singapore: World Scientific, 1991.
- [52] A. Brandt *et al.*, “A Forward proton detector at DØ ,” fERMILAB-PUB-97-377.
- [53] M. Rangel, J. Barreto, and G. Alves, “The Multi-hit Reconstruction in FPD,” d0-NOTE-4339.
- [54] G. Alves, J. Barreto, and M. Rangel, “Forward Proton Tracking at DØ ,” d0-NOTE-5222.
- [55] J. Barreto and A. Drozdhin, “Reconstructing Track Trajectories for the FPD,” d0-NOTE-3788.

- [56] M. Rangel. FPDTrack Documentation. [Online]. Available: [http://www-d0.fnal.gov/d0dist/dist/releases/development/d0fpd\\_track/doc/html/](http://www-d0.fnal.gov/d0dist/dist/releases/development/d0fpd_track/doc/html/)
- [57] L. Mundim. fpd\_db\_client Documentation. [Online]. Available: [http://www-d0.fnal.gov/d0dist/dist/releases/development/fpd\\_db\\_client/doc/html](http://www-d0.fnal.gov/d0dist/dist/releases/development/fpd_db_client/doc/html)
- [58] D. E. Acosta *et al.*, “Inclusive double pomeron exchange at the Fermilab Tevatron  $\bar{p}p$  collider,” *Phys. Rev. Lett.*, vol. 93, p. 141601, 2004.
- [59] T. Affolder *et al.*, “Observation of diffractive  $j/\psi$  production at the fermilab tevatron,” *Phys. Rev. Lett.*, vol. 87, no. 24, p. 241802, Nov 2001.
- [60] K. DeVaughan, “Luminosity Estimation for a Special FPD Store Using Inclusive Jets,” d0-NOTE-5723.
- [61] B. Casey, Y. Enari, T. Kuhl, T. Nunnemann, R. Partridge, P. Polozov, H. Schellman, and M. Wobisch, “Determination of the Effective Inelastic  $p\bar{p}$  Cross-Section for the  $D\bar{O}$  Luminosity Measurement Using Upgraded Readout Electronics,” d0-NOTE-4958.
- [62] D. Bernard, M. Bozzo, P. L. Braccini, F. Carbonara, R. Castaldi, F. Cervelli, G. Chiefari, E. Drago, M. Haguenaue, V. Innocente, P. M. Kluit, B. Kne, S. Lanzo, G. Matthiae, L. Merola, M. Napolitano, V. Palladino, G. Sanguinetti, P. Scampoli, S. Scapellato, G. F. Sciacca, G. Sette, R. Van Swol, J. Timmermans, C. Vannini, J. Velasco, P. G. Verdini, and F. Visco, “The cross section of diffraction dissociation at the cern sps collider. oai:cds.cern.ch:173672,” *Phys. Lett. B*, vol. 186, no. CERN-EP-86-205, pp. 227–232. 16 p, Dec 1986.
- [63] V. A. Khoze, A. D. Martin, and M. G. Ryskin, “Prospects for new physics observations in diffractive processes at the LHC and Tevatron,” *Eur. Phys. J.*, vol. C23, pp. 311–327, 2002.

- [64] P. J. Bussey, T. D. Coughlin, J. R. Forshaw, and A. D. Pilkington, “Central exclusive production of longlived gluinos at the LHC,” *JHEP*, vol. 11, p. 027, 2006.
- [65] V. A. Khoze, A. D. Martin, and M. G. Ryskin, “Double-diffractive processes in high-resolution missing- mass experiments at the Tevatron,” *Eur. Phys. J.*, vol. C19, pp. 477–483, 2001.
- [66] A. De Roeck, V. A. Khoze, A. D. Martin, R. Orava, and M. G. Ryskin, “Ways to detect a light Higgs boson at the LHC,” *Eur. Phys. J.*, vol. C25, pp. 391–403, 2002.
- [67] A. B. Kaidalov, V. A. Khoze, A. D. Martin, and M. G. Ryskin, “Extending the study of the Higgs sector at the LHC by proton tagging,” *Eur. Phys. J.*, vol. C33, pp. 261–271, 2004.
- [68] B. E. Cox, “A review of forward proton tagging at 420-m at the LHC, and relevant results from the Tevatron and HERA,” *AIP Conf. Proc.*, vol. 753, pp. 103–111, 2005.
- [69] V. A. Khoze, A. D. Martin, and M. G. Ryskin, “Central jet production as a probe of the perturbative formalism for exclusive diffraction,” *Eur. Phys. J.*, vol. C48, pp. 467–475, 2006.
- [70] M. G. Albrow and A. Rostovtsev, “Searching for the Higgs at hadron colliders using the missing mass method,” 2000.
- [71] M. Albrow, “FP420,” 2005.
- [72] V. A. Khoze, M. G. Ryskin, and W. J. Stirling, “On radiative QCD backgrounds to exclusive  $H \rightarrow b \bar{b}$  production at the LHC and a photon collider,” 2006.
- [73] J. Monk and A. Pilkington, “ExHuME: A Monte Carlo event generator for exclusive diffraction,” *Comput. Phys. Commun.*, vol. 175, pp. 232–239, 2006.

- [74] T. Sjostrand, S. Mrenna, and P. Skands, “PYTHIA 6.4 physics and manual,” *JHEP*, vol. 05, p. 026, 2006.
- [75] B. E. Cox and J. R. Forshaw, “POMWIG: HERWIG for diffractive interactions,” *Comput. Phys. Commun.*, vol. 144, pp. 104–110, 2002.
- [76] B. E. Cox, F. K. Loebinger, and A. D. Pilkington, “Detecting Higgs bosons in the  $b\bar{b}$  decay channel using forward proton tagging at the LHC,” *JHEP*, vol. 10, p. 090, 2007.
- [77] S. Heinemeyer *et al.*, “Studying the MSSM Higgs sector by forward proton tagging at the LHC,” *Eur. Phys. J.*, vol. C53, pp. 231–256, 2008.
- [78] V. A. Khoze, M. G. Ryskin, and W. J. Stirling, “Diffractive  $W + 2\text{jet}$  production: A background to exclusive  $H \rightarrow W W$  production at hadron colliders,” *Eur. Phys. J.*, vol. C44, pp. 227–232, 2005.



## BIOGRAPHICAL STATEMENT

Arnab K. Pal was born in India in 1979. He received his B.Sc(Hons.) degree in physics from University of Delhi in 1999. Then in 2001 he received his M.Sc degree in physics from Indian Institute of Technology(Kanpur) in India. He joined University of Texas at Arlington in the 2005 as a graduate student. Then in 2007, he went to Center For European Nuclear Research (CERN) to work on the ATLAS experiment which is one of the experiments of the Large Hadron Collider (LHC). In 2008, he came back from CERN after finishing his service work to the experiment and joined the DØ experiment at Fermi National Accelerator Lab to finish his thesis work on single diffractive differential cross section measurement.